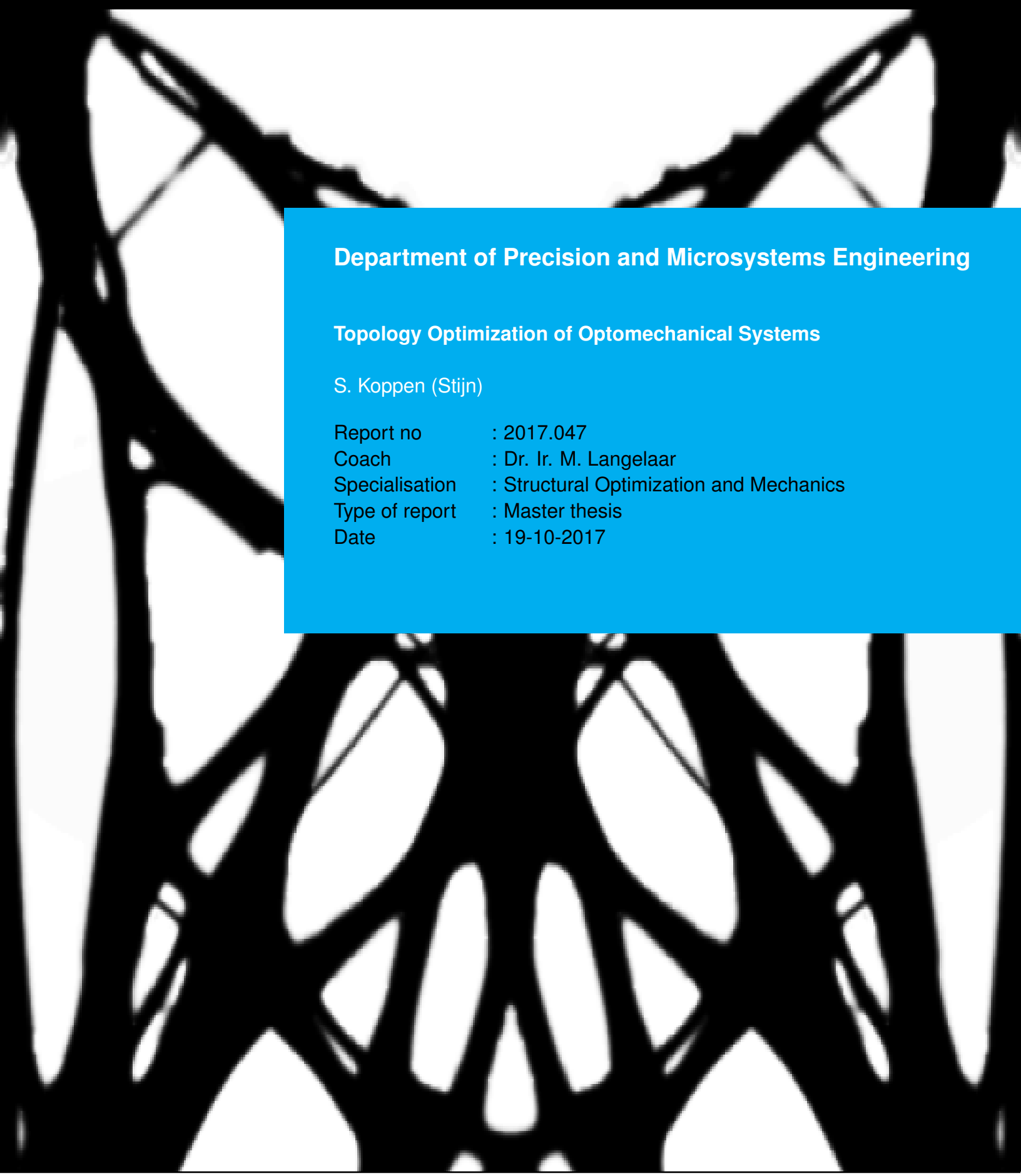

Department of Precision and Microsystems Engineering

Topology Optimization of Optomechanical Systems

S. Koppen (Stijn)

Report no	: 2017.047
Coach	: Dr. Ir. M. Langelaar
Specialisation	: Structural Optimization and Mechanics
Type of report	: Master thesis
Date	: 19-10-2017

TU Delft Delft University of Technology

Challenge the future

TOPOLOGY OPTIMIZATION OF OPTOMECHANICAL SYSTEMS

A thesis submitted to
Delft University of Technology
Mechanical, Maritime and Materials Engineering (3ME)
Precision and Microsystems Engineering (PME)
by

Stijn Koppen

In partial fulfillment of the requirements for the degree
of
Master of Science

to be defended publicly on Thursday October 19th, 2017 at 09:00.

Thesis committee:
Dr. Ir. Matthijs Langelaar (TU Delft, PME)
Prof. Dr. Ir. A. van Keulen (TU Delft, PME)
Prof. Dr. Ir. J. Herder (TU Delft, PME)
Ir. M. Van der Kolk (TU Delft, PME)
Dr. Ir. J. de Vreugd (TNO)
Ir. F.C.M. Van Kempen (TNO)

An electronic version of this thesis is available at `repository.tudelft.nl`.

PREFACE

Before you lies the master thesis "Topology Optimization of Optomechanical Systems", that describes a new approach to the thermomechanical design of optical instruments. It has been written to fulfill the graduation requirements of the master program Mechanical Engineering at the Delft University of Technology. The thesis is the final element of my graduation at the department of Precision & Microsystems Engineering (PME) with a specific focus on Structural Optimization and Mechanics.

The project was undertaken at the Optomechatronics department of the Netherlands Organization for Applied Scientific Research (TNO) under the supervision of Jan de Vreugd and Matthijs Langelaar, which I would like to thank for their active and enthusiastic guidance and support. Insights from and continuous contact with colleagues from various fields appeared to be a key aspect in answering the complex research questions. Therefore, I would like to thank Floris van Kempen (optimization), Rudolf Saathof (optomechatronics), James Day (optics) and Max Van der Kolk (optimization).

The project has, in addition to this thesis, resulted in a paper to be published in the journal of Structural & Multidisciplinary Optimization, written in cooperation with Max Van der Kolk, Floris van Kempen, Jan de Vreugd and Matthijs Langelaar. The process of iteratively restructuring, rewriting and reviewing the content has by far been the most intensive and academically instructive moment in my life, for which I thank the co-authors.

As each project has its setbacks, this project proved no exception. Thanks to the help of my family and friends I was able to convert such setbacks in stronger motivation. Large parts of my discipline has been the result of the encouraging and motivating discussions with my girlfriend; special thanks to you.

Stijn Koppen

Delft, October 19th, 2017

TABLE OF CONTENTS

Page

SYMBOLS

α	CTE
$\mathbf{A}_{\mathrm{XY}}(\mathbf{s})$	Global thermal expansion matrix of DOF set XY
$\mathbf{b}$	LLSR fit coefficients vector
β	Heaviside projection penalization parameter
c_{p}	Heat capacity coefficient at constant pressure
$\mathbb{C}$	Stiffness tensor
$\mathbf{d}$	System OPLs
D	Diffusivity
$\underline{D}$	Diffraction limit
$\boldsymbol{\delta}_i$	Misalignments of component i
$\delta_{\mathrm{z},i}$	Despace misalignment of surface i
$\delta_{\mathrm{x},i}$	Decenter misalignment of surface i
E	Young's modulus
E_0	Unpenalized Young's modulus
E_i	Penalized Young's modulus of element i
$\mathbf{E}_i$	Component specific misalignment vector of component i
ε_{m}	Mechanical strain
$\varepsilon_{\Delta\mathbf{s}}$	Convergence threshold
$\varepsilon_{\Delta\mathrm{f}(\mathbf{s})}$	Objective function convergence threshold
$\varepsilon_{\mathrm{g}(\mathbf{s})}$	Constraints convergence threshold
η	Heaviside projection threshold parameter
f	Eigenfrequency
f_i	Objective function of component i
f_*	Stationary solution at $\mathbf{s}_*$
$f_\dagger$	Local optimal solution at $\mathbf{s}_\dagger$
f_{n}	Natural eigenfrequency
F	Force
$\mathbf{F}_{\mathrm{X},i}$	Global force vector of DOF set X of component i
g	Gravitational acceleration
g_i	Constraint number i
$\mathbf{g}(\mathbf{s})$	Set of inequality constraints
$\mathbf{G}$	LLSR fit matrix
Γ_i	Optical surface of component i
$\mathbf{h}(\mathbf{s})$	Set of equality constraints

$\mathbf{H}_{\mathrm{XY}}(\mathbf{s})$	Global conductivity matrix of DOF set XY
$\mathbf{H}$	Hessian matrix
I	Mass moment of inertia
$\mathbf{I}$	Identitiy matrix
k	Coefficient of thermal conductivity
k	Spring stiffness of a single DOF system
$\mathbf{K}_{\mathrm{XY}}(\mathbf{s})$	Global stiffness matrix of DOF set XY
κ_i	Curvature of surface i
L	Length scale in definition of CTE
$\mathbf{L}$	Displacement DOF selecting matrix
λ_i	Eigenvalue of mode i
λ_{l}	Wavelength of light
$\boldsymbol{\lambda}$	Lagrange multipliers related to inequality constraints
$\boldsymbol{\lambda}_{\mathrm{X}}$	Lagrange multipliers of DOF set X
m	Mass
$\mathbf{M}_i$	Transfer matrix of component i
$\mathbf{M}_{\mathrm{XY}}(\mathbf{s})$	Global mass matrix of DOF set XY
μ	Gaussian profile expected value
$\boldsymbol{\mu}$	Lagrange multipliers related to equality constraints
$\hat{n}$	Number of design variables
n_{r}	Index of refraction
ν	Poisson's ratio
ω_i	Eigenfrequency of mode i
ω_{n}	Fundamental elastic eigenfrequency
Ω_i	Design domain of component i
$\mathscr{O}$	Approximation error
p	Penalization factor
$\mathbf{p}$	System specific constant parameters
ϕ_i	Mode shape i
ϕ_i	Angle of incidence of component i
$\boldsymbol{\Phi}(\mathbf{x})$	LSF as function of position
$\boldsymbol{\phi}$	System angles of incidence
q	Penalization weight factor
Q	Heat load
$\mathbf{Q}_{\mathrm{X},i}$	Global heat load vector of DOF set X of component i
R_i	Radius of curvature of surface i
$\mathbf{R}$	Nodal residuals
r_i	Deviation of the positional error of ray i to the average spot location
$\bar{r}$	Spatial filter radius
r_{ij}	Spatial filter distance between centroids of elements i and j
$\mathbf{r}_i$	Ray vector before component i

$\mathbf{r}_{0,i}$	Initial ray vector of ray i
ρ	Density
ρ_0	Density of unpenalized element
ρ_i	Penalized density of element i
$R_{\mathrm{X}}(\mathbf{s})$	Interpolation function of material property X
$\mathbf{s}$	Design variables
s_*	Variable at stationary point in design space (minimizer)
$s_\dagger$	Variable at local optimum in design space
$\mathbf{s}_0$	Initial set of variables
$\tilde{\mathbf{s}}$	MMA optimized design variables
$\hat{\tilde{\mathbf{s}}}$	Density filtered design variables
$\mathscr{S}$	Variable bound constraint
σ	Stress or Cauchy stress tensor
σ_{y}	Yield stress
σ^2	Gaussian profile variance
t	Time
T	Temperature
ΔT	Temperature change
$\mathbf{T}_{\mathrm{X},i}$	Global temperature vector of DOF set X of component i
$\theta_{\mathrm{y},i}$	Tip/tilt misalignement of surface i
$\mathbf{U}_{\mathrm{x},i}$	In plane displacement vector of surface i
$U_{\mathrm{z},i}$	Out of plane displacement of nodal point i
$\mathbf{U}_{\mathrm{z},i}$	Out of plane displacement vector of surface i
$\hat{U}_{\mathrm{z},i}$	Fitted out of plane displacement of nodal point i
$\hat{\mathbf{U}}_{\mathrm{z},i}$	Fitted out of plane displacement vector of surface i
$\mathbf{U}_{\mathrm{X},i}$	Global displacement vector of DOF set X of component i
V	Volume
$V(\mathbf{x})$	Velocity field or speed function of LSF
V_{Ω_i}	Volume of design domain i
$\mathbf{V}$	LLSR Vandermonde matrix
ε	Infinitesimal strain
ε_i	Ray i
$\varepsilon_{\mu,i}$	Average positional error due to misalignments of surface i
w_i	Spatial filter linear weight of element i
x	Nodal coordinate in X direction
$\mathbf{x}$	Vector of coordinates
$\mathbf{Y}$	LLSR coefficients fit matrix
z	Nodal coordinate in Z direction

ABBREVIATIONS

CS	Coupled System
CTE	Coefficient of Thermal Expansion
DOF	Degree of Freedom
E-ELT	European Extremely Large Telescope
ESA	European Space Agency
ESO	European Southern Observatory
EUV	Extreme Ultraviolet Lithography
GAIA	Global Astrometric Interferometer for Astrophysics
KKT	Karush Kuhn Tucker
LLSR	Linear Least Squares Regression
LSF	Level Set Function
MATLAB	MATrix LABoratory
MDO	Multidisciplinairy Design Optimization
MMA	Method of Moving Asymptotes
MMC	Metal Matrix Composite
OPL	Optical Path Length
PLSM	Parametric Level Set Method
PSD	Power Spectral Density
P-V	Peak-to-Valley
RAMP	Rational Approximation of Material Properties
RMS	Root Mean Square
RMSE	Root Mean Square Error
RSS	Root Sum Squared
SDO	System Design Optimization
SFE	Surface Form Error
SIMP	Solid Isotropic Material with Penalization
STOP	Structural-Thermal-Optical Performance
TC	Thermal Center
TNO	Netherlands Organization for Applied Scientific Research
ULE	Ultra-Low Expansion glass
US	Uncoupled System
WFE	Wave Front Error

ABSTRACT

The stringent and conflicting requirements of optomechanical instruments and the ever-increasing need for higher resolution and quality imagery demands a tightly integrated design approach. The aim of this study is to drive the thermomechanical design of multiple components of an optomechanical instruments by the system's optical performance. This work addresses the combination of structural-thermal-optical performance analysis and multicomponent topology optimization while taking into account both component and system level constraints. A 2D two-mirror example demonstrates that the proposed approach is able to improve the system's spot size error by 95 % compared to uncoupled system optimization.

EXECUTIVE SUMMARY

Optomechanical instruments enable humanity to explore new galaxies, communicate via space, measure and manufacture at the nanometer scale and modify human genetics. The optomechanical design involves many coupled disciplines such as thermal control, structural mechanics, motion control and optics. The stringent and conflicting requirements of optomechanical instruments and the ever-increasing need for higher resolution and quality imagery demands a tightly integrated design approach.

Many factors contribute to the inability of an optical system to produce a perfect image, including chromatic and geometrical aberrations, fabrication and alignment errors and environmental effects such as temperature fluctuations and vibrations. Structural deformations and temperature differences of the housing or frame should neither excessively distort the mount nor the optical surface, requiring a compliant design. Those deformations depend on loading and support conditions, material properties (e.g. density, Young's modulus, thermal conductivity, thermal expansion coefficient), structural efficiency and size. In contrast to a compliant design, the optical components require a stiff design, as the structure must constrain the component such that they are not damaged or irreversibly moved after exposure to external conditions.

The aim of this thesis is to investigate how to design optomechanical components such that the optical performance degradation due to thermal loads or mounting errors is minimized and to drive the thermomechanical design of multiple components through the system's optical performance. This work focuses on the reduction of optical performance errors of reflective optical systems induced by (quasi)-static thermal loads and alignment errors by optimizing the material layout of the mounts. Therefore, it is of interest to research the influence of including optical performance metrics in the design and optimization of these systems. For multicomponent systems, it is of interest what the differences are between optimizing a coupled system and optimizing the individual components.

The typical design approach of optomechanical instruments is characterized by the optical discipline creating a performance error budget that defines deformation limits for each optical component to the structural discipline. From this point of view, an optical system functions as long as the components remain within allowed tolerances of their nominal locations, orientations and deformations. Thus in the thermomechanical design process, the optical performance is not considered directly and each component is designed and optimized separately to meet a priori defined deformation limits. Typical optomechanical design focuses on structural and kinematic design (e.g. flexural design), thermal stability and athermalization, vibration control and material selection to meet those limits. This approach satisfies the optical performance requirements, though individual components are unnecessary overconstrained leading to non-optimal system designs.

This study involves combining multiple methods of multiphysics analysis techniques and structural optimization, which led to an effective new design optimization procedure. The optomechanical optimization problems generally are characterized by difficult multiphysics and non-selfadjoint response functions involving multiple nonlinear constraints. Therefore, this study uses a density gradient-based topology optimization procedure to maximize the design freedom to systematically find an optimal solution.

This work proposes a new method that includes system optical performance metrics in the thermomechanical design and optimization process and optimizes all components simultaneously in order to exploit component interactions and uses system-level constraints where possible. The method incorporates a full structural-thermal-optical performance analysis into a gradient-based topology optimization framework to effectively optimize the layout of multiple mirror mounts reducing the systems optical performance expressed in terms of spot size and position accuracy. The combination of a structural-thermal-optical performance analysis and topology optimization simultaneously utilizes the optical, structural and thermal design aspects in the structural design optimization. By enlarging the design space, one can further improve the instruments' optical performance, or maintain the optical performance under more stringent constraints.

To analyze a multicomponent optical system the deformed surfaces (analyzed by finite element analysis) are approximated by a least squares fit to obtain the optical surface misalignments (rigid body effects and surface form errors). Next, the ray transfer matrix analysis can be used to track the position and angle of paraxial rays through the system.

Multiple different optimization problems of a single mirror mount subjected to thermal influences and alignment errors show that there is a certain bandwidth of minimum eigenfrequency constraint values that influence the ability of the optimizer to minimize surface deformations. Thus, conflicting requirement tolerance values should be thoroughly investigated, as their limits can highly influence the topology layout and performance.

A 2D two-mirror example case shows that the proposed approach is able to improve the system's spot size error by 95 percent compared to uncoupled system optimization to below the system's diffraction limit. Thus, the case study proves that an integrated structural-thermal-optical thermomechanical design optimization procedure, taking into account all system components improves the system optical performance compared to individual component optimization, while subjected to equivalent design constraints. Whereas the uncoupled optimization aims to design two perfectly flat mirrors, the layout of the second mirror in the coupled optimization is such that its misalignments (mainly curvature) effectively counter effect the misalignments of the first mirror. Thus, the typical design approach unnecessarily overconstrains problems, whereas the system design optimization approach enlarges the feasible design domain and gives the optimizer more freedom to minimize the objective while still satisfying all constraints.

Further research might well be conducted on the extension to multiple and different optical components as well as the extension to 3D structures while taking manufacturability into account. Despite the academic nature of this study, it shows optomechanical designers should aim for considering and integrating

multiple components and physics simultaneously in the design loop when requirements seem irreconcilable.

1. INTRODUCTION

1.1 Optomechanical instruments

Optomechanical instruments control light by means of optics and generally have to meet very stringent optical, mechanical and thermal requirements [See e.g. 1–3]. These instruments enable use to explore new galaxies, communicate via space, measure and manufacture at the nanometer scale and explore and modify the human genetics. They are found in high-tech applications in disciplines such as (nano)metrology, astronomy, life sciences, aerospace, lithography, and communications. Some cutting-edge examples are the Sentinel 5 UV-1 spectrometer, the Global Astrometric Interferometer for Astrophysics (GAIA) and the European Extremely Large Telescope (E-ELT), see Figs. 1.1a, 1.1b and 1.2. The challenge of optomechanics lies in maintaining the position and shape of optical elements such that the optical performance is guaranteed under all working environments [e.g. 4, 5]. Those environments include extreme pressures (e.g. vacuum in space), high vibration levels, shocks, pollution and extreme high/low temperatures (cryogenic applications) and temperature fluctuations. The optomechanical design is a tightly integrated process involving many disciplines such as thermal control, structural mechanics, motion control and optics.

1.2 Optical performance and design requirements

The optical performance generally encompasses the systems' image quality, optical resolution, and image position accuracy. Both image quality and optical resolution are typically quantified by the spot size or image blur diameter [e.g. 10, 11]. The spot size of an aberration-free system is limited by the wavelength of light. This diffraction limit determines the minimum blur diameter that is achievable by an optical system and hence provides a reference for image quality. The spot size mainly depends on the wavefront quality due to geometric aberrations, whereas the beam position accuracy depends on the pointing (angular) errors of the optical components. These performance metrics can be determined using geometric ray tracing, which traces the propagation of light rays through an optical system [e.g. 12]. For flat or spherical single-mirror systems the Wave Front Error (WFE) scales linearly with the Surface Form Error (SFE) of the deformed surface and the pointing error is directly related to the tilt of the surface [e.g. 13, 14]. The optical performance metric of interest thus depends on the application and system composition. Figure 1.3 shows a 2D schematic of an arbitraty reflective optomechanical system to further clarify the discussed definitions. The SFE equals the difference between the deformed and undeformed surface configurations, whereas the WFE equals the difference between the wavefronts originating from the de-

(a) The Global Astrometric Interferometer for Astrophysics (GAIA) basic angle monitor optomechanical assembly module, fully made out of sintered Silicon Carbide. The system consist of two bars, a light source and beam splitters to measure the field of view or 'basic angle' of two separated telescopes with an accuracy comparable to measuring the diameter of a human hair at a distance of 1000 kilometres [See: 6, 7]. GAIA is launched in 2012 by the European Space Agency (ESA) and aims to measure with extreme precision the position and speed of billions of stars and create a 3D map of the universe.

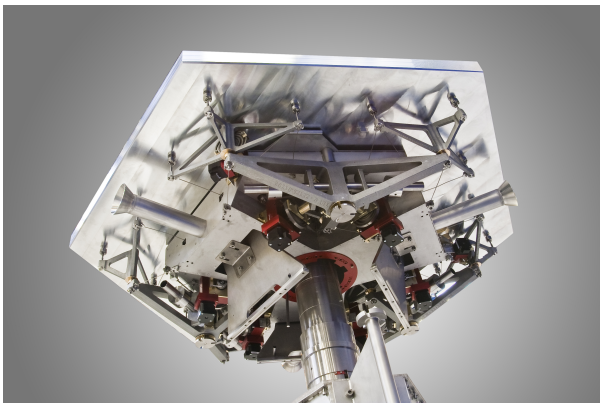

(b) The European Southern Observatory (ESO) is currently designing and building the European Extremely Large Telescope (E-ELT), which will be the largest optical telescope in the world with a primary mirror of almost 40 m in diameter consisting of nearly 1000 hexagonal segments of 1.2 m in width. TNO designed and optimized the support structure for each segment, leading to a maximum surface from error of 30 nm root mean square independent of the segment orientation and temperature [See: 8, 9].

Figure 1.1.: Cutting-edge optomechanical instruments; the GAIA basic angle monitor assembly module and the E-ELT.

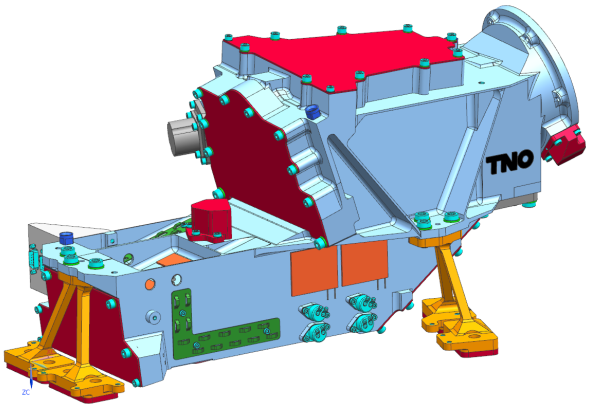

(a) Structural design of the Sentinel 5 UV1 spectrometer. The mirrors are bolted to the housing, which is semi-kinematically connected to the satellite frame via flexures in order to limit deformations due to imposed rigid body displacements of the frame.

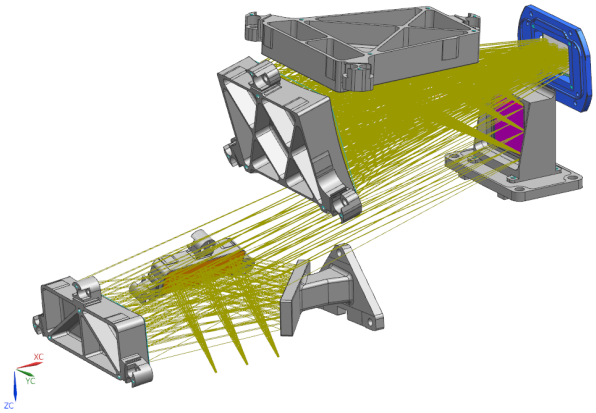

(b) Optical design of the UV1 illustrating the mirror mounts and optical rays. Note the different mirror back layouts and consistent connections to the frame. The spot position and size depends on the misalignments and surface deformations of all optical components.

Figure 1.2.: The European Space Agency's (ESA) SENTINEL 5 shortwave UV1 band (270-300 nm) spectrometer system to be carried on the MetOp-SG satellite.

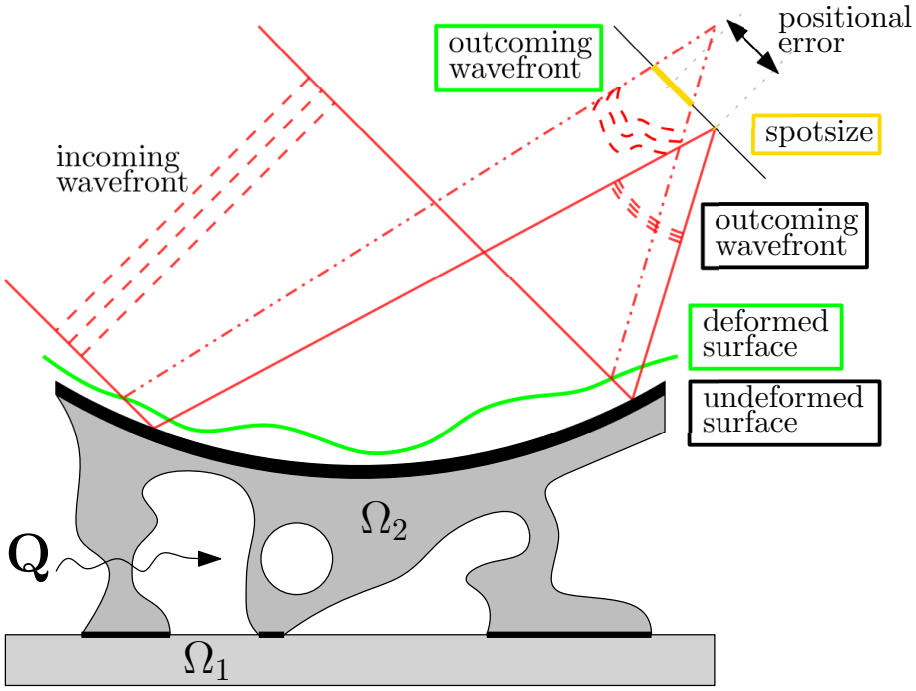

Figure 1.3.: Schematic of a reflective optical system, to illustrate the principles of surface form and wave form error and the resulting influence on the image quality (spot size and positional error). Domain Ω_1 represents a frame or housing, whereas Ω_2 represents the mounting structure. Due to a heat load Q, a misalignment in assembly or a difference in temperature between both domains, the body will deform causing the undeformed surface to deform, leading to Surface Form Errors (SFEs). Incoming light with a perfect wave front will deflect from the deformed surface degrading the wave front causing Wave Front Errors (WFEs), which will, in combination with rigid body effects of the surface lead to image quality degradation. In this case this is show by an increase in spot size and positional error in relation to the perfect system.

formed and undeformed surfaces, respectively. Both spotsize and positional accuracy degrade when a system subjected to environmental loads.

Many factors may contribute to the inability of an optical system to produce a perfect image, including chromatic and geometrical aberrations, fabrication and alignment errors, self-weight, and environmental effects such as temperature fluctuations. This work focuses on the reduction of optical performance errors of reflective optical systems induced by (quasi)-static thermal loads. Therefore, structural deformations and temperature differences of the frame should neither excessively distort the mount nor the optical surface. This implies that a mechanically disconnected frame and optical surface combination would be optimal. However, the presence of thermal loads requires material to abduct the heat from the optical surfaces to the frame or vice versa. In contrast, the optical components also require a stiff design, as the structure must constrain the components such that they are not damaged or irreversibly moved after exposure to external conditions such as vibrations, thermal shocks and gravity [e.g. 1–3]. To limit excitation from external vibrations, the fundamental elastic eigenfrequency must be higher than a critical lower limit. Adding more practical constraints such as maximum mass and material usage, which are often linked to costs, the optomechanical mirror support design clearly involves multiple conflicting structural requirements. Thus, careful consideration of the thermomechanical and dynamic performance of optical mounts is required. Optimization techniques can aid in this process.

1.3 Problem definition

The typical design approach of optomechanical instruments is characterized by the optical discipline creating a performance error budget that defines deformation limits for each optical component to the structural discipline. In an iterative design process, the thermal discipline provides the temperature fields and gradients after which the structural discipline aims to realize a design which meets the deformation limits during thermal and other environmental load cases. From this point of view, an optical system functions as long as the components remain within allowed tolerances of their nominal locations, orientations and deformations. Thus, in the thermomechanical design process, the optical performance is not considered directly and each component is designed and optimized separately to meet a priori defined deformation limits.

This approach satisfies the optical performance requirements, however individual components are overdesigned, as each component is exposed to worst-case load scenarios. Overdesigning components can increase weight and thereby costs. Furthermore, overdesign may lead to less optimal designs in relation to performance, due to unnecessary overconstraining of the design problem. Hence, there is a clear need for improved design approaches.

To enlarge the design space and further improve the optical performance of optical instruments, this thesis proposes that

1. system-level optical performances metrics should be taken into account during the thermomechanical design and optimization process,
2. all optical component designs should be optimized simultaneously for these metrics, and
3. system-level constraints should, if possible, not be replaced by component-level constraints.

1.4 Approach: simultaneous multicomponent multidisciplinary topology optimization

Model-based structural optimization techniques can aid in further improving the performance of optical instruments. Both heuristic procedures and mathematical routines are often applied. The heuristic procedures are based on simple statistics or genetics. These approaches result in designs that perform well, though for more conflicting and multi-physical problems a mathematical optimization routine is preferable. These routines provide a rigorous, systematic approach to find the optimal designs. Structural optimization problems are generally formulated as a sizing, shape or topology optimization problem. Whereas in sizing and shape optimization the design variables are dimensions of a predefined geometry, topology optimization is based on adding or removing small parts of the material. Topology optimization is a systematic, bottom-up structural optimization approach that provides maximum design freedom without any prior knowledge of the design. The procedure can effectively optimize the material layout within given design domains in order to maximize a performance measure, while subjected to a given set of loads, boundary conditions, and constraints [See e.g. 15]. The method, in combination with mathematical programming, has shown to be able to solve complex nonlinear multidisciplinary problems with multiple active constraints and is capable of producing innovative solutions.

In order to couple all involved physics of the optomechanical design and profit from the interactions between different disciplines an integrated Multidisciplinary Design Optimization (MDO) approach is often applied, resulting in superior designs. For optomechanical systems, an integrated Structural-Thermal-Optical Performance (STOP) analysis should be incorporated in the optimization procedure for this purpose [e.g. 11, 16, 17]. This combination utilizes simultaneous optimization of the optical, structural and thermal design aspects. Prior work in STOP optimization couples various analysis tools to obtain the optical performance. This shows great improvement, although the optimization often only includes sizes as variables and thus uses only a limited number of variables such as face sheet thickness and strut diameters [e.g. 18–20]. The STOP optimization procedure includes optical knowledge at the thermomechanical design level but the design freedom is not yet fully exploited.

In addition, one can simultaneously apply multidisciplinary optimization to multiple components or a system assembly and optimize for an optical performance metric at the system level, taking into account component level interactions. This approach will be referred to as System Design Optimization (SDO). To determine the system optical performance, this study uses a simplified version of geometric ray tracing, the ray transfer matrix analysis. The method uses the paraxial approximation of ray optics to construct a ray transfer matrix that describes the behavior of an optical system [e.g. 21–23].

The goal of this thesis is to show that an integrated structural-thermal-optical thermomechanical design optimization procedure taking into account all system components improves the system optical performance compared to individual component optimization, while subjected to equivalent design constraints.

Next two chapters give additional background in the fields of optomechanical design, Chapter 2, and structural optimization in Chapter 3. The formulation of the coupled thermomechanical discretized equilibrium equations, topology optimization formulation and sensitivity analysis of a generalized response function are described in Chapter 4. The extension to a full STOP optimization approach can be found in Chapter 5, which focuses on the optical performance prediction from finite element analysis results. Numerical examples, supporting the answers to the research questions, are to be found in Chapter 7. Finally, additional discussion, recommendations and conclusions are presented in Chapter 8 and Chapter 9.

2. OPTOMECHANICAL DESIGN

Optomechanics is defined as the part of optical engineering concerned with maintaining the shape and position of the optical systems' surfaces. Deviation from a stress-free condition always leads to deformations, which affect both the position and shape of surfaces in an optical system. The driving design requirement for operation is the optical performance while subjected to thermal loads, vibrations and temporal material changes. A proper optical system functions as long as the components remain within allowed tolerances of their nominal locations and orientations. Therefore, the design objective considered in optomechanical design is focused on deformations rather than stress.

2.1 Environmental conditions and requirements

The environmental conditions an optomechanical instrument has to withstand are generally very stringent at all stages of its lifetime. Both survival and operational environmental conditions dictate the design driving requirements. The survival conditions include situations where the performance is not of importance, however the instrument must be able to operate without degradation of performance after returning to the operational conditions. Severe conditions for survival happen during manufacturing, assembly and transport. For example for space applications that are typically

- extreme pressures and pressure drops from 102 kPa to vacuum with an average rate of $-2\,\mathrm{kPa\,s^{-1}}$ and accompanying moisture release effects,
- high vibrations and acoustic noise levels; power spectral density levels up to $0.13\,\mathrm{g^2/Hz}$ within a range of $30\,\mathrm{Hz} \leq f \leq 1500\,\mathrm{Hz}$,
- shock loads (approx. max 4 g over a 40 ms period),
- manufacturing loads (e.g. polishing or postprocessing),
- humidity levels between 0 % and 80 %, and
- extreme temperatures, as low as 100 K for cryogenic applications up to 344 K for hot cases, as well as temperature changes.

Those survival conditions generally impose maximum weight, minimum static/dynamic stiffness, limited material selection and maximum stress constraints derived from multiple different load cases.

During operation the design driving requirements are quite different, for example for space applications the pressure and static loads can be assumed negligible, though micro-vibrations arising from other subsystems or small temperature gradients become critical load cases. The system must be susceptible to, and withstand all dynamic and thermal loading conditions while performing nominally and provide full specified optical performance during the full operational lifetime. The system must perform at varying interface environment levels within a certain stability range; that is the optical performance must be retained within a certain precision, accuracy or resolution for a set of external temperatures or heat loads. The performance is often given by an optical measure, such as the allowable WFE, which dictates the required stability of the optical components relative to the mount interfaces, including temporary or permanent change in position of the optical component after initial alignment due to static, dynamic and thermal loads.

2.2 Design process

The first step in any optomechanical design is defining why the design needs to be done and what the corresponding performance metrics and design requirements are. Although many specifications may be of interest, generally a couple are the most important; the driving requirements. These driving requirements will determine in which direction trade-offs will be made.

The optical design starts with a preliminary design using simplified hand calculations in order to determine focal lengths and such. Light passing through an optical system consisting of various optical elements such as mirrors, prisms, gratings and lenses, can be analyzed using the ray properties of light. The trajectory of a ray can be computed by using the law of reflection and Snell's law of refraction. Followed by a paraxial design (based on linear approximations), most of the optomechanical requirements will be found and the optomechanical design can start by the selection of mounting structures and geometries as well as materials.

After the preliminary design has been evaluated using models and analysis techniques, the process of tolerancing begins. Tolerancing basically entails figuring out how far the manufacturing of the system elements and the operational conditions can stray before the system performance drops below acceptable levels. After defining starting tolerances, the effects of these boundaries on merit function are calculated. Once those effects are known, they are generally summed via the Root Sum Square (RSS). A more advanced method of tolerancing is by performing a Monte Carlo analysis, in which the optical Degrees Of Freedom (DOFs) are randomly varied to simulate the randomness of manufacturing errors or environmental conditions.

The detailed design basically consists of iterative redesign based on the tolerance limits and redefinition of the tolerance budget, until all requirements are met. The last step in the process is to experimentally verify the system requirements of the detailed design, either using a breadboard or full model, depending on the application.

2.3 Thermomechanics

In order to analyze heat transfer and thermal expansion one can describe these physical phenomena by differential equations. Assuming linearity and temperature independent material properties, a structure can be analyzed by discretizing these equations in both space and time. The heat equation describes the distribution of heat by conduction in a given regime over time. The temperature field $T(x,y,z,t)$ as a function of the spatial variables and time is described by

$$\frac{\partial T(\mathbf{x},t)}{\partial t} - D\frac{\partial^2 T(\mathbf{x},t)}{\partial \mathbf{x}^2} = Q(\mathbf{x},t), \tag{2.1}$$

where $D = \frac{k}{c_\mathrm{p}\rho}$ is the thermal diffusivity, a material-specific quantity depending on the thermal conductivity k, the mass density ρ and the specific heat capacity c_p. Q is the rate of internal heat generation. Assuming steady state conditions the equation simplifies to

$$-k\frac{\partial^2 T(\mathbf{x})}{\partial \mathbf{x}^2} = Q(\mathbf{x}). \tag{2.2}$$

The constitutive relations governing the linear elastic boundary value problem include the equations of motion (Newton's second law). Taking into account the thermoelastic forces, these are defined as

$$\rho\frac{\partial^2 \mathbf{U}(\mathbf{x},t)}{\partial t^2} - \frac{\partial \boldsymbol{\sigma}(\mathbf{x},t)}{\partial \mathbf{x}} = \mathbf{F}(\mathbf{x},t) + E\alpha\Delta T(\mathbf{x},t), \tag{2.3}$$

where $\mathbf{U}$ is the displacement vector, σ is the Cauchy stress tensor, $\mathbf{F}$ the body force per unit volume, E the Young's modulus, α the Coefficient of Thermal Expansion (CTE) and $\Delta T(\mathbf{x},t)$ the change in temperature at time t with respect to the stress free condition at location $\mathbf{x}$. For steady state statics Eq. (2.3) simplifies to

$$-\frac{\partial \boldsymbol{\sigma}(\mathbf{x})}{\partial \mathbf{x}} = \mathbf{F}(\mathbf{x}) + E\alpha\Delta T(\mathbf{x}). \tag{2.4}$$

The strain-displacement relations are given by

$$\boldsymbol{\varepsilon} = \frac{1}{2}\left(\frac{\partial \mathbf{U}(\mathbf{x},t)}{\partial \mathbf{x}} + \left(\frac{\partial \mathbf{U}(\mathbf{x},t)}{\partial \mathbf{x}}\right)^T\right), \tag{2.5}$$

where ε is the infinitesimal strain tensor. The constitutive equations, for linear elasticity based on Hooke's law, are given by

$$\boldsymbol{\sigma} = \mathbb{C}(E,\nu) : \varepsilon, \tag{2.6}$$

where $\mathbb{C}$ is the fourth-order stiffness tensor and ν the Poisson's ratio. A more in depth implementation of the discretized version of Eq. (2.4) can be found in Chapter B.

2.4 Material properties

For structural components, the physical property of interest is the mass density ρ, which is relatively constant in relation to temperature differences. Deflection in any application depends on support conditions, material properties, structural efficiency, size and loading conditions.

Important mechanical properties in relation to optomechanical design, include the elastic moduli, strength and fracture. For crystalline materials, the elastic properties can be described by the Young's Modulus E and Poisson's ratio ν, which both vary with temperature. The specific stiffness $\frac{E}{\rho}$ is an important material selection criteria. Other mechanical properties of interest are the creep strength, ductility, fatigue strength, fracture toughness, hardness, yield and ultimate strengths as well as micro creep and yield strengths.

The thermal properties of interest are the CTE α, thermal conductivity k, specific heat at constant pressure c_p and diffusivity $D = \frac{k}{\rho c_\mathrm{p}}$, of which all vary with temperature; α and c_p directly, whereas k and D inversely. The CTE is the most important property for optomechanical design and is defined as

$$\alpha = \frac{\Delta L}{L \Delta T} \tag{2.7}$$

where L is a length scale and T a temperature, i.e. the CTE is the expansion per temperature difference. A low CTE minimizes the effect of thermal gradients on dimensional change of components. The CTE of adjacent components can therefore be matched to minimize thermally induced strains. The thermal conductivity is the amount of heat transmitted per unit of time through a unit of area per unit of temperature gradient. High thermal conductive materials are desirable to minimize gradients, though, alternatively low conductive materials can be used to isolate components from heat sources. The specific heat or heat capacity per unit mass is the quantity of heat required to change the temperature of a unit mass of material one Kelvin under constant pressure. A material with high specific heat required more heat to cause a temperature change. The thermal diffusivity determines the rate at which a non-uniform temperature distribution reaches equilibrium. Commonly used figures of merit are the steady-state and transient distortion coefficients, $\frac{\alpha}{k}$ and $\frac{\alpha}{D}$, respectively. The former is a measure of the total thermal displacement for a given steady-state thermal input, whereas the latter indicates the time for a thermal distortion to dissipate per unit of temperature gradient. Material properties of the most commonly used materials in optomechanical design and accompanying figures of merit are shown in Chapter A.

2.5 Optomechanical design principles

Principles of optomechanical design and material selection tend to minimize the adverse effects of attributes such as contacts stress due forces imposed by temperature changes or accelerations, while retaining component function, location and alignment. The design objectives for a mirror-mount system are to eliminate or minimize local mounting forces/moments which might distort the optical surface, transfer support loads without distorting the optical alignment, compensate for or minimize strains caused by

differential thermal distortion and return the mirror-mount system elastically to the predetermined shape and position after subjection to accelerations, shocks and vibrations [See e.g. 1–3]. In general the mechanical architecture should in general be optimized to make it as symmetrical as possible with respect to the optical axis in order to have low and symmetrical thermomechanical deformation. Additionally, the materials have to be chosen to have effective CTEs that are as low as possible, where effective means that only some critical dimensions/orientations need to be controlled which is not only a function of the bulk material properties but also of the distance, architecture and compensation techniques. Finally, the design should be optimized to limit the thermal load and associated impact in the system as much as possible, i.e. limit internal power requirements, separate the sub-system requiring stability and those generating perturbations and increase the thermal time constant by reducing the internal and external thermal exchange while also increasing the thermal inertia. The most important attributes contributing to the performance of typical optomechanical designs are structural and kinematic design, thermal stability and athermalization, vibration control and material selection.

Material selection

The material selection depends on the system performance requirements and factors such as size, weight, mechanical loading, environment, number of components and cost. Material selection is an important design consideration for structural components, connectors, refractors and reflectors. For the interest of this thesis the focus is on structural components and reflectors. The material selection of reflective components, i.e. mirrors, scanners, reflecting prisms and gratings among others, is often combined with that of the structural components if it's weight is of essential importance. For that purpose special materials are created, such as beryllium (Be) or metal matrix composites (MMC). To minimize the disturbances from heat loads materials with extreme low thermal expansion properties can be used, such as Zerodur, Ultra-Low Expansion Glass (ULE) or Invar. Structural components, those that mechanically support and connect the optical components, must be relatively stiff, dimensionally stable and preferably thermally matched to the optics (both in relation to expansion and conduction). More information about the material properties and figures of merit can be found in Chapter A or [e.g 3].

Structural efficiency and dynamic stiffness

Structural efficiency in optomechanical support structures is determined by the stiffness-to-weight ratio. The fundamental elastic eigenfrequency f_{n} is one important index, determined by both stiffness and weight. For a single DOF system it is defined as

$$f_{\mathrm{n}} = 2\pi\sqrt{\frac{k}{m}} \tag{2.8}$$

where k is the stiffness and m the mass. The highest fundamental frequency is obtained by selecting materials with a high specific stiffness $\frac{E}{\rho}$ and a high geometric efficiency $\frac{I}{V}$, where I is the mass moment of inertia and V the volume. The dynamic properties of a mechanical structure are characterized by its eigenfrequencies and corresponding eigenmodes. To avoid mechanical resonance the eigenfrequencies of the structure should not approach the frequency of the dynamic loads. For the purpose of limiting excitation under random vibrations, the fundamental elastic eigenfrequency must be as high as possible.

Semi-kinematic design

In the design of an optical support structure it is not necessary to limit deflections at all parts of the structure. As long as the optical components are aligned compared to each other the performance is retained, this is called insensitive optical design. The support structure of an optomechanical component must maintain the components' position relative to other components within given design tolerances. The tolerances associated with optical systems generally require extremely accurate mechanical mounting of the surfaces to achieve this precision. In order to circumvent extreme manufacturing requirements one can use kinematic methods, which provide simple, accurate and repeatable mounting techniques in a low stress condition. When mounting mirrors, ideally, the contact with the body occurs at points such that moments cannot be exerted.

Every rigid body possesses six DOFs, any body which is constrained in more than six DOFs is over constrained, and hence, is likely to have uncertainties in the position or be distorted from its stress-free condition. Real kinematic mounts violate the theoretical assumption of infinite stiff material and infinitely small contact points. Therefore, semi-kinematic mounts are often adopted. Semi-kinematic design principles tend to reduce the elastic contact stress by replacing the point contacts by small contact areas (e.g. thin flexures) and tend to be able to increase the number of supports without overconstraining. Additionally, guidance of motion is provided without any play or backlash providing a unique location of the body at all times.

In order to avoid large stresses and deformation of the surface, finite-sized contact areas are used. In order to allow for CTE variations between mirrors and mounts, flexures are frequently used. A symmetric design with equal compliances keeps the optical elements centered when temperature changes. The flexures allow the component to decenter during survival conditions and return to the center afterwards. As point contacts are omitted, stresses due to shocks are highly reduced. Typical designs are stiff tangentially and axially, though compliant in the radial direction. Flexural design is free of stick-slip and friction effects, has less hysteresis than rolling or sliding contacts and is more robust to adverse environmental effects such as extreme temperatures, vacuum and abrasive dust. Additionally, it requires no maintenance. The thermal center ideally coincides with the center of gravity of the mirror, such that rotational symmetry tends to keep the center of the mirror fixed in relation to the optical system. The real benefit of a semi-kinematic mount is in the uncoupling of the optic's internal behaviour from its mount behaviour. If the mount support moves, the optic moves only in a rigid body sense, with no distortion of the optic itself,

leading solely to pointing errors and not to image quality. Though, thermal gradients will still cause distortions.

Athermal design

One of the most important environmental factors that can lead to distortions are thermal effects. Heat transfer takes place by radiation, convection and/or conduction. Optomechanical instruments are sensitive to thermal influences, which can cause optical component misalignments and mirror deformations. The supporting structures transmit both mechanical and thermal distortions from the frame to the mirror. In comparison to other considered loads, the thermal effects cause a relatively large magnitude of rigid body effects. The deformation of a mirror from its nominal shape causes wavefront errors that degrade the optical performance.

Athermal optomechanical design indicates that the design is able to maintain its optical performance under temperature changes. In general, three types of thermal distortion effects can be considered, that are

- distortions in the optical element due to the (change in) material properties, i.e. the CTE, spatial variation in the CTE, thermal distortion index (ratio of CTE over the thermal conductivity $\frac{\alpha}{k}$) and the thermal diffusivity D,
- distortions in the optical element due to the manner in which the element is mounted, which is primarily due to the difference in CTE between the mount and the optical component, and lastly
- distortions induced in the optical support structure or housing causing a loss of optical alignment.

Temperature gradients, especially radial temperature gradients, can be considered as the main source of potential problems in mirror design; a sudden change in temperature is likely to develop temperature gradients from the surface to the mount. Due to thermal expansion optical components move with respect to each other. The curvature of a mirror also scales with temperature and hence, if the structure's material and that of the apparatus are the same, effects of temperature differences can be minimized.

The thermal behaviour of a system can area-wise be divided in a heat source, heat transfer area and location where the optical performance is affected. A source, either hot or cold, can for example be an actuator, light source or change in environmental temperature. Source placement can be crucial in thermomechanical design. Any position in the component or material that will not move with change of temperature is called a Thermal Center (TC). With neatly constrained systems, a TC can be located as of interest.

To minimize disturbances from thermal deformations one can use different approaches [See: 4]:

- minimization of heat transfer using insulation for which one can select materials low thermal conductive materials or simply by minimizing mechanical contact areas,

- minimization of heat transfer by using components in direct contact with each other as they generally have a larger thermal resistance compared to solid materials,
- minimization of temperature gradients by good thermal conductivity, leading to a homogeneous temperature field,
- using a large thermal capacity minimizing the effects of change in temperature, since the source is too small to heat the system significantly, or
- additionally, but not preferable, the heat transfer can be actively controlled using heaters/coolers.

2.6 STOP analysis

The flow down of requirements in the typical optomechanical design, or tolerancing, to the various subsystems is done by experience and with much iteration as design teams negotiate for rebalancing of the allocations. This is done because prediction of an optical system's performance requires the use of optical design software with imported mechanical analysis results. Image quality requirements are often recast as requirements on WFE for this purpose. Thus, performing design trades on system level performance is cumbersome. Integrated modeling supports engineering design and verification of high-level optical requirements for image quality and sensitivity. By linking predictive methods from multiple engineering disciplines one can compute more meaningful predictions of a system's performance and simultaneously improve the efficiency of the design process. While the mechanical design parameters are taken as design variables one can optimize for the system's optical performance.

In order to analyze the optical performance degradation due to thermal distortions a full STOP analysis method can be used. The process begins with a thermal analysis to determine steady-state temperature distributions, for different orientations or phases if necessary (e.g. hot and cold cases), see e.g. Figs. 2.1a and 2.1b. The temperature results are mapped from the thermal to the structural model (if the models are not the same), which is then used to predict distortions resulting from thermal loads, see Figs. 2.1c and 2.1d.

The displacements of surfaces that are of interest for the optical analysis are mapped to an optical model to predict the system optical performance. Alternatively, one can compute a sensitivity matrix that contains information about the change in performance of the optical system with respect to a unit change of motion of a deformation of the optical surfaces. The matrix relates the performance of the optical system due to any deformation and motions of the optical surfaces as long as they can be described by the rigid body motions and Zernike polynomials used in the development of the optical sensitivity matrix.

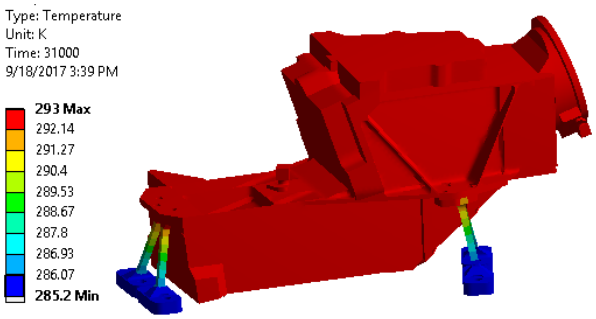

(a) Thermal gradient between the satellite and the average temperature of the UV-1.

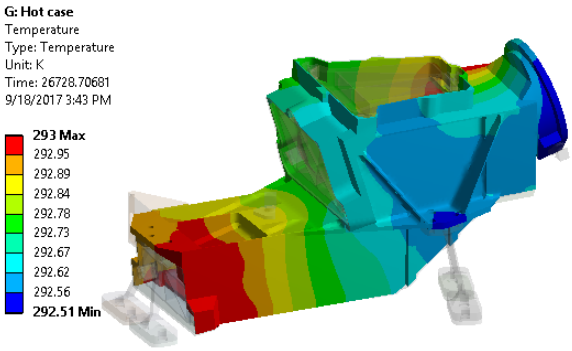

(b) Resulting temperature field on the UV-1.

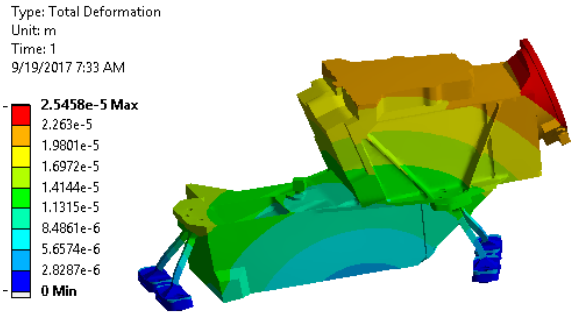

(c) Thermomechanical deformations due to hot load case. The maximum displacement is approximately 25 µm.

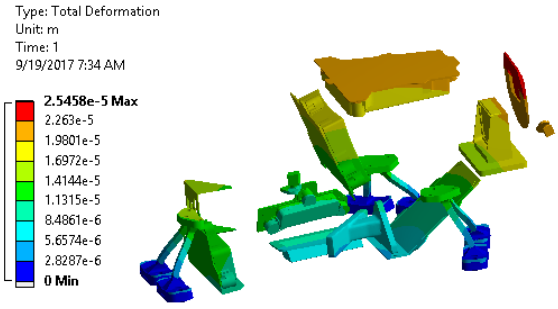

(d) Thermomechanical deformations illustrating the optical components and struts.

Figure 2.1.: Thermal loadcase of the Sentinel 5 UV-1, as shown in Fig. 1.2, mounted on the satellite. This case simulates the hotcase at the end of the instruments operational life, in which the absorption of heat is increased. The UV-1 is located in an environment in which panels and other instruments have deviating temperatures compared to the instrument. The instruments is mounted on a panel which has a temperature of 285 K, whereas two heaters ensure that the average temperature is 293 K. This is the integration temperature and hence this temperature will generally lead to a low amount of thermomechanical effects. Due to heatleaks in the system thermal gradients exist causing thermomechanical deformations of the optical components.

3. STRUCTURAL OPTIMIZATION

Structural optimization methods seek to find an optimal structural design, while subjected to a given set of loads, boundary conditions and constraints. Here optimal depends on the chosen performance criteria. Structural optimization increases the performance of structural designs and speeds up the design process. The existence of affordable and reliable structural analysis capabilities and the continuing growth of digital computing power has led to an increase in structural optimization research and applications.

Any description of an optimal design problem consists of a recognition of a need, an act of creation and a selection of alternatives. In a traditional description of the design phases, recognition of the original need is followed by a technical statement of the problem (problem definition), the creation of physical configurations (synthesis), the study of the configuration's performance using engineering science (analysis), and the selection of an alternative (optimization) [24]. The process ends with testing of the design against the original need. Thus, design optimization involves

1. the selection of a set of variables to describe the design alternatives,
2. the selection of an objective, as function of the design variables, which one seeks to minimize,
3. the determination of a set of constraints, as function of the design variables, which must be satisfied by any acceptable design, and
4. the determination of a set of values for the design variables, which minimize the objective while satisfying all the constraints.

Structural optimization methods are generally subdivided in size, shape and topology optimization as shown in Fig. 3.1. They differ in the type and number of design variables they use and thereby the amount of freedom provided to the optimizer. In size optimization a predefined design is optimized by altering some geometrical dimensions, e.g. cross-section widths or beam lengths, whereas in shape optimization the optimizer is able to change the shape of predefined boundaries, thereby extending the design freedom. Topology optimization opens up the design space even further by providing each finite element in the finite element analysis with a design variable. They are scaled to force each element to either solid or void material, thereby providing the ability to create holes that can result in complex, freeform and innovative designs. Topology optimization does not require any initial conceptual design and is able to generate the complex topologies expected in the design of thermally loaded optomechanical structures.

The topology optimization synthesis generally is incorporated in a gradient-based or heuristic optimization routine to select alternative designs. Heuristic methods are basically a rule of thumb based on nature

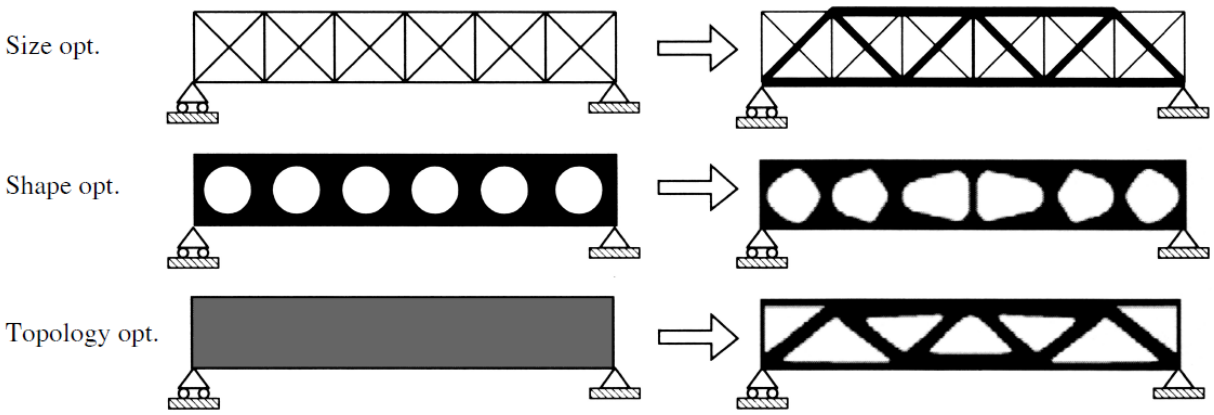

Figure 3.1.: Initial designs and resulting topologies of size, shape and topology optimization of a compliance bridge design problem [See: 15]. Whereas both size and shape optimization require an initial design, in topology optimization the design domain is often fully initiated with half-density material. Note the similarity between the size and topology optimization results, which indicates the well-known truss bridge is a near-optimal design.

.

or logic, e.g. genetic algorithms, that aim to find a good enough solution and often include randomization. Those methods are typically used to solve complex and/or discontinuous optimization problems that are difficult to solve to optimality. Because of the random nature of those methods, they are good at dealing with local optima. They generally require a high number of analysis and optimization iteration steps, do not have sensible convergence criteria and do not provide a systematic and flexible manner to include multiple constraints. Gradient-based methods require sensitivities of the response functions with respect to the design variables to determine an alternative design and are especially useful when an analytical description of the responses as a function of the design variables is known. These sensitivities are calculated analytically, semi-analytically or numerically, depending on available information. They generally ensure convergence within a reasonable number of iterations. Common for these approaches is that they represent smooth, differentiable problems that can efficiently be solved by well-proven gradient based optimization approaches, such as the optimality criteria, sequential quadratic programming, convex linearization approximation methods, quadratic approximations, steepest descent method or the Method of Moving Asymptotes (MMA) [25]. When working with difficult multiphysics non-selfadjoint optimization problems with varying signs on gradients or problems involving multiple nonlinear constraints the number of applicable optimization routines becomes limited. The MMA is often used and proved reliable in combination with non-selfadjoint optimization problems with multiple complex constraints.

The optomechanical design generally encompasses multiple physics and multiple nonlinear constraints. This study uses a topology optimization procedure in combination with the MMA gradient-based optimizer to maximize the design freedom and systematically find the optimal solution. The gradient-based optimization process is explained in more detail in Section 3.1, followed by a description of topology optimization procedures and application to optomechanical structures in Section 3.2.

3.1 Gradient-based optimization

The most generalized optimization problem in the negative null form is formulated as

$$\begin{aligned} \min_{\mathbf{s}} \quad & f(\mathbf{s}) \\ \text{s.t.} \quad & \mathbf{h}(\mathbf{s}) = \mathbf{0} \\ & \mathbf{g}(\mathbf{s}) \leq \mathbf{0} \\ & \mathbf{s} \in \mathscr{S} \subseteq \mathscr{R}^{\hat{n}} \end{aligned} , \tag{3.1}$$

where f is the objective function, $\mathbf{s}$ the design variables, $\mathbf{h}$, $\mathbf{g}$ the equality and inequality constraints, $\mathscr{S}$ the variable bound constraints and $\hat{n}$ the number of design variables [26]. Proper understanding of the boundedness of the design space as well as the optimality and constraint activity at a possible solution $\mathbf{s}_*$ are essential in the interpretation of an optimization result.

The optimality criteria states that, for a function of one variable: if a point s has a first derivative equal to zero and the second derivative at this point is positive, then s_* is a local optimum. Extending this to

a function of many variables involves the concept of local approximation of functions. The quadratic Taylor series approximations around $\mathbf{s}_0$ can be written in compact form as

$$\partial f \triangleq \nabla f(\mathbf{s}_0)\partial\mathbf{s} + \frac{1}{2}\partial\mathbf{s}^T\mathbf{H}(\mathbf{s}_0)\partial\mathbf{s} + \mathscr{O}\left(\|\partial\mathbf{s}\|^2\right), \tag{3.2}$$

where $\mathbf{H}$ is the Hessian matrix and $\mathscr{O}$ is the approximation error. The first order necessity states that at the optimum solution f_* for $\mathbf{s}_*$ by definition

$$\partial f_* = \nabla f(\mathbf{s}_*)\partial\mathbf{s}_* \geq 0, \tag{3.3}$$

hence all partial derivatives $\frac{\partial f}{\partial s_i}$ at $\mathbf{s}_*$ must be zero. The fist-order necessary condition for an unconstrained (or interior) local minimum states that if $f(\mathbf{s})$ has a local minimum at an interior point $\mathbf{s}_*$ and if $f(\mathbf{s})$ is continuously differentiable at $\mathbf{s}_*$, then $\nabla f(\mathbf{s}_*) = \mathbf{0}^T$, which can also be true at points that are not local minima (i.e. local maxima and saddle points).

Second-order information can indicate a sufficient condition, that is whether a stationary point is a local minimum. If $\mathbf{s}_\dagger$ is a stationary point of f, then

$$\partial f_\dagger = \frac{1}{2}\partial\mathbf{s}^T\mathbf{H}(\mathbf{s}_\dagger)\partial\mathbf{s}, \tag{3.4}$$

neglecting the higher order terms and accounting for $\nabla f(\mathbf{s}_\dagger) = \mathbf{0}^T$. If this quadratic form is strictly positive for all $\partial\mathbf{s} \neq 0$ then, $\mathbf{s}_\dagger$ is definitely a local minimum. Hence, the second-order sufficiency condition for an unconstrained local minimum states that if the Hessian matrix of $f(\mathbf{s})$ is positive-definite at a stationary point $\mathbf{s}_\dagger$, then $\mathbf{s}_\dagger$ is a local minimum. A square, symmetric matrix is positive-definite if and only if all its eigenvalues are positive.

Taking into account inequality constraints the necessary optimality conditions for a problem as Eq. (3.1), known as the Karush-Kuhn-Tucker (KKT) conditions [26], are

$$\begin{aligned} \mathbf{h}(\mathbf{s}_*) &= \mathbf{0} \\ \mathbf{g}(\mathbf{s}_*) &\leq \mathbf{0} \\ \nabla f_* + \boldsymbol{\mu}^T\nabla\mathbf{h}_* + \boldsymbol{\lambda}^T\nabla\mathbf{g}_* &= \mathbf{0}^T \\ \boldsymbol{\mu} &\neq \mathbf{0} \\ \boldsymbol{\lambda} &\geq \mathbf{0} \\ \boldsymbol{\lambda}^T\mathbf{g} &= 0 \end{aligned}, \tag{3.5}$$

where the minimizer $\mathbf{s}_*$ is assumed to be a stationary point and $\boldsymbol{\mu}$ and $\boldsymbol{\lambda}$ are the Lagrange multipliers related to the equality $\mathbf{h}$ and inequality constraints $\mathbf{g}$, respectively. Elaborated definition and explanation of Lagrange multipliers can be found in Chapter C. The second-order sufficiency conditions now state that if a KKT point $\mathbf{s}_*$ exists, such that the Hessian of the Lagrangian on the subspace tangent to the active constraints (both equalities and inequalities) is positive-definite at $\mathbf{s}_*$, then $\mathbf{s}_*$ is a local constrained minimum, i.e $\mathbf{s}_* = \mathbf{s}_\dagger$.

Typical optimization algorithms reach the solution of the problem in the limit, thus termination criteria are required. These criteria should address whether an acceptable estimate of the solution has been found, slow/no progress is encountered, an acceptable number of iterations has been exceeded, an acceptable solution does not exist or whether the algorithm cycles. One of the simplest criteria is the convergence test, that is

$$\|\mathbf{s}^{(k)} - \mathbf{s}^{(k-1)}\| \leq \varepsilon_{\nabla \mathbf{s}}, \tag{3.6}$$

where $\varepsilon_{\mathbf{s}}$ is a small constant value dependent on the application and k is the iteration number. Another termination criteria is convergence of the objective function

$$\|f^{(k)} - f^{(k-1)}\| \leq \varepsilon_{\nabla f} \tag{3.7}$$

in combination with a satisfactory positive-definiteness of the Hessian at $\mathbf{s}^{(k)}$. The constraints may be tested individually or collectively by checking whether

$$\|\mathbf{g}^{(k)}\| \leq \varepsilon_g. \tag{3.8}$$

Since the optimality criteria is the KKT conditions, equivalently, the termination criteria may also be imposed on the KKT norm, i.e.

$$\|\nabla f_* + \boldsymbol{\mu}^T \nabla \mathbf{h}_* + \boldsymbol{\lambda}^T \nabla \mathbf{g}_*\| \leq \varepsilon_{\text{KKT}} \tag{3.9}$$

3.2 Topology optimization

Topology optimization effectively optimizes the material layout within given design domains, while subjected to a given set of loads, boundary conditions and constraints in order to maximize a performance metric. The method, in combination with a non-linear optimization algorithm, has proven to be able to solve complex nonlinear multidisciplinary problems with multiple active conflicting constraints. Commonly used topology optimization approaches based on gradient-based optimization routines are the homogenization method [27], density-based approach [28] and (parametric) level-set methods [29–31], schematically illustrated in Fig. 3.2.

The homogenization method [27] replaces the material layout distribution problem by a sizing problem by considering that the macro structure consists of a periodic combination of microstructures. Each finite element is described by a base cell, the smallest repetitive unit of material for that structure. The cell's microstructure is parameterized by a single or multiple design variables. The evaluation of the effective constitutive parameters can thus be carried out by analysis of a single base cell, see Fig. 3.2. The homogenization method aims to effectively find the optimal microstructure for each cell minimizing the macrostructure's performance function. For manufacturability and optimality reasons this approach has long been considered unuseful for industrial applications.

Short after the introduction of the homogenization approach the Solid Isotropic Material with Penalization (SIMP) approach [28] was introduced. Starting as an artificial trick to simplify the homogenization

method and improve convergence, it was physically justified in a later stadium. In density based optimization methods a design variable is assigned to each finite element in the design domain, see Fig. 3.2. These one-variable material interpolation scheme approaches provide a continuous interpolation between solid and void with a penalization of intermediate density values. The SIMP penalization scheme is defined as

$$\begin{aligned} \rho_i &= s_i \rho_0 \\ E_i &= s_i^p E_0 \\ 0 \leq \underline{s}_i &\leq s_i \leq 1 \end{aligned} \tag{3.10}$$

where s_i is the design variable of finite element i, bounded between $\underline{s}_i$ and 1, and p is the penalization factor, generally $p = 3$. The solid material density and Young's modulus are denoted by ρ_0 and E_0 respectively and ρ_i and E_i are the penalized material properties of that specific element. Intermediate material properties can provide optimal performance depending on the objective function, though are unwanted from a manufacturing point of view. The penalization scheme forces the design towards solely solid and void elements. Additional filters or other restrictions are generally applied to the density approach in order to ensure well-posed and mesh independent solutions.

In contrast to density methods, level set approaches [29–31] define the geometry of the structure via the definition of a solid-void interface (isoline for 2D problems, isosurface for 3D problems). This boundary is defined by the zero level contour of a Level Set Function (LSF) $\phi(\mathbf{x})$. The structure is defined by the domain where the level set function takes positive values, that is

$$\rho = \begin{cases} 0 : \forall \mathbf{x} \in \Omega : \phi(\mathbf{x}) < 0 \\ 1 : \forall \mathbf{x} \in \Omega : \phi(\mathbf{x}) \geq 0 \end{cases}. \tag{3.11}$$

In many approaches the LSF is updated via the solution of the Hamilton-Jacobi equation using shape sensitivities, i.e.

$$\frac{\partial \phi}{\partial t} + V|\nabla \phi| = 0, \tag{3.12}$$

where t is a pseudo-time representing the evolution of the design in the optimization process and V is the velocity field or speed function. The function $V(\mathbf{x})$ at $\phi(\mathbf{x}) = 0$ represents the sensitivity of moving the boundary interface in its normal direction with respect to some objective function, thus V is a function of the design variables s. The geometry of this interface is clearly defined throughout the optimization process and allows explicitly formulating the response functions and boundary conditions on the interface.

Many variations of the method have been developed that generally differ by the way of discretization of the level set function, mapping of the level set field onto the mechanical model and by the type of updating scheme. An alternative of the Hamilton Jacobi equation, allowing the use of mathematical programming schemes, is the Parametric Level Set Method (PLSM), where one directly applies local changes to the LSF introducing local changes to the structure's topology. These PLSMs use a parameterization to describe the LSF using shape functions and expansion coefficients that are used as the design variables in gradient-based optimization routines, see Fig. 3.2.

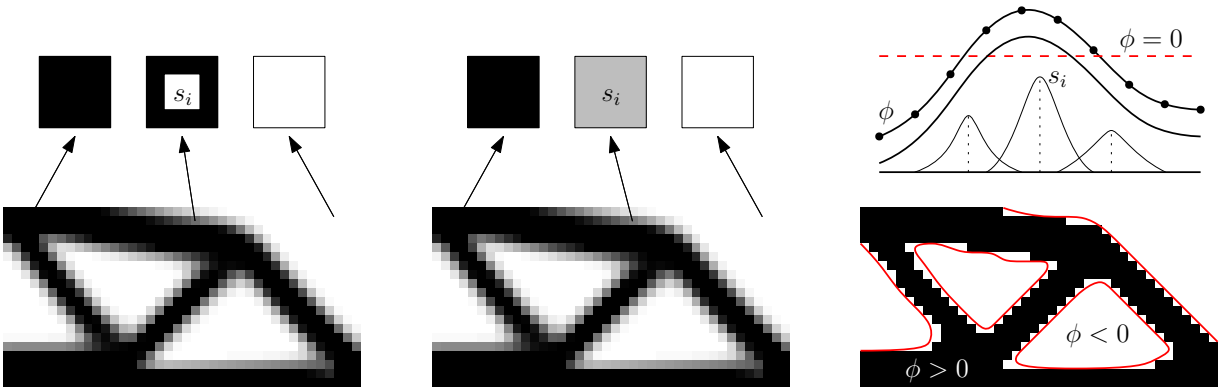

Figure 3.2.: Illustration of the benchmark cantilever topology optimization problem showing the differences in gradient-based topology optimization approaches: homogenization, density-based and level-set method (from left to right), respectively. The homogenization method applies a parameterization to the microstructe of each finite element, effectively optimizing the element stiffness matrix of each element. The density-based method applies a scale factor to each finite element, in combination with a chosen penalization scheme, optimizing each element to solid or void. The level set method defines the structures geometry by a solid-void interface, which is defined by the zero level contour of a level-set function (indicated in red). The parametric version describes this function using shape functions, which magnitudes are the design variables. The resulting topology is created using the 88 line Matlab code using the density-based method by `top(nelx,nely,volfrac,penal,rmin)` with `nelx = 40`, `nely = 20`, `volfrac = 0.5`, `penal = 3`, and `rmin = 2`) [See: 32]. Results of the homogenization method and level-set method are thus schematics to illustrate the principle.

It appears that the various approaches are not that different as most of them are Eulerian based and use the same sensitivity information and almost all make use of filtering techniques to ensure smooth convergence and mesh-independency. Differences appear in the types of updating schemes and whether and how length scales are controlled. Based on the difficulty of the optomechanical design problem, i.e. multiphysical, non-selfadjoint problems with multiple nonlinear response functions, and the ease of implementation and usage, this study uses a density-based approach in combination with the MMA optimization routine.

Topology optimization of optomechanical systems: state-of-the-art

The influence of the mentioned typical requirements in optomechanical design for the use in topology optimization have previously been researched. This includes thermal loads and prescribed temperature differences on stiffness problems [e.g. 33–36] and the application to the design of thermomechanical compliant mechanisms [e.g. 37, 38]. The fundamental eigenfrequency as a response function has been thoroughly investigated [e.g. 39–42]. The mentioned studies propose solutions for problems related to localized modes and oscillations of the optimization due to mode switching. This study uses a combined SIMP and linear penalization scheme to overcome local modes and applies the mean eigenvalue to circumvent mode switching. The formulation of the coupled thermomechanical discretized equilibrium equations and modal analysis, topology optimization formulation and sensitivity analysis of a generalized response function are described in Chapter 4.

Topology optimization has previously shown its benefits in the design of mirror mounts for optical performance. For example the minimization of SFEs under static [43, 44] and thermal loads [45] and mass minimization while constraining SFEs as well as the fundamental eigenfrequency [46]. Furthermore, semi-kinematic flexible mirror mounts are topology optimized by, Hu et al. [47] who minimize surface form errors subjected to both static and thermal loads while constrained by a minimum natural eigenfrequency, and Van der Kolk et al. [48], who achieve optimal damping characteristics at source frequencies. The system optical performance metrics have not been included in the topology optimization framework yet.

Coupled multicomponent topology optimization can aid in exploiting the components interactions. Simultaneous topology optimization of multiple components has mainly focused on layout design and combined topology and joint location optimization [e.g. 49, 50]. Topology optimization involving component interactions to improve a system performance has previously been investigated by Jin et al. [51], with the focus on simultaneous optimization of multiple coupled actuator mechanisms to minimize the coupling interaction. However, this study was restricted to a single physical discipline. Thus additional work coupling multiple components and physics taking into account the systems performance is required.

4. FORMULATION OF COUPLED THERMOMECHANICAL ANALYSIS FRAMEWORK FOR TOPOLOGY OPTIMIZATION

A schematic of an opto-thermo-mechanical system consisting of two mirrors is shown in Fig. 4.1. Both domains consist of a linear-elastic homogeneous isotropic material with conductivity k_i, Young's Modulus E_i, Poisson's ratio ν_i, density ρ_i and Coefficient of Thermal Expansion (CTE) α_i. For every optical component a coordinate systems is required to express the displacements of the optical surfaces. Additionally, each optical element (including propagation in medium with constant refractive index) has a coordinate system to track the position and angle of rays with respect to the optical axis. The response of a system to a given load case depends on the optical design and properties as well as the component's domain geometries, boundary conditions, structural layout and material properties. The optical design includes the optical path lengths $\mathbf{d}$, incident angles ϕ and beam properties. Any system response function depends on the response of multiple components to a given load case, where the response of each domain directly depends on the layout of material, denoted by the design variables $\mathbf{s}$, or indirectly through other responses.

The design variables, one belonging to every finite element in the domain, are bounded by a lower and upper bound, i.e. $0 < \underline{\mathbf{s}} \leq \mathbf{s} \leq 1$, where $\underline{\mathbf{s}}$ has a very small value (to avoid numerical issues) denoting the absence of material and, $\bar{\mathbf{s}} = 1$ providing the element with the assigned initial material properties. Each design variable can have any intermediate value within the given bounds. The material properties are interpolated using a penalization function as discussed in Section 4.1. Sections 4.2 to 4.4 discuss the thermomechanical and modal analysis, followed by the respective sensitivity analyses.

4.1 Penalization scheme

Intermediate density values are penalized to force the design variables to approach their bounds and achieve interpretable and manufacturable designs. All material properties are either a linear or nonlinear functions of the design variables depending on the applied penalization scheme. Common interpolation functions for the Young's Modulus $R_{\mathrm{E}}(\mathbf{s})$, the density $R_{\rho}(\mathbf{s})$, and conductivity $R_{\mathrm{k}}(\mathbf{s})$, are the SIMP and RAMP functions [52].

Large ratios of $\frac{R_{\rho}}{R_{\mathrm{E}}}$ for design variables with near zero densities should be avoided to prevent low-frequency eigenmodes localized in the void regions of the structure [49]. Therefore, this study applies a

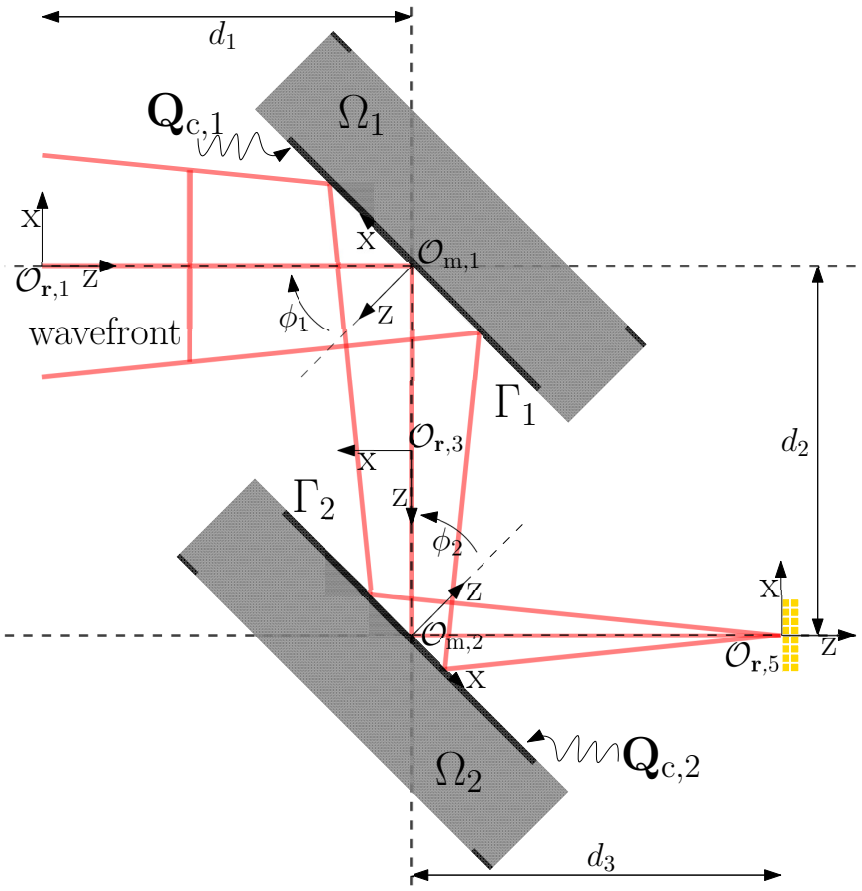

Figure 4.1.: Overview and nomenclature of a typical optical system. The incoming converging wavefront is deflected by the mirrors and focused onto a sensor. The design domain of each component $\Omega_i(E_i, k_i, \nu_i, \rho_i, \alpha_i)$ is shown in grey, with nondesign domain illustrated in black. Prescribed displacements $\mathbf{U}_\mathrm{b}$ and temperatures $\mathbf{T}_\mathrm{d}$, respectively, represent the housing rigid body effects and temperatures. The beam imposes thermal loads $\mathbf{Q}_\mathrm{c}$ onto the mirror surfaces. The position and deformations of mirror i are locally described using coordinate systems $\mathcal{O}_{\mathrm{m},i}$. An incoming wavefront is described by multiple rays, of which each rays' position and the angle is expressed in local coordinate system $\mathcal{O}_{\mathbf{r},i}$ with respect to the principal ray incoming on component i. Each mirror makes an angle ϕ_i with relation to the incoming principal ray. The initial optical path lengths of principal ray i is given by d_i.

continuously differentiable penalization scheme for $R_{\mathrm{E}}(\mathbf{s})$ and $R_{\mathrm{k}}(\mathbf{s})$, as proposed by Zhu et al. [49]. The function is a summation of a linear and SIMP interpolation term, that is

$$R_{\mathrm{E}} = R_{\mathrm{k}}(s) = qs^p + (1-q)\,s, \tag{4.1}$$

where p is a penalization parameter and q is a weight factor controlling the relative influence. This study consistently uses a power $p = 3$ and weight $q = 0.8$. The densities are scaled linearly, thus the volume and mass of an element depend linearly on the accompanying design variable. Using two adjustable parameters the method can effectively penalize intermediate densities and avoid spurious eigenmodes for low-density elements while keeping the penalization factor relatively low.

The thermal stress is given by

$$\sigma(s) = E(s)\,(\varepsilon_{\mathrm{m}} + \alpha\Delta T)\,, \tag{4.2}$$

where ε_{m} is the strain from applied forces, ΔT the applied temperature difference and $E(s)\alpha\Delta T$ the resulting thermal stress. Hence, the CTE itself is not penalized, though the thermal stresses are a nonlinear function of the design variables via the penalization of the Young's Modulus.

4.2 Thermomechanical equilibrium equations

The one-way coupled thermomechanical finite element discretized equilibrium equations, neglecting heat transfer by radiation and convection, are given by

$$\begin{bmatrix} \mathbf{K}(\mathbf{s}) & -\mathbf{A}(\mathbf{s}) \\ \mathbf{0} & \mathbf{H}(\mathbf{s}) \end{bmatrix} \begin{bmatrix} \mathbf{U} \\ \mathbf{T} \end{bmatrix} = \begin{bmatrix} \mathbf{F}(\mathbf{s}) \\ \mathbf{Q}(\mathbf{s}) \end{bmatrix}, \tag{4.3}$$

where $\mathbf{K}(\mathbf{s})$ is the global stiffness matrix, $\mathbf{H}(\mathbf{s})$ the global conductivity matrix and $\mathbf{A}(\mathbf{s})$ the global thermal expansion matrix converting the temperatures to equivalent thermal loads [53]. These global matrices are a function of the material layout. Depending on the considered loading conditions, the forces $\mathbf{F}(\mathbf{s})$ and applied heat flux $\mathbf{Q}(\mathbf{s})$ can become design dependent. The material properties are assumed to be independent of strain and temperature, thus both linear geometric and linear material models are applied. Furthermore, the loads are assumed to be independent of time, thus only steady state heat transfer and (quasi)-static forces apply.

Prescribed and free Degrees of Freedom (DOFs) sets are generally different for the mechanical and thermal problem. To express this in a convenient notation, one can separate the DOFs in terms of free and prescribed displacement DOFs a and b, as well as free and prescribed temperature DOFs c and d. Each domain can be a function of externally applied forces $\mathbf{F}_{\mathrm{a}}(\mathbf{s})$ and heat loads $\mathbf{Q}_{\mathrm{c}}(\mathbf{s})$, prescribed displacements $\mathbf{U}_{\mathrm{b}}(\mathbf{s})$ and temperatures $\mathbf{T}_{\mathrm{d}}(\mathbf{s})$, free displacements $\mathbf{U}_{\mathrm{a}}(\mathbf{s})$ and temperatures $\mathbf{T}_{\mathrm{c}}(\mathbf{s})$ as well as the reaction forces $\mathbf{F}_{\mathrm{b}}(\mathbf{s})$ and reaction heat loads $\mathbf{Q}_{\mathrm{d}}(\mathbf{s})$. For the sake of clarity we abbreviate the multiplications, such that for instance,

$$\mathbf{K}_{\mathrm{a}}\mathbf{U} \triangleq \mathbf{K}_{\mathrm{aa}}\mathbf{U}_{\mathrm{a}} + \mathbf{K}_{\mathrm{ab}}\mathbf{U}_{\mathrm{b}}. \tag{4.4}$$

For a single domain one can now write the partitioned discretized heat transfer and elasticity equilibrium equations as

$$\begin{aligned}\begin{bmatrix}\mathbf{K}_{aa} & \mathbf{K}_{ab}\\ \mathbf{K}_{ab}^T & \mathbf{K}_{bb}\end{bmatrix}\begin{bmatrix}\mathbf{U}_a\\ \mathbf{U}_b\end{bmatrix} &= \begin{bmatrix}\mathbf{F}_a\\ \mathbf{F}_b\end{bmatrix} + \begin{bmatrix}\mathbf{A}_{ac} & \mathbf{A}_{ad}\\ \mathbf{A}_{bc} & \mathbf{A}_{bd}\end{bmatrix}\begin{bmatrix}\mathbf{T}_c\\ \mathbf{T}_d\end{bmatrix}\\ \begin{bmatrix}\mathbf{H}_{cc} & \mathbf{H}_{cd}\\ \mathbf{H}_{cd}^T & \mathbf{H}_{dd}\end{bmatrix}\begin{bmatrix}\mathbf{T}_c\\ \mathbf{T}_d\end{bmatrix} &= \begin{bmatrix}\mathbf{Q}_c\\ \mathbf{Q}_d\end{bmatrix}.\end{aligned} \tag{4.5}$$

Note that the design variable dependency has been left out, and will be left out from now on for compact notation. The equilibrium equations, Eq. (4.5), are solved to obtain both temperature and displacement fields.

4.3 Modal analysis and mean eigenvalue

The natural dynamic properties (neglecting damping) of a structure are found using a modal analysis by solving the eigenvalue problem

$$(\mathbf{K} - \lambda_i \mathbf{M})\,\phi_i = 0 \quad \text{for} \quad i = 1,2,..,n \tag{4.6}$$

for each unknown eigenvalue λ_i and corresponding mode shape ϕ_i. Here i is the mode of interest and n the number of DOFs. In this eigensystem the characteristic value equals the squared radial eigenfrequency, i.e. $\lambda_i = \omega_i^2$. All modes are mass normalized satisfying

$$\phi_i^T \mathbf{M} \phi_j = \delta_{ij} \quad \text{for} \quad i,j = 1,2,...,n. \tag{4.7}$$

In order to maximize or constraint the minimum fundamental frequency, the mean eigenvalue [39] is used as a response function. The mean eigenvalue combines the $\tilde{m}$ lowest eigenfrequencies of the structure, calculated as

$$f(\mathbf{s}) = \sum_{i=1}^{\tilde{m}} \frac{1}{\lambda_i}. \tag{4.8}$$

This form ensures that the first elastic resonant frequency is the main contributor and the influence of modes with a higher eigenfrequency quickly decreases. Thus, this closely resembles a pure natural eigenfrequency constraint, though ensures the absence of mode switching.

4.4 Sensitivity analysis

For any response f, the sensitivities with respect to $\mathbf{s}$ must be determined to enable gradient-based optimization. The focus is first on the response that depends on the thermomechanical analysis. Adjoint

sensitivity analysis is efficient due to the large number of design variables, and therefore we augment the response function as

$$\begin{aligned} f = f\left(\mathbf{s}, \mathbf{U}_\mathrm{a}, \mathbf{U}_\mathrm{b}, \mathbf{F}_\mathrm{a}, \mathbf{F}_\mathrm{b}, \mathbf{T}_\mathrm{c}, \mathbf{T}_\mathrm{d}, \mathbf{Q}_\mathrm{c}, \mathbf{Q}_\mathrm{d}\right) \\ - \boldsymbol{\lambda}_\mathrm{a}^T \left(\mathbf{K}_\mathrm{a}\mathbf{U} - \left(\mathbf{F}_\mathrm{a} + \mathbf{A}_\mathrm{a}\mathbf{T}\right)\right) \\ - \boldsymbol{\lambda}_\mathrm{c}^T \left(\mathbf{H}_\mathrm{c}\mathbf{T} - \mathbf{Q}_\mathrm{c}\right). \end{aligned} \tag{4.9}$$

Using the adjoint method to solve the sensitivities of the objective function in relation to the variables for which a solve is required, the total derivative in relation to the design variables is

$$\begin{aligned} \frac{\mathrm{d}f}{\mathrm{d}\mathbf{s}} = \frac{\partial f}{\partial \mathbf{s}} + \frac{\partial f}{\partial \mathbf{F}_\mathrm{a}}\frac{\partial \mathbf{F}_\mathrm{a}}{\partial \mathbf{s}} + \frac{\partial f}{\partial \mathbf{U}_\mathrm{b}}\frac{\partial \mathbf{U}_\mathrm{b}}{\partial \mathbf{s}} + \frac{\partial f}{\partial \mathbf{Q}_\mathrm{c}}\frac{\partial \mathbf{Q}_\mathrm{c}}{\partial \mathbf{s}} + \frac{\partial f}{\partial \mathbf{T}_\mathrm{d}}\frac{\partial \mathbf{T}_\mathrm{d}}{\partial \mathbf{s}} \\ - \boldsymbol{\lambda}_\mathrm{a}^T \left(\frac{\partial \mathbf{K}_\mathrm{a}}{\partial \mathbf{s}}\mathbf{U} + \mathbf{K}_\mathrm{ab}\frac{\partial \mathbf{U}_\mathrm{b}}{\partial \mathbf{s}} - \frac{\partial \mathbf{F}_\mathrm{a}}{\partial \mathbf{s}} - \frac{\partial \mathbf{A}_\mathrm{a}}{\partial \mathbf{s}}\mathbf{T} - \mathbf{A}_\mathrm{ad}\frac{\partial \mathbf{T}_\mathrm{d}}{\partial \mathbf{s}}\right) \\ - \boldsymbol{\lambda}_\mathrm{c}^T \left(\frac{\partial \mathbf{H}_\mathrm{c}}{\partial \mathbf{s}}\mathbf{T} + \mathbf{H}_\mathrm{cd}\frac{\partial \mathbf{T}_\mathrm{d}}{\partial \mathbf{s}} - \frac{\partial \mathbf{Q}_\mathrm{c}}{\partial \mathbf{s}}\right) \end{aligned} \tag{4.10}$$

by forcing the Lagrange multipliers to satisfy

$$\begin{bmatrix} \mathbf{H}_\mathrm{cc} & -\mathbf{A}_\mathrm{ac}^T \\ \mathbf{0} & \mathbf{K}_\mathrm{aa} \end{bmatrix} \begin{bmatrix} \boldsymbol{\lambda}_\mathrm{c} \\ \boldsymbol{\lambda}_\mathrm{a} \end{bmatrix} = - \begin{bmatrix} \left(\frac{\partial f}{\partial \mathbf{T}_\mathrm{c}}\right)^T + \mathbf{H}_\mathrm{cd}\left(\frac{\partial f}{\partial \mathbf{Q}_\mathrm{d}}\right)^T \\ \left(\frac{\partial f}{\partial \mathbf{U}_\mathrm{a}}\right)^T + \mathbf{K}_\mathrm{ab}\left(\frac{\partial f}{\partial \mathbf{F}_\mathrm{b}}\right)^T \end{bmatrix}. \tag{4.11}$$

Equation (4.11) shows that the Lagrange multipliers related to the free displacement DOFs depend on the sensitivity of the objective function f with respect to the free displacement DOFs as well as the sensitivity of the response in relation to the reaction forces. Equivalent relations hold for the Lagrange multipliers $\boldsymbol{\lambda}_\mathrm{c}$ related to the free temperature DOFs. In case the objective function does not explicitly depend on the reaction forces or reaction heat loads, the terms $\frac{\partial f}{\partial \mathbf{F}_\mathrm{b}}$ and $\frac{\partial f}{\partial \mathbf{Q}_\mathrm{d}}$ vanish.

Furthermore, the terms $\frac{\partial \mathbf{K}_\mathrm{ab}}{\partial \mathbf{s}}\mathbf{U}_\mathrm{b}$ and $\frac{\partial \mathbf{H}_\mathrm{cd}}{\partial \mathbf{s}}\mathbf{T}_\mathrm{d}$ in Eq. (4.10) vanish when the prescribed displacements or the prescribed temperatures are zero. Whenever the prescribed displacements or temperatures are design independent, that is $\mathbf{U}_\mathrm{b}$ or $\mathbf{T}_\mathrm{d}$ is not a function of $\mathbf{s}$, the terms $\mathbf{K}_\mathrm{ab}\frac{\partial \mathbf{U}_\mathrm{b}}{\partial \mathbf{s}}$ or $\mathbf{H}_\mathrm{cd}\frac{\partial \mathbf{T}_\mathrm{d}}{\partial \mathbf{s}}$ and $\mathbf{A}_\mathrm{ad}\frac{\partial \mathbf{T}_\mathrm{d}}{\partial \mathbf{s}}$ vanish. In case the mechanical and thermal loads are not design dependent, $\frac{\partial \mathbf{F}_\mathrm{a}}{\partial \mathbf{s}}$ and $\frac{\partial \mathbf{Q}_\mathrm{c}}{\partial \mathbf{s}}$ have no contributions.

For this research, loads and boundary conditions are assumed to be design independent and the responses solely depends on the displacement field. Thus, Eq. (4.10) can be simplified to

$$\frac{\mathrm{d}f}{\mathrm{d}\mathbf{s}} = -\boldsymbol{\lambda}_\mathrm{a}^T \left(\frac{\partial \mathbf{K}_\mathrm{a}}{\partial \mathbf{s}}\mathbf{U} - \frac{\partial \mathbf{A}_\mathrm{a}}{\partial \mathbf{s}}\mathbf{T}\right) - \boldsymbol{\lambda}_\mathrm{c}^T \frac{\partial \mathbf{H}_\mathrm{c}}{\partial \mathbf{s}}\mathbf{T}, \tag{4.12}$$

where the Lagrange multipliers now have to satisfy

$$\begin{bmatrix} \mathbf{H}_\mathrm{cc} & -\mathbf{A}_\mathrm{ac}^T \\ \mathbf{0} & \mathbf{K}_\mathrm{aa} \end{bmatrix} \begin{bmatrix} \boldsymbol{\lambda}_\mathrm{c} \\ \boldsymbol{\lambda}_\mathrm{a} \end{bmatrix} = \begin{bmatrix} \mathbf{0} \\ -\left(\frac{\partial f}{\partial \mathbf{U}_\mathrm{a}}\right)^T \end{bmatrix}. \tag{4.13}$$

The sensitivities of the mean eigenvalue, as described in Eq. (4.8), with respect to the design variables are

$$\frac{\mathrm{d}f(\mathbf{s})}{\mathrm{d}\mathbf{s}} = \sum_{i=1}^{\tilde{m}} -\frac{1}{\lambda_i^2}\boldsymbol{\phi}_i^T \left(\frac{\partial \mathbf{K}}{\partial \mathbf{s}} - \lambda_i \frac{\partial \mathbf{M}}{\partial \mathbf{s}}\right) \boldsymbol{\phi}_i. \tag{4.14}$$

The sensitivities of the global matrices can be derived element wise using direct differentiation. With this, all the sensitivities have been determined up until the term $\frac{\partial f}{\partial \mathbf{U}_\mathrm{a}}$, which will be discussed in Chapter 5, after the considered optimization problem and response functions have been introduced.

5. OPTICAL PERFORMANCE MEASURES AND SENSITIVITIES

This section describes various optical performance metrics relevant for the analysis of reflective optical systems. First, the SFE response will be discussed. Most commonly the SFE is expressed by the Root Mean Square Error (RMSE) of the deformed configuration in relation to the undeformed or a predefined configuration [13]. For 3D unit disk surfaces the surface errors are often expressed in Zernike polynomials, which have the same form as the types of optical aberrations often observed. For diffraction limited flat or spherical single-mirror systems there exists a simple relation between the RMSE and the Strehl ratio, the peak aberrated image intensity compared to the maximum attainable intensity using an unaberrated system. The conversion factor relating wavefront to surface error is a simple scalefactor. Though, for complex mirrors or multi-mirror systems the WFE becomes a function of the SFEs and can only be determined by ray tracing techniques.

To analyze a multi-component system, the deformed surfaces can be approximated by a fit to obtain the optical surface misalignments, i.e. rigid body movements and SFE. Next, the ray transfer matrix analysis can be used to track the position and angle of a paraxial ray though a multi-component system, leading to a measure for the averaged positional accuracy. In order to track the rays, all system properties, i.e. optical paths lengths, incident angles and specific properties of the optical components, as well as component transfer functions and misalignments should be known. Finally, the spot size is quantified by the mean average deviation of all rays with respect to the averaged spot position.

5.1 Surface form error

The RMSE is the standard deviation of the deformed surface from the ideal surface and is a global measure for SFE. The deformed surface is constructed from the out of plane displacements $\mathbf{U}_z$, which is fitted to a smooth surface represented by the fitted out of plane displacements $\hat{\mathbf{U}}_z$ using a Linear Least Squares Regression (LLSR) scheme [54] such that

$$\hat{\mathbf{U}}_z = \mathbf{G}\mathbf{U}_z, \tag{5.1}$$

where $\mathbf{G}$ is the fit matrix, see Fig. 5.1. The fit matrix is constructed as

$$\mathbf{G} = \mathbf{V}\mathbf{Y} = \mathbf{V}\left(\mathbf{V}^T\mathbf{V}\right)^{-1}\mathbf{V}^T, \tag{5.2}$$

where $\mathbf{V}$ is the Vandermonde matrix. This matrix consists of the terms of a geometric progression and evaluates a polynomial at a set of points, the surface nodal x-coordinates in this case. The tangential

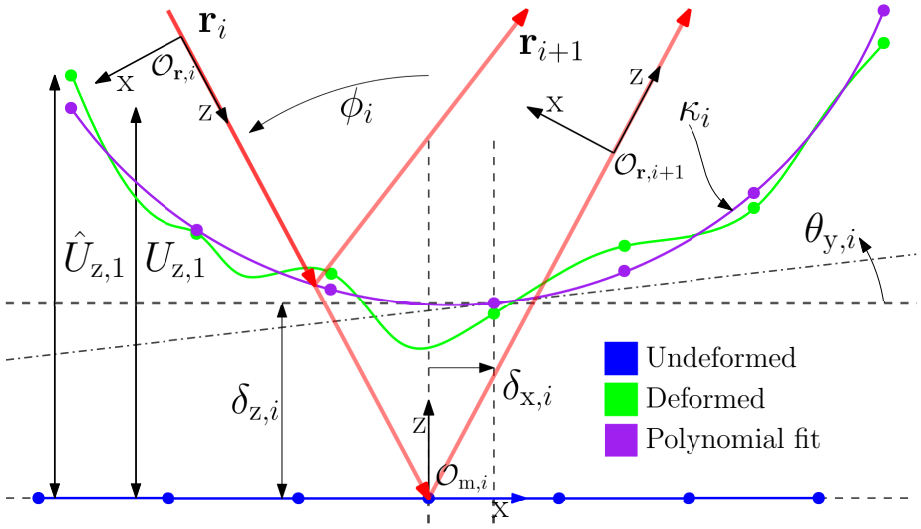

Figure 5.1.: Schematic representation of a generalized surface in undeformed (blue) and deformed (green) configuration. A least-squares polynomial fit through the deformed surface (purple) is used to extract the surface misalignments, that are the tangential and out of plane misalignments, δ_{x} and δ_{z} as well as the rotational misalignment θ_{y} and curvature κ. The component specific properties and misalignments δ cause the input ray $\mathbf{r}_i$, with incident angle ϕ_i, to change into $\mathbf{r}_{i+1}$.

displacements are assumed negligible compared to the out of plane displacement, i.e. $||\mathbf{U}_x|| \ll ||\mathbf{U}_z||$, which ensures $\mathbf{V}$ is constant during the optimization and hence the least-squares fit is linear.

Vector $\mathbf{b}$ stores the coefficients of the least-squares fit (size depends on the order of the fitted polynomial) which will be used in Section 5.2. Matrix $\mathbf{Y}$ relates the out of plane displacements $\mathbf{U}_z$ directly to the coefficients of the least-squares solution, that is $\mathbf{b} = \mathbf{Y}\mathbf{U}_z$. The fitted displacements are related to the coefficients via $\hat{\mathbf{U}}_z = \mathbf{V}\mathbf{b}$. The nodal residuals of the LLSR fit, denoted by $\mathbf{R}$, are calculated as

$$\mathbf{R} = \mathbf{U}_z - \hat{\mathbf{U}}_z = (\mathbf{I} - \mathbf{G})\,\mathbf{U}_z, \tag{5.3}$$

where $\mathbf{I}$ is the identity matrix.

The surface RMSE equals the absolute residual between the deformed surface and the ideal surface. It is preferred to use the Mean Square Error (MSE) when using the response in gradients based optimization to avoid division by zero in the sensitivities. The MSE is defined as

$$f = \mathrm{MSE}\,(\mathbf{U}_a) = \frac{1}{\tilde{n}} \sum_{i=1}^{\tilde{n}} \left(U_{z,i} - \hat{U}_{z,i} \right)^2 = \frac{1}{\tilde{n}} \mathbf{R}^T \mathbf{R}, \tag{5.4}$$

where $\tilde{n}$ is the total number of nodes on the mirror face, $U_{z,i}$ is the observed and $\hat{U}_{z,i}$ the fitted out of plane displacement at nodal point i.

The sensitivities of the MSE in relation to the free displacements $\mathbf{U}_a$, as required in Eq. (4.13), equal

$$\frac{\partial f}{\partial \mathbf{U}_a} = \frac{\partial f}{\partial \mathbf{R}} \frac{\partial \mathbf{R}}{\partial \mathbf{U}_a} = \frac{2}{\tilde{n}} \mathbf{R}^T (\mathbf{I} - \mathbf{G})\,\mathbf{L}_z, \tag{5.5}$$

where $\mathbf{L}_z$ selects the appropriate DOFs of the surface of interest from the vector of free displacements, i.e. $\mathbf{U}_z = \mathbf{L}_z \mathbf{U}_a$.

5.2 Positional accuracy

Depending on the application, it is often essential that the image remains within certain bounds from the preferred position (e.g. within the boundaries of a sensor). Considering a situation where all optical components are symmetric around the optical axis, the positional error of ray j, here denoted by ε_j, depends on the radial distance and angle of the ray with respect to the optical axis when entering the system, which will be denoted by vector $\mathbf{r}_0$. Furthermore, it depends on all misalignments $\boldsymbol{\delta}_1, ..., \boldsymbol{\delta}_N$ of all reflective optics (N is the number of components) and system specific constant parameters $\mathbf{p}$ (initial optical path lengths $\mathbf{d}$ and angles of incidence ϕ), thus $\varepsilon_j \left(\mathbf{r}_{0,j}, \mathbf{p}, \boldsymbol{\delta}_1, ..., \boldsymbol{\delta}_N \right)$.

The lower order misalignments of a surface i in 2D, are the change in curvature κ_i, the axial displacement $\delta_{z,i}$ (despace) the rotational misalignment $\theta_{y,i}$ (tip/tilt), and the radial displacement $\delta_{x,i}$ (decenter).

The decenter is directly calculated from the tangential displacement of the surface vertex. Other misalignments can be derived from the coefficients of the surface fit $\mathbf{b}_i$, which is calculated by the LLSR in Eq. (5.2) and shown in Fig. 5.1.

The radius of curvature $R_i = \frac{1}{\kappa_i}$ is assumed to be constant over the surface for small angular misalignments, that is $\left(\frac{\mathrm{d}z}{\mathrm{d}x}\right)_i \ll 1$, and defined as the reciprocal of the curvature κ_i, which equals $\kappa_i \approx \left(\frac{\mathrm{d}^2 z}{\mathrm{d}x^2}\right)_i$. The misalignments are stored as $\boldsymbol{\delta}_i = [R_i \ \theta_{\mathrm{y},i} \ \delta_{\mathrm{z},i} \ \delta_{\mathrm{x},i}]^T$. Determination of the despace, tip/tilt and radius of curvature from the surface fit do not take into account the radial displacement distribution nor the average radial displacement (decenter) of the mirror surface.

Ray transfer matrix analysis

Assuming paraxial rays, ray transfer matrix analysis can be used to describe the light path through a system by multiplying the vector representing the ray with the appropriate component transfer matrices, which depend on the component specific properties and the misalignments. A general misaligned paraxial transformation for component i, such as the mirror in Fig. 5.1, is denoted as

$$\begin{bmatrix} \mathbf{r}_{i+1} \\ 1 \end{bmatrix} = \begin{bmatrix} \mathbf{M}_i & \mathbf{E}_i \\ \mathbf{0} & 1 \end{bmatrix} \begin{bmatrix} \mathbf{r}_i \\ 1 \end{bmatrix}, \tag{5.6}$$

where $\mathbf{r}_i = [x_i \ \frac{\mathrm{d}x}{\mathrm{d}z}_i]^T$, with x_i and $\frac{\mathrm{d}x}{\mathrm{d}z}_i$ the distance and angle with respect to the optical axis i in the undeformed configuration. The ray vector after component i, $\mathbf{r}_{i+1}$, is linearly related to the incoming ray $\mathbf{r}_i$ via the component specific transfer matrix $\mathbf{M}_i$, and the influence of the misalignments as contained in $\mathbf{E}_i$.

Using the first-order optical canonical operator theory [21] one can determine the influence of the misalignments of an optical component $\boldsymbol{\delta}_i$ on the position and angle of an incoming ray $\mathbf{r}_i$ [55]. The generalized transfer matrices for the elements used in this study, that are space propagation and reflective optics, are shown in Table 5.1. The space propagation transformation matrix assumes no aberrations or change in refraction index between optical components and the derivation of the mirror transformation matrix assumes perfectly reflecting surfaces without scattering, transmission or absorption.

The positional error ε_j after $\tilde{N}$ elements, considering an initial ray vector $\mathbf{r}_{0,j}$ and $\tilde{N}$ sequential optical elements[1] with accompanying misalignments $\mathbf{E}_i$, equals the distance from the optical axis after the last component, that is $\varepsilon_j = x_{\tilde{N}}$. The output ray vector equals

$$\mathbf{r}_{\tilde{N},j} = \mathbf{M}_{\mathrm{S}} \mathbf{r}_{0,j} + \mathbf{E}_{\mathrm{S}}, \tag{5.7}$$

[1] The number of optical elements in a system is generally larger than the number of optical components, since space propagation is also an optical element, i.e. $\tilde{N} \geq N$. In most optomechanical applications $\tilde{N} = 2N + 1$.

Table 5.1: General misaligned ray transfer matrices for space propagation and mirror surfaces [55]. Here R_i is the radius of curvature, $\delta_{\mathrm{z},i}$ and $\delta_{\mathrm{x},i}$ are despace and decenter misalignments, $\theta_{\mathrm{y},i}$ the tip/tilt contribution and d_i the optical path lengths of a principal ray i with angle of incidence ϕ_i on component i.

Element type	Free space	Mirror
$\begin{bmatrix} \mathbf{M}_i & \mathbf{E}_i \\ \mathbf{0} & 1 \end{bmatrix}$	$\left[\begin{array}{cc\|c} 1 & d_i - \frac{\delta_{\mathrm{z},i-1}}{\cos\phi_{i-1}} - \frac{\delta_{\mathrm{z},i+1}}{\cos\phi_{i+1}} & 0 \\ 0 & 1 & 0 \\ \hline 0 & 0 & 1 \end{array}\right]$	$\left[\begin{array}{cc\|c} 1 & 0 & 2\sin\phi_i\delta_{\mathrm{z},i} \\ -\frac{2\sec\phi_i}{R_i} & 1 & -2\left(\frac{\tan\phi_i\delta_{\mathrm{z},i}+\delta_{\mathrm{x},i}}{R_i} - \theta_{\mathrm{y},i}\right) \\ \hline 0 & 0 & 1 \end{array}\right]$

where the system transformation matrix and misalignment vector are

$$\mathbf{M}_{\mathrm{S}} = \prod_{i=0}^{\tilde{N}-1} \mathbf{M}_{\tilde{N}-i} \quad \text{and} \quad \mathbf{E}_{\mathrm{S}} = \sum_{i=1}^{\tilde{N}-1} \mathbf{E}_i \left(\prod_{j=0}^{\tilde{N}-i-1} \mathbf{M}_{\tilde{N}-j} \right) + \mathbf{E}_{\tilde{N}}. \tag{5.8}$$

Thus, the positional error of each ray is a function of all system and component optical properties and misalignments.

Averaged positional error

The absolute positional error of a single reflective optic, for the purpose of an uncoupled optimization, solely is a function of the misalignments of that specific component, that is

$$f_i = \hat{\varepsilon}_i^2 \left(\mathbf{U}_{\mathrm{a},i} \right) = \left(\frac{1}{m} \sum_{j=1}^{m} \varepsilon_j \left(\mathbf{r}_{0,j}, \boldsymbol{\delta}_i \right) \right)^2, \tag{5.9}$$

where $\hat{\varepsilon}_i$ is the average positional error due to misalignments of component i and m the number of rays in the system. For equivalent reasoning as in Eq. (5.4), the root is omitted. In most applications it is unlikely the positional error contributions have the same direction and hence superposition of the errors will lead to overdesign of the individual components. Therefore, generally the positional errors of independent sources are combined via the Root Sum Square (RSS).

The absolute positional error taking into account all the components' misalignments is defined as

$$f = \hat{\varepsilon}^2 \left(\mathbf{U}_{\mathrm{a},1}, ..., \mathbf{U}_{\mathrm{a},N} \right) = \left(\frac{1}{m} \sum_{j=1}^{m} \varepsilon_j \left(\mathbf{r}_{0,j}, \boldsymbol{\delta}_1, ..., \boldsymbol{\delta}_N \right) \right)^2 \tag{5.10}$$

The sensitivities of the positional error contribution of component i in relation to the free displacements of domain Ω_i are

$$\frac{\partial f_i}{\partial \mathbf{U}_{\mathrm{a},i}} = \frac{2}{m} \sum_{j=1}^{m} \varepsilon_j \left(\mathbf{r}_{0,j}, \boldsymbol{\delta}_i \right) \frac{\partial \varepsilon_j}{\partial \mathbf{U}_{\mathrm{a},i}} \tag{5.11}$$

and the sensitivities of the positional error using an integrated approach equals

$$\frac{\partial f}{\partial \mathbf{U}_{\mathrm{a},i}} = \frac{2}{m} \sum_{j=1}^{m} \varepsilon_j \left(\mathbf{r}_{0,j}, \boldsymbol{\delta}_1, ..., \boldsymbol{\delta}_N \right) \frac{\partial \varepsilon_j}{\partial \mathbf{U}_{\mathrm{a},i}}. \tag{5.12}$$

In both Eq. (5.10) and Eq. (5.12) the sensitivities of a single ray ε_j are

$$\frac{\partial \varepsilon_j}{\partial \mathbf{U}_{\mathrm{a},i}} = \frac{\partial \varepsilon_j}{\partial \boldsymbol{\delta}_i} \frac{\partial \boldsymbol{\delta}_i}{\partial \mathbf{U}_{\mathrm{a},i}}. \tag{5.13}$$

Note that $\frac{\partial f}{\partial \mathbf{U}_{\mathrm{a},i}}\left(\mathbf{U}_{\mathrm{a},1},...,\mathbf{U}_{\mathrm{a},N}\right)$, thus the sensitivities of the positional error with respect to the displacements of domain i depend on all displacements in the system. In contrary, the positional error due to component i only depends on the components' displacements, that is $\frac{\partial f_i}{\partial \mathbf{U}_{\mathrm{a},i}}\left(\mathbf{U}_{\mathrm{a},i}\right)$.

The sensitivities of the misalignments $\boldsymbol{\delta}_i$ are defined as

$$\frac{\partial \boldsymbol{\delta}_i}{\partial \mathbf{U}_{\mathrm{a},i}} = \begin{bmatrix} \frac{\partial \boldsymbol{\delta}_i^*}{\partial \mathbf{b}_i}\frac{\partial \mathbf{b}_i}{\partial \mathbf{U}_{\mathrm{a},i}} \\ \frac{\partial \delta_{\mathrm{x},i}}{\partial \mathbf{U}_{\mathrm{a},i}} \end{bmatrix}, \tag{5.14}$$

where $\boldsymbol{\delta}_i^* = [R_i \ \theta_{\mathrm{y},i} \ \delta_{\mathrm{z},i}]^T$. Corresponding sensitivity matrix $\frac{\partial \boldsymbol{\delta}_i^*}{\partial \mathbf{b}_i}$ is a transformation scaling the fit coefficients to the misalignments, this is defined as

$$\frac{\partial \boldsymbol{\delta}_i^*}{\partial \mathbf{b}_i} = \begin{bmatrix} \frac{\partial R_i}{\partial b_{i,1}} & \frac{\partial R_i}{\partial b_{i,2}} & \cdots & \frac{\partial R_i}{\partial b_{i,\tilde{k}}} \\ \frac{\partial \theta_{\mathrm{y},i}}{\partial b_{i,1}} & \frac{\partial \theta_{\mathrm{y},i}}{\partial b_{i,2}} & \cdots & \frac{\partial \theta_{\mathrm{y},i}}{\partial b_{i,\tilde{k}}} \\ \frac{\partial \delta_{\mathrm{z},i}}{\partial b_{i,1}} & \frac{\partial \delta_{\mathrm{z},i}}{\partial b_{i,2}} & \cdots & \frac{\partial \delta_{\mathrm{z},i}}{\partial b_{i,\tilde{k}}} \end{bmatrix}, \tag{5.15}$$

where $\tilde{k}$ is the order of the fitted polynomial. For a third order polynomial (parabola) $\tilde{k} = 3$ and

$$\frac{\partial \boldsymbol{\delta}_i^*}{\partial \mathbf{b}_i} = \begin{bmatrix} 0 & 0 & \frac{1}{\kappa_i} \\ 0 & 1 & 0 \\ 1 & 0 & 0 \end{bmatrix}, \tag{5.16}$$

where κ_i is considered constant over the surface. The order of the fit determines what type of aberrations can be accounted for. The term $\frac{\partial \mathbf{b}_i}{\partial \mathbf{U}_{\mathrm{a},i}} = \mathbf{Y}_i\mathbf{L}_{\mathrm{z},i}$ can be derived from Eq. (5.2) and $\frac{\partial \delta_{\mathrm{x},i}}{\partial \mathbf{U}_{\mathrm{a},i}} = \mathbf{L}_{\mathrm{x},i}$, where $\mathbf{L}_{\mathrm{x},i}$ picks the appropriate DOFs, i.e. $\delta_{\mathrm{x},i} = \mathbf{L}_{\mathrm{x},i}\mathbf{U}_{\mathrm{a},i}$.

5.3 Spot size and sensitivities

In order to measure the spot size one can perform ray tracing for multiple rays with different initial distance and angle from the optical axis, see Fig. 4.1. The average resulting deviation from the averaged positional error is a measure for the spot size. The spot size due to the misalignments of component i is defined as

$$f_i = \tilde{\varepsilon}_i\left(\mathbf{U}_{\mathrm{a},i}\right) = \frac{1}{m}\sum_{j=1}^{m}\left(\varepsilon_j - \hat{\varepsilon}_i\right)^2, \tag{5.17}$$

where ε_j is calculated according to Eq. (5.7) and $\hat{\varepsilon}_i$ via Eq. (5.9). For an integrated system optimization the spot size response is calculated by

$$f = \tilde{\varepsilon}\left(\mathbf{U}_{\mathrm{a},i},...,\mathbf{U}_{\mathrm{a},N}\right) = \frac{1}{m}\sum_{j=1}^{m}\left(\varepsilon_j - \hat{\varepsilon}\right)^2, \tag{5.18}$$

where $\hat{\varepsilon}$ is calculated via Eq. (5.10).

The sensitivities of the MSE spot size due to the misalignments of component i, with respect to the free displacements of domain Ω_i, as required to solve for the Lagrange multipliers Eq. (4.11), are

$$\frac{\partial f_i}{\mathbf{U}_{\mathrm{a},i}} = \frac{1}{m}\sum_{j=1}^{m}\left(\varepsilon_j - \hat{\varepsilon}_i\right)\left(\frac{\partial \varepsilon_j}{\partial \mathbf{U}_{\mathrm{a},i}} - \frac{\partial \hat{\varepsilon}_i}{\partial \mathbf{U}_{\mathrm{a},i}}\right), \tag{5.19}$$

where $\frac{\partial \hat{\varepsilon}_i}{\partial \mathbf{U}_{\mathrm{a},i}}$ is defined in Eq. (5.11) and $\frac{\partial \varepsilon_j}{\partial \mathbf{U}_{\mathrm{a},i}}$ is calculated using Eq. (5.13). Equivalently, the sensitivities of the MSE spot size taking into account all components' misalignments are

$$\frac{\partial f}{\mathbf{U}_{\mathrm{a},i}} = \frac{1}{m}\sum_{j=1}^{m}\left(\varepsilon_j - \hat{\varepsilon}\right)\left(\frac{\partial \varepsilon_j}{\partial \mathbf{U}_{\mathrm{a},i}} - \frac{\partial \hat{\varepsilon}}{\partial \mathbf{U}_{\mathrm{a},i}}\right), \tag{5.20}$$

where $\frac{\partial \hat{\varepsilon}}{\partial \mathbf{U}_{\mathrm{a},i}}$ is defined in Eq. (5.12).

6. NUMERICAL IMPLEMENTATION

This section describes practical considerations of the implementation. The initial conditions are set such that designs are initialized with a uniform density field that exactly satisfies the volume constraint. The optimization is solved using the Method of Moving Asymptotes (MMA) [25]. The optical performance measures are relatively sensitive to design changes. Therefore, the algorithm is set more conservative (the move limit `move` is set to 0.1) in order to avoid large jumps in the design space.

The optimization is subjected to termination criteria to circumvent infinite optimization or oscillation. The optimization is considered to be terminated when the design variables and objective function change less than a threshold and all constraints are met, that is

$$\begin{bmatrix} \frac{1}{\hat{n}}\sqrt{\left(\mathbf{s}^{(k)}-\mathbf{s}^{(k-1)}\right)^2} \\ \frac{1}{\hat{n}}\sqrt{\left(f(\mathbf{s})^{(k)}-f(\mathbf{s})^{(k-1)}\right)^2} \\ g_i(\mathbf{s}) \end{bmatrix} \leq \begin{bmatrix} \varepsilon_{\Delta \mathbf{s}} \\ \varepsilon_{\Delta \mathrm{f}(\mathbf{s})} \\ \varepsilon_{\mathrm{g}(\mathbf{s})} \end{bmatrix}, \tag{6.1}$$

where $\hat{n}$ is the number of design variables, k is the iteration number and $i = 1,2,...,\hat{m}$ with $\hat{m}$ the number of constraints.

In order to control the design complexity and to avoid mesh dependency and checkerboard patterns, a general mesh and element-type independent linear spatial filter are implemented [56]. The simplest spatial filter, as used in the presented study, is the linear filter with weights according to

$$w_{ij} = \begin{cases} \bar{r} - r_{ij} & \text{if} \quad \bar{r} < r_{ij} \\ 0 & \text{if} \quad \bar{r} \geq r_{ij} \end{cases}, \tag{6.2}$$

where $\bar{r}$ is the radius of the filter, taken equal to the size of a single element. The radius r_{ij} is the distance between the centroids of elements i and j and $\hat{n}$ is the number of active elements (equal to the number of design variables). The filtered variables are calculated as

$$\hat{\tilde{s}}_i = \frac{\sum_{j=1}^{\hat{n}} w_{ij}\tilde{s}_j}{\sum_{j=1}^{\hat{n}} w_{ij}}, \tag{6.3}$$

where $\tilde{\mathbf{s}}$ are the variables as updated by the MMA optimization algorithm. The filter does not take account of the element volumes as only structured meshes are used.

To stimulate full black-and-white designs, the filtered design variables are projected in the direction of their lower and upper bounds by a smooth Heaviside projection function [57–59]. The projected design variables are penalized by a projection parameter β around a threshold η, given by

$$s_i = \frac{\tanh(\beta\eta) + \tanh\left(\beta\left(\hat{\tilde{s}}_i - \eta\right)\right)}{\tanh(\beta\eta) + \tanh\left(\beta\left(1-\eta\right)\right)}. \tag{6.4}$$

All given values are constant during the optimization and no continuation strategy is used.

7. RESULTS

This section discusses three case studies applying the foregoing theory and demonstrates the validity of the proposed method. First, the focus is on the optimization of a single mirror mount to minimize SFEs while subjected to a homogeneous temperature field. Next, multiple cases are investigated to obtain mounting error insensitive designs. Finally, the proposed SDO method including the STOP analysis is tested on a two-mirror case.

7.1 Single-component surface form error minimization

The focus of this study is on the optimization of a flat mirror mount design subjected to a uniform temperature increase. The aim is to minimize the resulting SFE. Both the boundary conditions and eigenfrequency constraint play a dominant role in the possibility to improve the optical performance. The study verifies the single-component topology optimization procedure and investigates the influence of the eigenfrequency constraint on the resulting topology and performance.

Problem definition

The design domain Ω, as shown in Fig. 7.1, is subjected to an overall temperature increase $\Delta\mathbf{T}$, causing the domain to expand and deform. As there are no resulting unknown temperatures, there is no need to solve the heat equation. It is assumed the housing is subjected to the same temperature increase as the considered design domain. It is assumed that the design domain is mounted to a housing with different material properties. The resulting change in expansion is introduced in the design domain by application of known prescribed displacements on both fixtures.

The objective is to minimize the MSE of the optical surface Γ due to the overall thermal expansion of the underlying structure and the incompatibility with the housing, while constrained by a minimum mean eigenfrequency and maximum volume. Therefore, the mean eigenvalue Eq. (4.8) is adopted as a constraint such that the mean eigenvalue must be higher or equal than the minimum elastic mean eigenfrequency $\underline{\omega}_{\mathrm{n}}^2$. In order to investigate the influence of the eigenfrequency constraint, a parameter sweep is performed over a range of minimum eigenfrequency constraints. The range spans from minimum eigenfrequency constraints where the constraint is inactive up to values where the structure is unable to satisfy the constraint. Additionally, a constant volume constraint is added, in order to ensure a fair comparison.

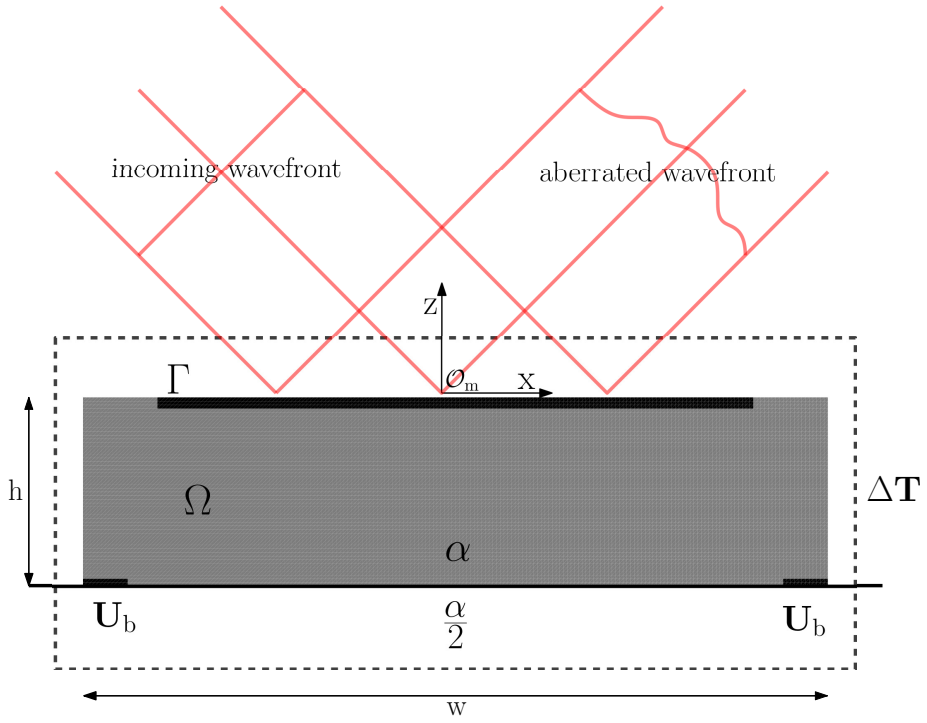

Figure 7.1.: Optical mount design domain Ω of width w, height h and thickness t with CTE α subjected to a uniform temperature increase $\Delta\mathbf{T}$. All non design space is indicated in black. Two fixtures are modelled as the interface with an infinitely stiff housing structure, which has CTE $\frac{\alpha}{2}$, and thus known prescribed displacements $\mathbf{U}_b$, which will induce SFE on surface Γ due to the boundary conditions and hence degrade the image quality of the incoming wavefront.

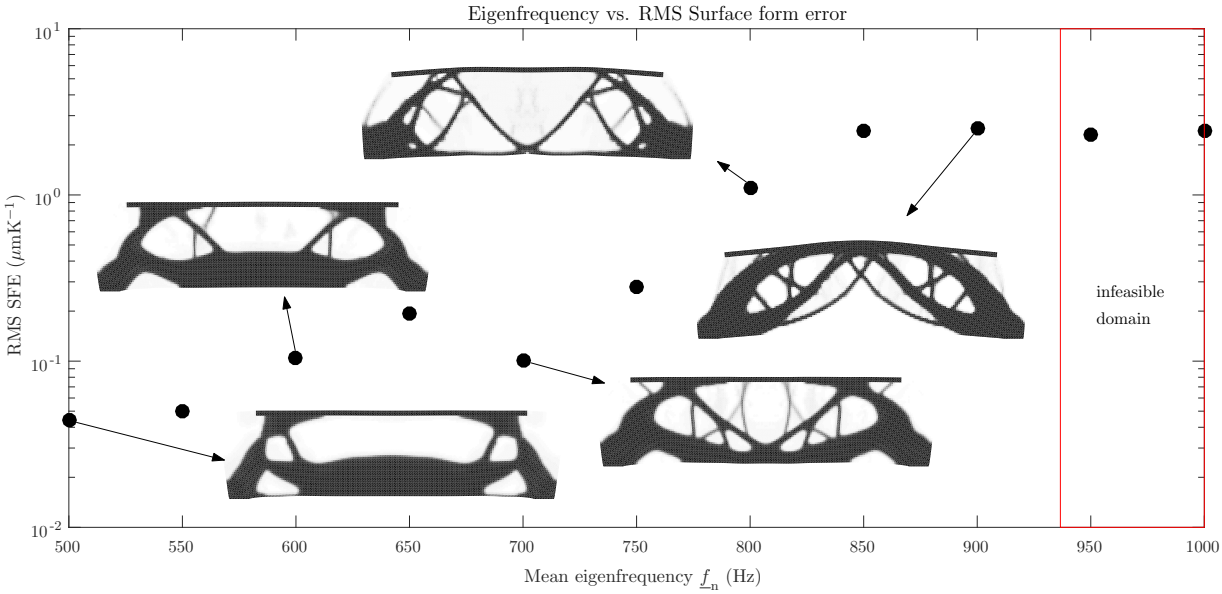

Figure 7.2.: Optimization results for Eq. (7.1) showing topologies (thermal deformations scaled by a factor 100) and RMS surface form error, in μmK^{-1}, for a range of minimum eigenfrequency constraints $\underline{f}_{\mathrm{n}}$.

The problem is formally stated as

$$
\begin{aligned}
\min_{\mathbf{s}} \quad & f = \mathrm{MSE}_{\Gamma}\left(\mathbf{U}_{\mathrm{a}}\right) = \left(\frac{1}{\tilde{n}}\mathbf{R}^{T}\mathbf{R}\right)_{\Gamma} \\
\text{s.t.} \quad & \mathbf{KU} = \mathbf{AT} \\
& \left(\mathbf{K} - \omega_i^2\mathbf{M}\right)\phi_i = 0 \quad \text{for} \quad i = 1,2,...,n \\
& \sum_{i=1}^{\tilde{m}} \frac{\underline{\omega}_{\mathrm{n}}^2}{\omega_i^2(\mathbf{s})} - 1 \leq 0 \\
& \frac{V_{\Omega}(\mathbf{s})}{\overline{V}} - 1 \leq 0 \\
& \mathbf{0} < \underline{\mathbf{s}} \leq \mathbf{s} \leq \overline{\mathbf{s}}
\end{aligned}
\tag{7.1}
$$

In this study $\tilde{m} = 6$ for all cases, to prevent the occurrence of mode switching.

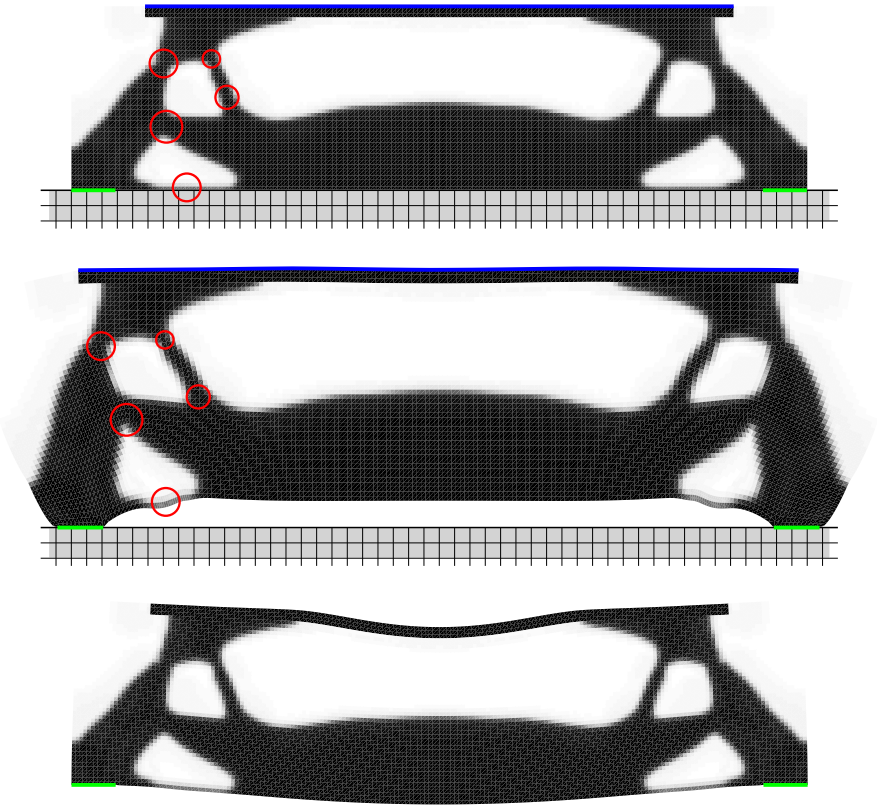

Figure 7.3.: Detailed view of the resulting topology of optimization problem Eq. (7.1) with an eigenfrequency constraint of 500 Hz both in undeformed and deformed (scaled by a factor 4). The figure illustrates the deformed compliant mechanism-like structure with rotation points indicated in red, mirror surface in blue and frame interface in green. Bottom figure shows the first modeshape of the structure. This is the bending mode, as expected.

Optimization results

Figure 7.2 shows the optimization results of Eq. (7.1) for a range of eleven different values for $\underline{f}_{\mathrm{n}}$ (note that $\underline{\omega}_{\mathrm{n}}^2 = 4\pi^2 \underline{f}_{\mathrm{n}}^2$). The required minimum eigenfrequency determines to what degree the optimizer is able to minimize the MSE. Cases with a higher eigenfrequency constraint generally result in higher SFE, as a compromise must be made. Note that above a critical frequency the resulting designs do not satisfy the eigenfrequency constraint. The resulting RMS SFEs are given in $\mu\mathrm{m}\,\mathrm{K}^{-1}$ because the RMS SFE scales linearly with respect to both $\Delta\mathbf{T}$ and the CTE α, thus the imposed temperature difference or CTE is irrelevant for the final topology.

The topology of the optimal design subjected to a mean eigenfrequency constraint of 500 Hz is shown in more detail in Fig. 7.3. Designs with a relatively low eigenfrequency constraint tend to possess compliant mechanism-like structures in order to counteract surface deformations. In general, structures with a lower required dynamic stiffness have clear rotation points (shown in red) and less small beams to support the mirror. The large amount of material underneath the mirror both stiffens the structure and forces the flexure-like structures, which are fixed to the frame (green), to bend outwards effectively flattening the surface (blue).

7.2 Mounting error insensitive mirror design

The following case aims to develop a design chart for mirror mounts of which the SFE is insensitive for mounting errors. Mounting errors in this case include differences in CTE between mount and housing, radial misalignments and tip/tilt misalignments of the fixtures. The following studies are considered:

Δ CTE a study of two load cases with a 1 K global temperature increase, while the CTE of the housing is $\frac{\alpha}{2}$ and 2α, respectively,

TILT a study consisting of two load cases where the fixtures are axially displaced 10 mm up and down and vice versa, causing the mirror to tilt and deform,

RADIAL a double load case study that investigate the influence of radial displacement of the fixtures both inwards and outwards 1 mm, and finally

ALL a study consisting of all 6 foregoing load cases.

All cases are optimized via a multi-objective formulation, constrained by a maximum volume and minimum natural eigenfrequency. A parameter sweep of the minimum eigenfrequency constraint gives insight in the working principles of the designs. The studies are formally stated as

$$\begin{aligned}
\min_{\mathbf{s}} \quad & \sum_{i=1}^{L} f^{[L]} = \mathrm{MSE}_{\Gamma}^{[L]}\left(\mathbf{U}_{\mathrm{a}}\right) = \left(\frac{1}{\tilde{n}}\mathbf{R}^{T}\mathbf{R}\right)_{\Gamma}^{[L]} \\
\text{s.t.} \quad & \mathbf{KU} = \mathbf{AT} \\
& \left(\mathbf{K} - \omega_i^2\mathbf{M}\right)\phi_i = 0 \quad \text{for} \quad i = 1,2,...,n \\
& \sum_{i=1}^{\tilde{m}} \frac{\omega_{\mathrm{n}}^2}{\omega_i^2(\mathbf{s})} - 1 \leq 0 \\
& \frac{V_{\Omega}(\mathbf{s})}{\overline{V}} - 1 \leq 0 \\
& \mathbf{0} < \underline{\mathbf{s}} \leq \mathbf{s} \leq \overline{\mathbf{s}}
\end{aligned} \quad , \tag{7.2}$$

where L is the load case considered.

Results of Eq. (7.2) are shown in Fig. 7.4. Figure 7.5 shows the influence of the loadcases on a resulting topology.

7.3 Two-mirror system spotsize minimization

This example studies the topology optimization of a two-mirror system subjected to thermal loads from a light source, as used in for example high-power laser or EUV applications. The study compares the following design approaches:

1. Uncoupled System (US) optimization, and
2. Coupled System (CS) optimization, where the integrated SDO approach is applied.

Both optimization procedures make use of a full STOP analysis, though only the integrated approach considers the component interactions and applies both system and component level constraints. Note that the uncoupled optimization problem is not a typical design approach used in practice, since it does consider system optical performances. The separate components are however artificially decoupled with relation to the optical performance, in order to investigate the difference with respect to the coupled SDO approach.

The optimization aims to minimize the spot size error due presumed known boundary conditions of the frame and thermal loads from the propagating beam, while bounded by a the position accuracy, mass, and eigenfrequency constraints. The main target is to investigate whether, and how, the components make use of the capability to interact and compensate for each others optical aberrations and how this may benefit the resulting optical performance.

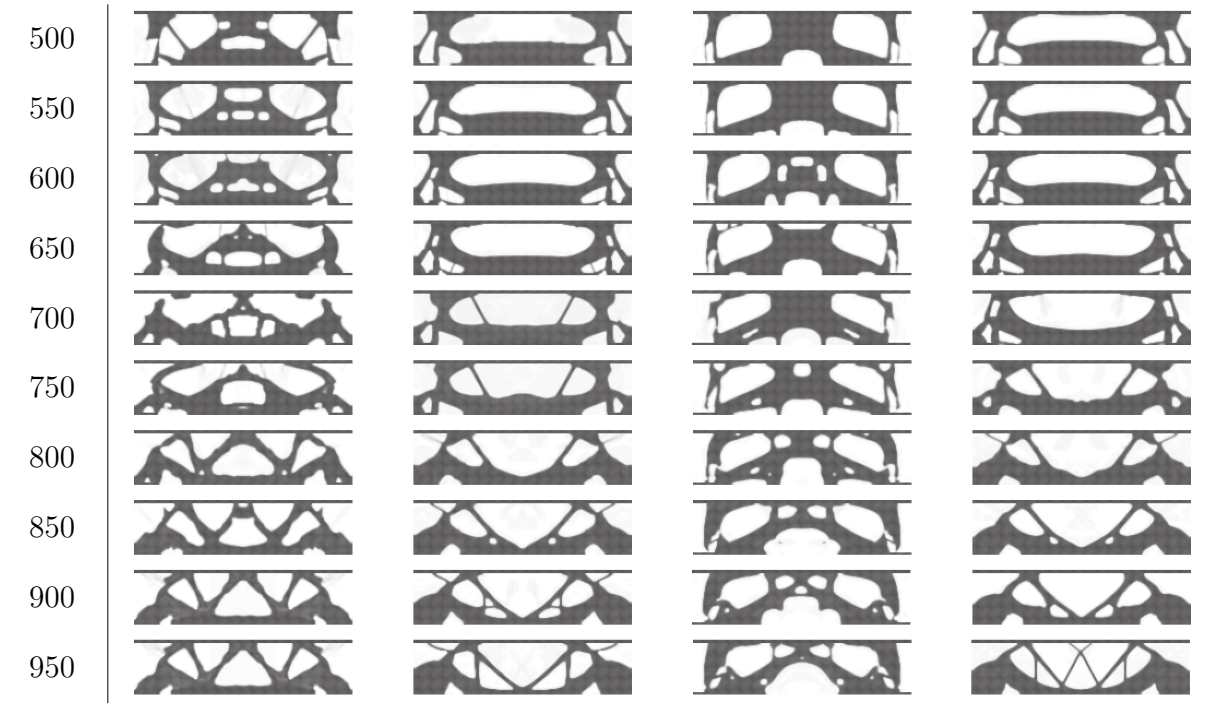

Figure 7.4.: Design chart illustrating the final topologies of four different multi-objective optimizations for a parameter sweep over the minimum eigenfrequency constraint $\underline{f}_{\mathrm{n}}$. Note the similarities between the radial misalignment and the homogeneous temperature increase studies.

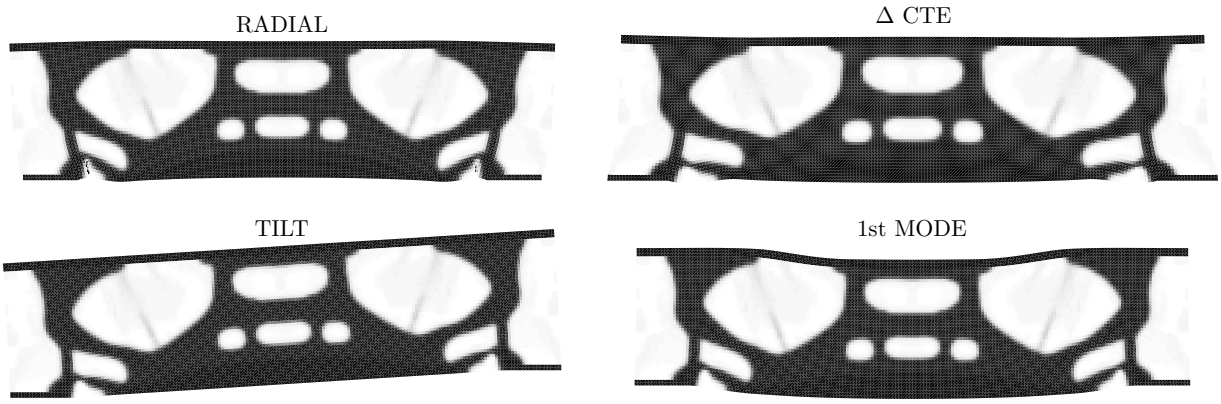

Figure 7.5.: Three of the six loadcases and the first modeshape of the 550 Hz case subjected to all loadcases. The topology effectively minimizes the sensitivity of the mount with respect to mounting errors. Deformations are highly scaled for illustration purposes.

Problem definition

Consider the schematic structural-thermal-optical system consisting of two flat reflecting surfaces supported by optical mounts with equal design domains as shown in Fig. 4.1. An incoming converging beam with perfect wavefront is reflected by two mirrors before it is focused onto a sensor with a theoretical spot size of zero (in real systems the minimum spot size is limited by the diffraction limit).

The fundamental maximum resolution or minimum spot size of any optical system is limited by the diffraction limit. The diffraction limit for the system as shown in Fig. 4.1, equals

$$\underline{D} = \frac{0.61\lambda_{\mathrm{l}}}{\mathrm{NA}} = \frac{0.61\lambda}{n_{\mathrm{r}} \sin\theta_{\mathrm{i}}} \tag{7.3}$$

where $\underline{D}$ is the first minimum in the Airy disk, NA the Numerical Aperture of the system, λ_{l} the wavelength of the light, n_{r} the index of refraction of the medium and θ_{i} the half-angle of the incoming light. Assuming perfect vacuum conditions, i.e. $n_{\mathrm{r}} = 1$, sunlight of $\lambda_{\mathrm{l}} = 550\,\mathrm{nm}$ (center of sunlight wavelength spectrum) the half-angle of the system of 3.8° and a NA of 0.0665, the diffraction limit of this system equals 8.3 µm.

The mesh is structured and consists of 10000 Quad 4 isoparametric elements (4 Gauss points and bilinear shape functions) per domain. Each domain consists of Aluminium, with Young's modulus $E = 70\,\mathrm{GPa}$, Poisson ratio 0.35, density $\rho = 2700\,\mathrm{kg/m^3}$, coefficient of thermal conductivity $k = 250\,\mathrm{W\,m^{-1}\,K}$ and CTE $\alpha = 25\,\mu\mathrm{m/mK^{-1}}$.

Both mirrors are subjected to known rigid body movements from the housing, which is modelled as an infinitely stiff interface. The interfaces of the first mirror mount are considered constant at 1 K difference with respect to ambient conditions, whereas the interfaces of the second mirror are constant at 0 K difference. The first mirror is subjected to a decenter rigid body effect of $\delta_{\mathrm{x},1} = 200\,\mu\mathrm{m}$ and a the same amount of despace misalignment. The left side of the second mirror is moved out by 200 µm and down the same magnitude. The right side of the second mirror interface is also moved out by 200 µm. This causes the second mirror to initially have a despace and tip/tilt error.

The heat load is modelled as a Gaussian profile over the surface, i.e.

$$Q_{\mathrm{c},i}(x) = \frac{Q_{0,i}}{\sigma\sqrt{2\pi}} e^{-\frac{1}{2}\left(\frac{x-\mu}{\sigma}\right)^2}, \tag{7.4}$$

where $Q_{0,i}$ is the maximum amplitude in domain i in Watts, x is the location on the surface, with $x = 0\,\mathrm{m}$ in the middle of the mirror surface, $\mu = 0\,\mathrm{m}$ and σ taken equal to 0.1 m. The input heat loads are normalized in relation to the maximum value at $x = 0$. The first mirror is subjected to a Gaussian heat profile with a maximum input of $Q_{0,1} = 0.1\,\mathrm{W\,m^{-1}}$. Assuming the first mirror absorbs 10 % of the heat load, the second mirror is subjected to a heat load with a 90 % maximum amplitude in relation to the first mirror.

Each design domain is constrained by an individual eigenfrequency constraint, as well as a maximum allowable RMS SFE in relation to a perfectly parabolic mirror. Therefore, the MSE SFE objective Eq. (5.4), has to be adopted as a constraint, taking into account proper scaling, i.e.

$$g_{\mathrm{MSE},i}(\mathbf{U}_{\mathrm{a},i}) = \log_{10}\left(\frac{1}{\tilde{n}}\mathbf{R}^T\mathbf{R}\right)_{\Gamma_i} \leq -\log_{10}\left(\overline{\mathrm{MSE}}_{\Gamma_i}\right) \tag{7.5}$$

Additionally, the system is forced to keep the position of the spot within a certain limit with respect to the optical axis, therefore the positional error, Eq. (5.9) or Eq. (5.10), depending on the optimization problem, has to be adopted as a constraint, such that

$$g_{\hat{\varepsilon},i}(\mathbf{U}_{\mathrm{a},i}) = \log_{10}\left(\hat{\varepsilon}_i^2\right) \leq -\log_{10}\left(\bar{\hat{\varepsilon}}_i^2\right) \tag{7.6}$$

for an uncoupled optimization, and

$$g_{\hat{\varepsilon}}(\mathbf{U}_{\mathrm{a},i},\ldots,\mathbf{U}_{\mathrm{a},N}) = \log_{10}\left(\hat{\varepsilon}^2\right) \leq -\log_{10}\left(\bar{\hat{\varepsilon}}^2\right) \tag{7.7}$$

for the coupled case. For an uncoupled optimization, the system positional error budget must be split up into the individual components, in this case such that the RSS value equals the total allowed system positional error, with equal weights per mirror, i.e. the positional error $\bar{\hat{\varepsilon}}$ of the integrated case equals the RSS of the positional tolerances $\bar{\hat{\varepsilon}}_1$ and $\bar{\hat{\varepsilon}}_2$.

In the uncoupled optimization each mirror is subjected to an individual maximum volume constraint, however, when performing integrated SDO the full system is subjected to a maximum volume constraint equal to the sum of the volumes of the individual components. In the example 50 % volume is allowed. This allows the optimizer to move material between domains for the benefit of the system performance. The constraint tolerance values, redefined into more relevant measures (e.g. $\underline{f}_{\mathrm{n}}$ instead of $\underline{\omega}_{\mathrm{n}}^2$), are given in Table 7.1.

The uncoupled optimization problem of the individual components minimizes the spot size as a function of the misalignments of the component of interest while satisfying the volume, positional error contribution and RMS SFE constraints. The US optimization is a combination of the optimization of mirror

one (U-M1), not taking into account the misalignments of the second mirror (U-M2) and vice versa. The problem is stated as

$$
\begin{aligned}
\min_{\mathbf{s}} \quad & f_i = \tilde{\varepsilon}_i^2\left(\mathbf{U}_{\mathrm{a},i}\right) = \frac{1}{m}\sum_{j=1}^{m}\left(\varepsilon_j - \hat{\varepsilon}_i\right)^2 \\
\text{s.t.} \quad & \begin{bmatrix}\mathbf{K} & -\mathbf{A}\\ \mathbf{0} & \mathbf{H}\end{bmatrix}_i \begin{bmatrix}\mathbf{U}\\ \mathbf{T}\end{bmatrix}_i = \begin{bmatrix}\mathbf{0}\\ \mathbf{Q}\end{bmatrix}_i \\
& \left(\mathbf{K} - \omega_i^2\mathbf{M}\right)\phi_i = 0 \quad \text{for} \quad i = 1,2,...,n \\
& g_{\hat{\varepsilon},i}(\mathbf{U}_{\mathrm{a},i}) = \log_{10}\left(\hat{\varepsilon}_i^2\right) + \log_{10}\left(\bar{\hat{\varepsilon}}_i^2\right) \leq 0 \\
& g_{\mathrm{MSE},i}(\mathbf{U}_{\mathrm{a},i}) = \log_{10}\left(\frac{1}{\tilde{n}}\mathbf{R}^T\mathbf{R}\right)_{\Gamma_i} + \log_{10}\left(\overline{\mathrm{MSE}}_{\Gamma_i}\right) \leq 0 \\
& g_{\omega,i}(\mathbf{U}_{\mathrm{a},i}) = \sum_{j=1}^{\tilde{m}} \frac{\underline{\omega}_{\mathrm{n}}^2}{\left(\omega_j^2\right)_i} - 1 \leq 0 \\
& g_{V,i}(\mathbf{U}_{\mathrm{a},i}) = \frac{V_{\Omega_i}}{\overline{V}} - 1 \leq 0 \\
& \mathbf{0} < \underline{\mathbf{s}} \leq \mathbf{s} \leq \bar{\mathbf{s}}
\end{aligned}
\tag{7.8}
$$

for $i = 1,...N$, where $N = 2$ for this system.

In the coupled case, the integrated SDO approach simultaneously optimizes all domains, thus objective function, system positional error and volume constraint are a function of the layout of all domains in the system, that is

$$
\begin{aligned}
\min_{\mathbf{s}} \quad & f = \tilde{\varepsilon}^2\left(\mathbf{U}_{\mathrm{a},1}, \mathbf{U}_{\mathrm{a},2}\right) = \frac{1}{m}\sum_{j=1}^{m}\left(\varepsilon_j - \hat{\varepsilon}\right)^2 \\
\text{s.t.} \quad & \begin{bmatrix} \mathbf{K} & -\mathbf{A} \\ \mathbf{0} & \mathbf{H} \end{bmatrix}_i \begin{bmatrix} \mathbf{U} \\ \mathbf{T} \end{bmatrix}_i = \begin{bmatrix} \mathbf{0} \\ \mathbf{Q} \end{bmatrix}_i \\
& \left(\mathbf{K} - \omega_i^2 \mathbf{M}\right)\phi_i = 0 \quad \text{for} \quad i = 1, 2, ..., n \\
& g_{\hat{\varepsilon}}\left(\mathbf{U}_{\mathrm{a},1}, \mathbf{U}_{\mathrm{a},2}\right) = \log_{10}\left(\hat{\varepsilon}^2\right) + \log_{10}\left(\bar{\hat{\varepsilon}}^{-2}\right) \leq 0 \\
& g_{\mathrm{MSE},i}\left(\mathbf{U}_{\mathrm{a},i}\right) = \log_{10}\left(\frac{1}{\tilde{n}}\mathbf{R}^T\mathbf{R}\right)_{\Gamma_i} + \log_{10}\left(\overline{\mathrm{MSE}}_{\Gamma_i}\right) \leq 0 \\
& g_{\omega,i}\left(\mathbf{U}_{\mathrm{a},i}\right) = \sum_{j=1}^{\tilde{m}} \frac{\underline{\omega}_{\mathrm{n}}^2}{\left(\omega_j^2\right)_i} - 1 \leq 0 \\
& g_V\left(\mathbf{U}_{\mathrm{a},1}, \mathbf{U}_{\mathrm{a},2}\right) = \frac{V_{\Omega_1} + V_{\Omega_2}}{\overline{V}} - 1 \leq 0 \\
& \mathbf{0} < \underline{\mathbf{s}} \leq \mathbf{s} \leq \overline{\mathbf{s}}
\end{aligned}
\tag{7.9}
$$

for $i = 1, 2$.

The lower bound on the design variables is $\underline{\mathbf{s}} = 10^{-3}$. The density filter radius equals the length of two finite elements and the Heaviside projection parameters are set to $\beta = 1.5$ and $\eta = 0.45$. The termination criteria are $\varepsilon_{\Delta\mathbf{s}} = 0.0015$, $\varepsilon_{\Delta\mathrm{f}(\mathbf{s})} = 0.002$, and $\varepsilon_{\mathrm{g}(\mathbf{s})} = 0.02$.

System optimization results

Figure 7.7 shows the resulting RMS spot size diameter as a function of iteration history for both optimization problems. The RMS spot size diameter versus the number of iterations for the coupled case using the SDO approach is illustrated in red. Whereas this approach requires only a single objective function, the uncoupled optimization consists of two separated optimization problems (one for each optical component), of which the RMS spot size diameter versus iteration number are shown in green and purple. In order to compare the system performances the RMS spot size diameter as a function of iteration history of the uncoupled system is calculated afterwards as shown in blue. Note that the optimizer is unaware of the US performance during the optimization process. The resulting topologies for both problems are displayed in Fig. 7.6, accompanied by the final performances as well as the system and component properties and constraint tolerances shown in Table 7.1.

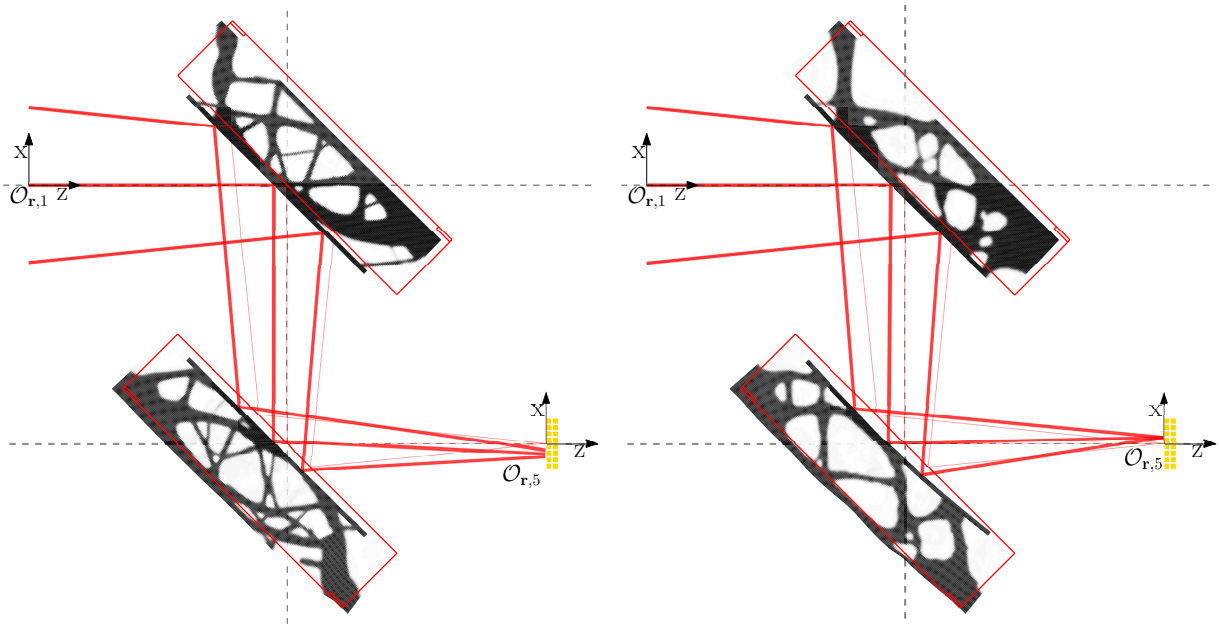

(a) Final topologies after the uncoupled optimization, resulting in an improved but not diffraction-limited system.

(b) Final topologies after the integrated SDO, resulting in a diffraction-limited system.

Figure 7.6.: Final topologies after the optimization of the system in Fig. 4.1. The system, topologies and deformations are not to scale (deformations scaled by a factor 100). The uncoupled optimization attempts to obtain two flat mirror surfaces, whereas the SDO is able to design both mirrors with respect to each other and utilize the curvature of C-M2 to correct for the defocus error introduced by C-M1.

Table 7.1: Performance of the obtained optomechanical systems, and properties of their individual mirror mounts: RMS spot size, RMS positional error, volume, RMS SFE, mean eigenfrequency rigid body movements and mirror curvature. The values between parentheses indicate the value at the first iteration.

	US	U-M1	U-M2	CS	C-M1	C-M2
Spot size $\tilde{\varepsilon} \div \underline{D}$ (-)	12.7	17.9	5.1	0.5		
Positional error $\hat{\varepsilon}$ (µm)	68.7	153.4	222.0	311.9		
$\overline{\hat{\varepsilon}}$ (µm)		223.6	223.6	316.2		
Volume V (dm^3)	161.1	80.4	80.6	161.2	84.0	77.1
$\overline{V}$ (dm^3)		80	80	160		
SFE (µm)		0.9	2.4		2.4	2.5
$\overline{\text{RMSE}}$ (µm)		2.5	2.5		2.5	2.5
Eigenfrequency f_n (Hz)		748	749		750	748
$\underline{f}_\text{n}$ (Hz)		750	750		750	750
Curvature R (km)		(-0.8) -4.1	(0.5) 7.2		(-0.8) -1.4	(0.5) 0.3
Tip/Tilt θ_y (µrad)		(0) 49	(275) 37		(0) 46	(275) 263
Despace δ_z (µm)		(312) 247	(-245) -210		(312) 263	(-245) -284
Decenter δ_x (µm)		(200) 212	(-50) -130		(200) 206	(-50) -58

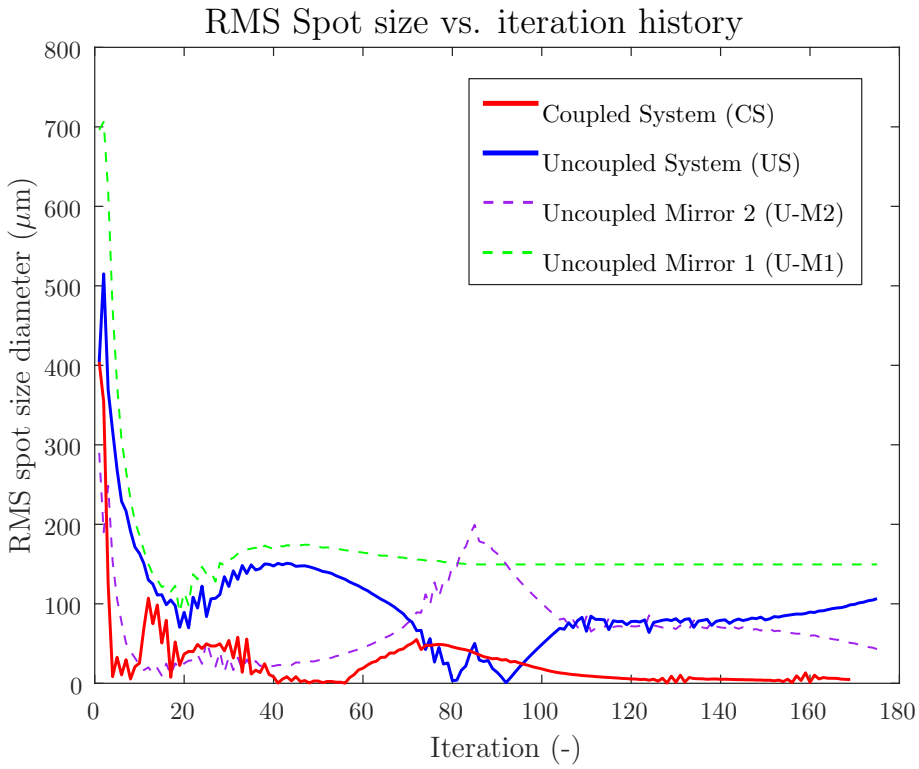

Figure 7.7.: RMS spot size diameter versus iteration history for the uncoupled system (US) as result of the individual contribution of mirror mount one (U-M1) and mirror mount two (U-M2), as well as the coupled system (CS). Note that the RMS spot size diameter of the US is constructed afterwards.

The optimization process has lowered the RMS spot size diameter from 0.4 mm in the first iteration to 106.5 µm and 4.7 µm for the uncoupled and coupled optimization approaches, respectively. Thus, the integrated SDO approach used for the coupled case proves a ratio of increase in performance of 22.6 times compared to the uncoupled method, equivalent to an improvement of 95.6 %. Note that the integrated SDO approach is able to lower the RMS spot size to below the diffraction limit of the system, that means it is not possible to further improve the optical performance measure with a geometry-based performance metric.

The two approaches result in some significant differences, see Table 7.1 and Fig. 7.6. Whereas the curvature of the first mirror in both approaches is brought as close as possible to zero, the second mirror in the coupled approach is made even more concave than its original shape. Note that the spot size of US is not simply the average of both mirrors. The positional error constraint of U-M2 is active, although the combined positional error of US is far below the allowable error. Both systems have satisfied the allowable mass, however, the integrated SDO has transferred mass from C-M2 to C-M1. The resulting temperature and Von Mises stress distributions of mirror C-M2 are illustrated in Figs. 7.8a and 7.8b. The stress distribution indicates that for the given loadcase the maximum yield stress of Aluminium, $\sigma_y \approx 250\,\text{MPa}$, is exceeded on multiple locations in the design leading to failure of the structure. High stresses mainly occur on the bottom, due to tension of the material as a consequence of the imposed boundary conditions of the frame, around the prescribed displacements $\mathbf{U}_{b,2}$, and within some thin flexures. Additionally, thermal stresses are present, clearly visible at the high temperature areas ($\mathbf{T} \approx 6\,\text{K}$). The exceeding of the yield stress for this load case is caused by the excessively large initial prescribed deformations and heat loads, not representable for industrial applications.

Figure 7.9 shows the first three modes of mirror mount C-M2. As expected from the topology the first mode is the first bending mode and the second mode is swaying of the body. The third mode shows large deformations of the optical surface and hence when the mount is subjected to vibrations of this eigenfrequency (e.g. micro-vibrations for other subsystems) this will high degrade the optical dynamic stability, that means a blurred image.

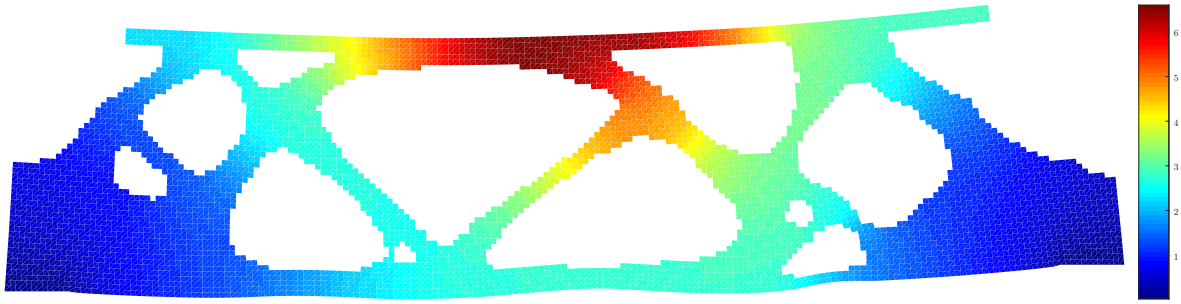

(a) Temperature distribution of mirror mount C-M2 in the deformed configuration. The fixtures are subjected to a constant temperature difference of 1 K. The maximum temperature due to the imposed thermal load is approx. 6.5 K. Note that the mount requires material underneath the mirror surface to conduct heat off the surface.

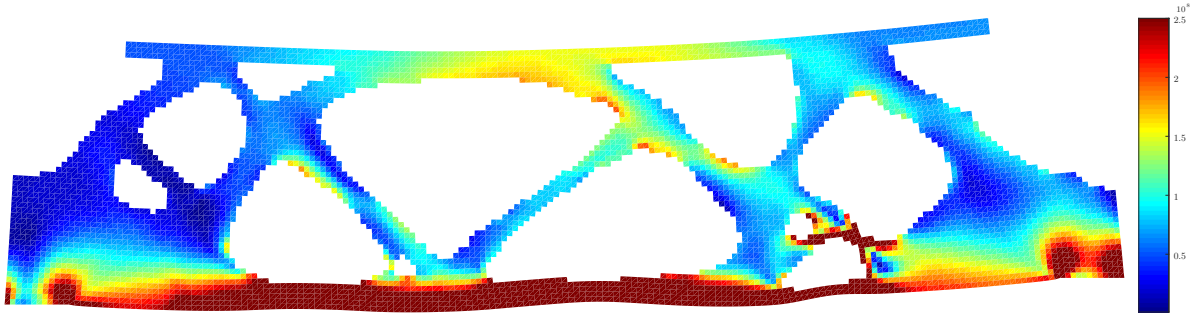

(b) Von Mises stress distribution of mirror mount C-M2 in the deformed configuration. The color bar is cut off at $\sigma_{VM} = 250\,\text{MPa}$. The red areas indicate failure of the structure by plasticity. The magnitudes of the resulting stress field is not representable for the stresses that occur in most optomechanical thermal loadcases, though the field shows the critical locations.

Figure 7.8.: Analysis results of component C-M2.temperature and stress. Deformed configurations are scaled a factor 100. Physical density threshold of $\mathbf{s} = 0.5$.

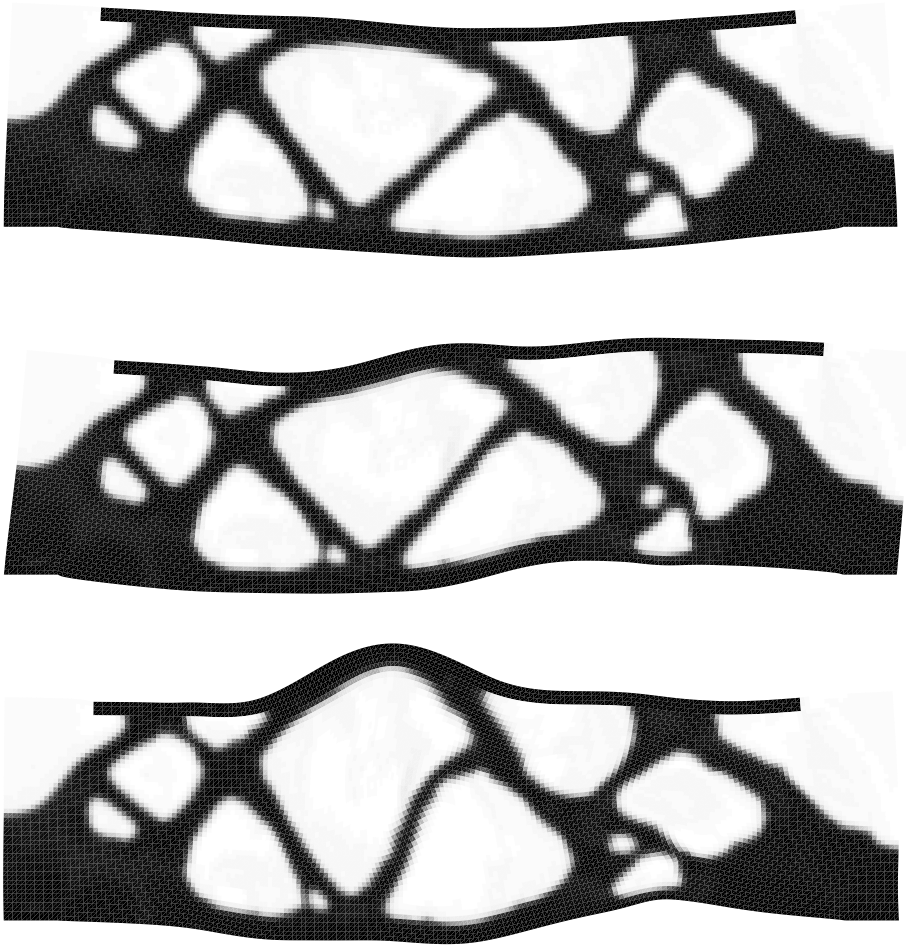

Figure 7.9.: First three modes (top to bottom) of mirror mount C-M2.

8. DISCUSSION, LIMITATIONS & RECOMMENDATIONS

Existing approaches for topology optimization of optomechanical systems focusses on the optimization of individual mirror mounts to minimize their surface deformations. This research extends this by

1. topology optimization of mirror mounts for the systems' optical performance expressed in terms of spot size and position accuracy using a full structural-thermal-optical performance analysis procedure, and
2. simultaneous topology optimization of multiple mirror mounts to exploit the interaction of aberrations between different components due to thermal loads and frame movements and minimize a system optical performance while constrained by dynamic stiffness, weight and optical performance measures, both on a component and system level.

The results of the first case study, shown in Fig. 7.2, indicate there is a certain bandwidth of minimum eigenfrequency constraint values that influence the ability of the optimizer to minimize the surface deformations. Thus, conflicting requirement tolerance values should be thoroughly investigated, as their limits can highly influence the topological layout and performance.

The second study shows that, as expected, different topologies result from different loadcases, though some loadcases result in comparable topologies as their structures have the same working principles. The multi-objective approach combining all loadcases appears to be effective; all response functions are lowered. Though, control over how much the response functions are lowered compared to each other and how to fairly compare the results of different loadcases has not been addressed yet.

The results of the third study indicates that whereas the uncoupled optimization aims to design two perfectly flat mirrors, the layout of the second mirror in the coupled optimization is such that its misalignments (mainly curvature) effectively compensate for the misalignments of the first mirror, resulting in a spotsize improvement of over 95 % to below the diffraction limit of the system.

The activity of the positional error constraint in the optimal solution of the uncoupled optimization (while the system easily remains within the accuracy limits) indicates the system is unnecessarily overconstrained. The SDO approach makes use of the enlarged feasible domain, which is apparent from the mass transfer between the mirrors in the optimal solution and the significant differences in topologies. Thus, the typical design approach unnecessarily overconstrains problems, whereas the SDO approach enlarges the feasible domain and gives the optimizer more freedom to minimize the objective while still satisfying all constraints.

During optimization the SFE constraints are not necessarily satisfied, which means that optical analysis is based on optical properties that do not accurately describe the deformed surface leading to inaccurate results. However, the converged optimal solutions do satisfy the SFE constraints and hence accurately describe the system's optical performance metrics. A more enhanced surface error determination method may result in faster convergence, and additionally a different optimal solution.

One would expect the SDO problem to be more difficult to solve than the uncoupled problem, due to a larger design space and potentially more complicated cost function. However, the results indicate the opposite as the required number of iterations to solve the problem remain the same. The iteration history, Fig. 7.7, shows that the SDO approach is able to drastically decrease the objective in the first number of iterations, where the uncoupled optimization requires more iterations. The RMS spot size diameter of the uncoupled system reaches the diffraction limit twice, halfway the iteration history, whereas the individual components are, at these particular points in the iteration history, far from optimal. In addition, these points are not feasible, since the components do not satisfy all constraints. In addition, when the optimizer is able to decrease the objective function of the second mirror, the system spot size increases again. This indicates that the mirrors exactly counteract each others error during optimization, although the optimizer is unaware of this information. Thus, component interaction should be included to obtain a more optimal solution in terms of system performance.

Thus, the case study proves that an integrated structural-thermal-optical design optimization procedure taking into account all system components improves the system optical performance compared to individual component optimization, while subjected to equivalent design constraints.

A potential limitation of the method in current use is that the imposed boundary conditions are assumed to be known. This implies that the housing is designed and analyzed before the conceptual design of the mirror, which is not necessarily the case. Additional research concerning simultaneous optimization of the housing and optical components is therefore of interest. An extension to this is the simultaneous optimization of the housing and optical components when their domains are merged into a single mesh, instead of using separate meshes per component as in the present study. A single, enlarged design domain would give the optimizer the freedom to relocate the boundary conditions.

The determination of mirror misalignments from the deformed configuration includes multiple assumptions influencing the final accuracy: these assumptions are the negligible radial displacements and constant curvature approximations, which limits the method to load cases causing deformations with relatively large out of plane versus in plane magnitudes, small changes in the radius of curvatures and small tip/tilt misalignments. For the targeted high-precision optical instruments these assumptions apply, but in other optical systems with larger deformations a more extended misalignment analysis is necessary. In addition, a more complex misalignment analysis would open up possibilities to extent to multiple, and different types of components, e.g. lenses, gratings, prisms and initially curved mirrors.

Additionally, the differences in optical path lengths currently only take into account despace effects, whereas tip/tilt, curvature, decenter and higher order terms also have small effects. These additional effects can influence the optical performance prediction. Hence, if incorporated, the influence should be

evaluated by a full STOP analysis using numerical ray tracing to verify the impact of the previously made assumptions.

Furthermore, the current ray tracing technique is limited by the paraxial approximation. In the studied two-mirror system, the maximum angle from the optical axis (in undeformed configuration) is smaller than 4°, thus the paraxial errors are smaller than 0.5 %. In order to limit the paraxial error to less then one percent, the current method is limited to maximum angles from the optical axis of about 14°. When larger angles are required, the extension to more advanced aberration theory or numerical ray tracing is required. This would also open up possibilities for non-constant curvature or non-symmetric (freeform) mirrors.

A recommendation that might further improve the performance of the mirror mounts is the extension to multi-material topology optimization to achieve higher performances as there are more possibilities to counter effects of thermal expansion, create conductive isolation, as well as damp out external vibrations [See: 48]. Also, optimizing locations and magnitudes of active thermal components (heaters/coolers) can have a large influence on both topology and the required design effort. In addition, enhancing thermal modeling and control by e.g. considering design-dependent heat loads affected by the misalignments and including radiation influences would increase the accuracy in relation to industrial usage.

In order to take this research from a concept version (proof-of-principle) to industrial usage the biggest step is to extent the method to 3D structures as well as taking manufacturability into account. One could use the same method for the detection of misalignments, i.e. fitting a parabolic plane through the displaced surfaces from which known constant sensitivities can be derived. Though, a simpler and more accurate approach would be to decompose the deformed surfaces into its Zernike polynomials (in the case of circular mirror sheets) or another set of orthogonal polynomials for other shapes. Either a sensitivity matrix, indicating the change in optical performance with respect to a change in magnitude of a Zernike mode, can be created, or one could perform paraxial ray tracing. Both are only accurate for small deformations. For larger deformations one is required to use a more complex numerical ray tracing technique. In order to make the 3D design manufacturable additional constraints (or filters) should be applied.

To conclude with a future perspective; it is expected that the more components compromise the system and the higher the sensitivity of the interactions, the greater the benefit of the SDO method will be. Allowing the optimizer to distribute unavoidable errors over multiple components in the system, instead of letting the designer impose the error budgets on each component, enlarges the feasible domain and the potential for superior system designs.

9. CONCLUSIONS

A new method to improve the optical performance of multicomponent optomechanical systems is presented. The method uses topology optimization and a full structural-thermal-optical analysis to simultaneously design the layout of multiple components for a system performance metric.

The aim of this thesis has been to investigate how to design optomechanical components such that the optical performance degradation due to thermal loads or mounting errors is minimized. Therefore, it was of interest to research the influence of including the optical performance metrics in the design and optimization of these systems. For multicomponent systems it is of interest what the differences are between optimizing a coupled system and optimizing the individual components. This study involved combining multiple methods of multiphysics analysis techniques and structural optimization, which led to an effective new design optimization procedure.

An optomechanical component can be optimized for mounting error or thermal load insensitivity by using topology optimization minimizing a surface form error or some displacement based function with relation to the undeformed configuration. Instead of optimizing a design based on deformations one can optimize a component based on an optical performance metric by including a structural-thermal-performance analysis in the topology optimization framework. Such an analysis is able to expose the performance metrics that matter for optomechanical systems without relying on intermediate derived performance indicators. For a single component system or multicomponent uncoupled optimized system, only minimizing deformations leads to better optical systems. For a multicomponent system, the coupled analysis allows the optical components to compensate for each others errors, which is a mechanism that is invisible to the optimizer in an uncoupled optimization. That allows for focus where it matters, without overconstraining the system unnecessarily. Since the feasible design space of the system level optimization completely encapsulates the design space of the individual component optimization, the globally optimal performance of the coupled system is always better or equal to the uncoupled optimization approach.

The benefits of this method is investigated by simultaneous topology optimization of multiple mirror mounts to exploit the interaction of aberrations between different components due to thermal loads and frame movements and minimize a system optical performance while constrained by dynamic stiffness, weight and optical performance measures, both on a component and system level. The results of the optimization problems showed that the coupled optimization based on the full structural-thermal-optical performance analysis is able to reduce the spot size of a two-mirror system with 95 % compared to uncoupled component optimization to below the system's diffraction limit.

This work contributes to the research fields of optomechanical design and topology optimization. The problem formulation questions the typical optomechanical design approach and combines multidisci-

plinary, multicomponent, system, and topology optimization to show both the system engineering and optimization communities that system optimization involving multiple optomechanical components leads to more design freedom and potentially improved systems for specific applications. These findings are of interest to system engineers and optomechanical designers of high-tech systems that are looking to further improve their instruments' optical performance, or maintain the optical performance under more stringent environments.

As a result of this study, further research might well be conducted on the extension to multiple and different optical components. It is expected that the more components compromise the system and the higher the sensitivity of the interactions, the greater the benefit of the system design optimization method will be. In order to use this method in industrial usage an essential step is to extent the method to 3D structures as well as taking manufacturability into account. The current method is limited by the paraxial approximation and hence small displacements. When larger angles are required, the extension to more advanced aberration theory or numerical ray tracing is required. Despite fact that real systems are more complex than the simplified example considered in this study, it shows optomechanical designers should aim for considering and integrating multiple components and physics simultaneously in the design loop when requirements seem irreconcilable.

LIST OF REFERENCES

[1] D. Chin, "Optical mirror-mount design and philosophy," *Applied Optics*, vol. 3, no. 7, pp. 895–901, 1964.

[2] R. S. Reiss, "Opto-mechanical instrument design," in *Proceedings of SPIE*, vol. 0817, pp. 154–170, 1987.

[3] P. R. Yoder and D. Vukobratovich, *Opto-Mechanical Systems Design*. CRC Press, 4th ed., 2015.

[4] P. Giesen and E. Folgering, "Design guidelines for thermal stability in opto-mechanical instruments," *Proceedings of SPIE*, vol. 5176, pp. 126–134, 2003.

[5] J. Pijnenburg, M. J. A. te Voert, J. de Vreugd, A. Vosteen, W. van Werkhoven, J. Mekking, and B. A. H. Nijland, "Ultra-stable isostatic bonded optical mount design for harsh environments," in *Proceedings of SPIE*, no. 8450, p. 12, 2012.

[6] E. A. Meijer, J. N. Nijenhuis, R. J. P. Vink, F. Kamphues, W. Gielesen, and C. Coatantiec, "Picometer metrology for the GAIA mission," in *Proceedings of SPIE*, vol. 7439, p. 15, 2008.

[7] W. Gielesen, D. de Bruijn, T. Van den Dool, F. Kamphues, J. Mekking, B. Calvel, A. Laborie, C. Coatantiec, S. Touzeau, M. Erdmann, P. Gare, and D. Monteiro, "GAIA basic angle monitoring system," in *Proceedings of SPIE* (M. C. Clampin, G. G. Fazio, H. A. MacEwen, and J. M. Oschmann, eds.), vol. 8442, p. 88630G, International Society for Optics and Photonics, aug 2013.

[8] J. Nijenhuis and R. Hamelinck, "The optimization of the opto-mechanical performance of the mirror segments for the E-ELT," in *Proceedings of SPIE* (T. Andersen and A. Enmark, eds.), vol. 8336, p. 83360H, International Society for Optics and Photonics, sep 2011.

[9] J. Nijenhuis, B. Braam, and R. Hamelinck, "The opto-mechanical performance prediction of thin mirror segments for E-ELT," in *Proceedings of SPIE* (R. Navarro, C. R. Cunningham, and E. Prieto, eds.), vol. 8450, p. 1001203, International Society for Optics and Photonics, sep 2016.

[10] B. M. Welsh, "Imaging performance analysis of adaptive optical telescopes using laser guide stars," *Applied Optics*, vol. 30, p. 5021, dec 1991.

[11] K. B. Doyle, V. L. Genberg, and G. J. Michels, *Integrated Optomechanical Analysis*. SPIE Press, 2nd ed., 2012.

[12] G. H. Spencer and M. V. R. K. Murty, "General ray-tracing procedure," *Journal of the Optical Society of America*, vol. 52, pp. 672–678, jun 1962.

[13] V. L. Genberg, "Optical Surface Evaluation," in *Proceedings of SPIE* (L. M. Cohen, ed.), vol. 0450, pp. 81–87, International Society for Optics and Photonics, jan 1984.

[14] V. L. Genberg, "Optical performance criteria in optimum structural design," in *Proceedings of SPIE* (E. A. Derby, C. G. Gordon, D. Vukobratovich, P. R. Yoder, and C. H. Zweben, eds.), vol. 3786, pp. 248–255, International Society for Optics and Photonics, sep 1999.

[15] M. P. Bendsøe and O. Sigmund, *Topology Optimization: Theory, Methods and Applications*. No. 724, Springer Berlin Heidelberg, 2nd ed., 2003.

[16] J. D. Johnston, J. M. Howard, G. E. Mosier, K. A. Parrish, M. A. McGinnis, A. M. Bluth, K. Kim, and K. Q. Ha, "Integrated modeling activities for the James Webb Space Telescope: structural-thermal-optical analysis," in *Proceedings of SPIE* (J. C. Mather, ed.), vol. 5487, p. 600, International Society for Optics and Photonics, oct 2004.

[17] A. Kuisl, W. Gambietz, J. Zeller, A. Zhukov, G. Bleicher, and M. Czupalla, "A multidisciplinary software for structural, thermal and optical performance analysis of space optical instruments," in *European Conference on Spacecraft Structures Materials and Environmental Testing*, (Toulouse), p. 8, OHB System AF, 2016.

[18] A. L. Williams, V. L. Genberg, S. M. Gracewski, and B. D. Stone, "Simultaneous design optimization of optomechanical systems," in *Proceedings of SPIE* (E. A. Derby, C. G. Gordon, D. Vukobratovich, P. R. Yoder, Jr., and C. H. Zweben, eds.), vol. 3786, pp. 236–247, International Society for Optics and Photonics, sep 1999.

[19] G. J. Michels, V. L. Genberg, K. B. Doyle, and G. R. Bisson, "Design optimization of system level adaptive optical performance," in *Proceedings of SPIE* (M. A. Kahan, ed.), vol. 5867, pp. 58670P–58670P–8, International Society for Optics and Photonics, aug 2005.

[20] D. Bonin and B. McMaster, "Closed loop optimization of opto-mechanical structure via mechanical and optical analysis software," in *Proceedings of SPIE* (M. D. Turner and G. W. Kamerman, eds.), vol. 6550, p. 65500X, International Society for Optics and Photonics, apr 2007.

[21] M. Nazarathy, A. Hardy, and J. Shamir, "Misaligned first-order optics: canonical operator theory," *Journal of the Optical Society of America*, vol. 3, no. 9, pp. 1360–1369, 1986.

[22] W. J. Smith, *Modern Optical Engineering*. SPIE Press, 4th ed., 2007.

[23] R. E. Fischer, B. Tadic-Galeb, and P. R. Yoder, *Optical System Design*. SPIE Press, 2nd ed., 2008.

[24] A. J. G. Schoofs, "Structural Optimization History and State-of-the-Art," *Topics in Applied Mechanics*, no. November 1992, pp. 339–345, 1993.

[25] K. Svanberg, "The method of moving asymptotes - a new method for structural optimization," *International Journal for Numerical Methods in Engineering*, vol. 24, pp. 359–373, feb 1987.

[26] P. Y. Papalambros and D. J. Wilde, *Principles of Optimal Design: Modeling and Computation*. Cambridge: Cambridge University Press, 2nd ed., 2000.

[27] M. P. Bendsøe and N. Kikuchi, "Generating optimal topologies in structural design using a homogenization method," *Computer Methods in Applied Mechanics and Engineering*, vol. 71, no. 2, pp. 197–224, 1988.

[28] M. P. Bendsøe, "Optimal shape design as a material distribution problem," *Structural Optimization*, vol. 1, no. 4, pp. 193–202, 1989.

[29] M. Y. Wang, X. Wang, and D. Guo, "A level set method for structural topology optimization," *Computer Methods in Applied Mechanics and Engineering*, vol. 192, no. 1-2, pp. 227–246, 2003.

[30] G. Allaire, F. Jouve, and A.-M. Toader, "A level-set method for shape optimization," *Comptes Rendus Mathematique*, vol. 334, no. 12, pp. 1125–1130, 2002.

[31] G. Allaire, F. Jouve, and A. M. Toader, "Structural optimization using sensitivity analysis and a level-set method," *Journal of Computational Physics*, vol. 194, no. 1, pp. 363–393, 2004.

[32] E. Andreassen, A. Clausen, M. Schevenels, B. S. Lazarov, and O. Sigmund, "Efficient topology optimization in MATLAB using 88 lines of code," *Structural and Multidisciplinary Optimization*, vol. 43, no. 1, pp. 1–16, 2011.

[33] H. Rodrigues and P. Fernandes, "A material based model for topology optimization of thermoelastic structures," *International Journal for Numerical Methods in Engineering*, vol. 38, no. 12, pp. 1951–1965, 1995.

[34] Q. Li, G. P. Steven, and Y. M. Xie, "Thermoelastic Topology Optimization for Problems With Varying Temperature Fields," *Journal of Thermal Stresses*, vol. 24, no. 4, pp. 347–366, 2001.

[35] T. Gao and W. Zhang, "Topology optimization involving thermo-elastic stress loads," *Structural and Multidisciplinary Optimization*, vol. 42, no. 5, pp. 725–738, 2010.

[36] J. D. Deaton and R. V. Grandhi, "Stiffening of restrained thermal structures via topology optimization," *Structural and Multidisciplinary Optimization*, vol. 48, no. 4, pp. 731–745, 2013.

[37] O. Sigmund, "Design of multiphysics actuators using topology optimization - Part I: One-material structures," *Computer Methods in Applied Mechanics and Engineering*, vol. 190, no. 49-50, pp. 6605–6627, 2001.

[38] R. Ansola, E. Veguería, J. Canales, and C. Alonso, "Evolutionary optimization of compliant mechanisms subjected to non-uniform thermal effects," *Finite Elements in Analysis and Design*, vol. 57, pp. 1–14, 2012.

[39] Z. D. Ma, N. Kikuchi, and H. C. Cheng, "Topological design for vibrating structures," *Computer Methods in Applied Mechanics and Engineering*, vol. 121, no. 1-4, pp. 259–280, 1995.

[40] N. L. Pedersen, "Maximization of eigenvalues using topology optimization," *Structural and Multidisciplinary Optimization*, vol. 20, no. 1, pp. 2–11, 2000.

[41] J. Du and N. Olhoff, "Topological design of freely vibrating continuum structures for maximum values of simple and multiple eigenfrequencies and frequency gaps," *Structural and Multidisciplinary Optimization*, vol. 34, no. 2, pp. 91–110, 2007.

[42] T. D. Tsai and C. C. Cheng, "Structural design for desired eigenfrequencies and mode shapes using topology optimization," *Structural and Multidisciplinary Optimization*, vol. 47, no. 5, pp. 673–686, 2013.

[43] K.-S. Park, J. H. Lee, and S.-K. Youn, "Lightweight mirror design method using topology optimization," *Optical Engineering*, vol. 44, p. 53002, may 2005.

[44] R. Sahu, V. Patel, S. K. Singh, and B. S. Munjal, "Structural optimization of a space mirror to selectively constrain optical aberrations," *Structural and Multidisciplinary Optimization*, vol. 55, pp. 2353–2363, jun 2017.

[45] J.-Y. Kim, K.-S. Park, and S.-K. Youn, "The design of reflective mirrors for high-power laser systems using topology optimization," in *6th World Congress on Structural and Multidisciplinary Optimization*, 2005.

[46] R. Hu, S. Liu, and Q. Li, "Topology-optimization-based design method of flexures for mounting the primary mirror of a large-aperture space telescope," *Applied Optics*, vol. 56, no. 15, p. 4551, 2017.

[47] R. Hu, W. Chen, D. Ph, Q. Li, S. Liu, and P. Zhou, "Design optimization method for additive manufacturing of the primary mirror of a large-aperture space telescope," *Journal of Aerospace Engineering*, vol. 30, no. 3, pp. 1–10, 2017.

[48] M. Van der Kolk, G. J. Van der Veen, J. de Vreugd, and M. Langelaar, "Multi-material topology optimization of viscoelastically damped structures using a parametric level set method," *Journal of Vibration and Control*, vol. 23, no. 15, pp. 2430–2443, 2017.

[49] J. Zhu, W. Zhang, and P. Beckers, "Integrated layout design of multi-component system," *International Journal for Numerical Methods in Engineering*, vol. 78, pp. 631–651, may 2009.

[50] H. Chickermane and H. C. Gea, "Design of multi-component structural systems for optimal layout topology and joint locations," *Engineering with Computers*, vol. 13, no. 4, pp. 235–243, 1997.

[51] M. Jin and X. Zhang, "A new topology optimization method for planar compliant parallel mechanisms," *Mechanism and Machine Theory*, vol. 95, pp. 42–58, 2016.

[52] M. P. Bendsøe and O. Sigmund, "Material interpolation schemes in topology optimization," *Archive of Applied Mechanics*, vol. 69, no. 9-10, pp. 635–654, 1999.

[53] R. Cook, *Concepts and Applications of Finite Element Analysis*. John Wiley & Sons, Ltd, 4th ed., 1981.

[54] D. C. Lay, *Linear Algebra and Its Applications*. Pearson International, 3rd ed., 2006.

[55] J. Yuan, X. Long, and M. Chen, "Generalized ray matrix for spherical mirror reflection and its application in square ring resonators and monolithic triaxial ring resonators," *Optics Express*, vol. 19, no. 7, pp. 6762–6776, 2011.

[56] T. E. Bruns and D. A. Tortorelli, "Topology optimization of non-linear elastic structures and compliant mechanisms," *Computer Methods in Applied Mechanics and Engineering*, vol. 190, no. 26-27, pp. 3443–3459, 2001.

[57] J. K. Guest, J. H. Prévost, and T. Belytschko, "Achieving minimum length scale in topology optimization using nodal design variables and projection functions," *International Journal for Numerical Methods in Engineering*, vol. 61, pp. 238–254, sep 2004.

[58] O. Sigmund, "Morphology-based black and white filters for topology optimization," *Structural and Multidisciplinary Optimization*, vol. 33, no. 4-5, pp. 401–424, 2007.

[59] S. Xu, Y. Cai, and G. Cheng, "Volume preserving nonlinear density filter based on heaviside functions," *Structural and Multidisciplinary Optimization*, vol. 41, no. 4, pp. 495–505, 2010.

A. STRUCTURAL COMPONENT MATERIALS AND FIGURES OF MERIT

This appendix gives detailed properties of commonly used structural component and mirror mount materials for optomechanical design. Often used materials and their properties are shown in Fig. A.1 and for some selected materials the material selection figures of merit are shown in Fig. A.2.

Properties of Selected Mirror and Structural Materials

Preferred	ρ Density (g/cm^3)	E Young's Modulus (GPa) Large	ν Poisson's Ratio Small	K_{Ic} Fracture Toughness ($MPa[m]^{1/2}$) Large	MYS Microyield Strength (MPa) Large	α Thermal Expansion ($10^{-6}/K$) Small	k Thermal Conductivity (W/m K) Large	Cp Specific Heat (W sec/kg K)	D Thermal Diffusivity (10^{-6} m^2/sec) Large
Pyrex 7740	2.23	63	0.2			3.3	1.13	1050	0.65
Fused silica	2.19	72	0.17	<1.0	—	0.5	1.4	750	0.85
ULE fused silica	2.21	67	0.17			0.03	1.31	766	0.78
Zerodur	2.53	91	0.24			0.05	1.64	821	0.77
Aluminum: 6061	2.70	68	0.33	—	140.	22.5	167.	896	69.
MMC: 30% SiC/Al	2.91	117	0.29	>10.	>200.	12.4	123.	870	57.
Beryllium: I-70-H	1.85	287	0.043	12.	35.	11.3	216.	1925	57.2
Beryllium: I-220-H	1.85	287	0.043	12.	50.	11.3	216.	1925	57.2
Copper: OFC	8.94	117	0.343	—	12.	16.5	391.	385	115.5
Invar 36	8.05	141	0.259	—	41.	1.0	10.4	515	2.6
Super Invar	8.13	148	0.26	—	41.	0.3	10.5	515	2.5
Molybdenum	10.21	324	0.293	—	280.	5.0	140.	247	55.5
Silicon	2.33	131	0.42	1.0	—	2.6	156.	710	94.3
SiC: HP alpha	3.2	455	0.14	5.2	—	2.4	155.	650	74.5
SiC: CVD beta	3.21	465	0.21	2.7	—	2.4	198.	733	84.2
SiC: RB-30% Si	2.89	330	0.24	2.5	—	2.5	155.	670	80.0
Stainless steel: 304	8.00	193	0.27	—	65.	14.7	16.2	500	4.1
Stainless steel: 416	7.80	215	0.283	—	—	8.5	24.9	460	6.9
Titanium: 6Al4V	4.43	114	0.31	—	50.	8.8	7.3	560	2.9
Gr/Ep (GY-70/×30)	1.78	93	—			0.02	35.0		

Figure A.1.: Properties of most common mirror and structural materials including density, Young's modulus, Poisson's ratio, fracture toughness, microyield strength, thermal expansion and conductivity, specific heat and thermal diffusivity. The row indicating 'preferred' gives insight in what properties are preferably large or small for typical optomechanical designs. Unknown values are indicated by a dash. Additional information about the chart and materials for e.g. lenses can be found in [3].

Figures of Merit for Selected Mirror and Structural Materials

	Weight and Self-Weight Deflection Proportionality Factors				Thermal Distortion Coefficients	
	$(E/\rho)^{1/2}$ Resonant Frequency for Same Geometry (arb. units)	ρ/E Mass or Deflection for Same Geometry (arb. units)	ρ^3/E Deflection for Same Mass (arb. units)	$(\rho^3/E)^{1/2}$ Mass for Same Deflection (arb. units)	α/k Steady State (μm/W)	α/D Transient (sec/m^2 K)
Preferred	Large	Small	Small	Small	Small	Small
Pyrex	5.3	3.53	1.76	0.420	2.92	5.08
Fused silica	5.7	3.04	1.46	0.382	0.36	0.59
ULE fused silica	5.5	3.30	1.61	0.401	0.02	0.04
Zerodur	6.0	2.78	1.78	0.422	0.03	0.07
Aluminum: 6061	5.0	3.97	2.90	0.538	0.13	0.33
MMC: 30% SiC/Al	6.3	2.49	2.11	0.459	0.10	0.22
Beryllium: I-70-H	12.5	0.64	0.22	0.149	0.05	0.20
Beryllium: I-220-H	12.5	0.64	0.22	0.149	0.05	0.20
Copper: OFC	3.6	7.64	61.1	2.471	0.53	0.14
Invar 36	4.2	5.71	37.0	1.924	0.10	0.38
Super Invar	4.3	5.49	36.3	1.906	0.03	0.12
Molybdenum	5.6	3.15	32.8	1.812	0.04	0.09
Silicon	7.5	1.78	0.97	0.311	0.02	0.03
SiC: HP alpha	11.9	0.70	0.72	0.268	0.02	0.03
SiC: CVD	12.0	0.69	0.71	0.267	0.02	0.03
SiC: RB-30% Si	10.7	0.88	0.73	0.270	0.01	0.03
Stainless steel: 304	4.9	4.15	26.5	1.629	0.91	3.68
Stainless steel: 416	5.2	3.63	22.1	1.486	0.34	1.23
Titanium: 6Al4V	5.1	3.89	7.63	0.873	1.21	3.03

Figure A.2.: Figures of merit for selected mirror and structural materials, often used to aid in material selection. The selection criteria include weight and self-weight deflection factors using the density ρ and Young's modulus E, as well as thermal distortion coefficients based on the CTE α, thermal conductivity k and thermal diffusivity D. Note the row indicating 'preferred', which gives insight in what coefficient are preferably large or small for typical optomechanical designs. That is high resonant frequency, low mass, small deflections due to selfweight and small expansion coefficient in relation to both thermal conductivity and diffusivity. Additional information about the chart and materials for e.g. lenses can be found in [3].

B. FINITE ELEMENT ANALYSIS

The following material provides detailed information about the finite element analysis procedure used. Most information in this section is derived from multiple chapters in Cook [See: 53].

B.1 Preliminaries

For linear elastic conditions, stress-strain relations can be stated in general as

$$\begin{aligned} \boldsymbol{\sigma} &= \mathbf{E}\boldsymbol{\varepsilon} + \boldsymbol{\sigma}_0 \\ &= \mathbf{E}(\boldsymbol{\varepsilon} - \boldsymbol{\varepsilon}_0) \end{aligned} \tag{B.1}$$

where $\boldsymbol{\sigma}_0$ and $\boldsymbol{\varepsilon}_0$ respectively indicate the initial stress and strain and the constitutive matrix $\mathbf{E}$ contains elastic constants. For a 2D case where x and y are the in-plane coordinates, this can be written in matrix form as

$$\begin{bmatrix} \sigma_x \\ \sigma_y \\ \tau_{xy} \end{bmatrix} = \begin{bmatrix} E_{11} & E_{12} & E_{13} \\ E_{21} & E_{22} & E_{23} \\ E_{31} & E_{32} & E_{33} \end{bmatrix} \begin{bmatrix} \varepsilon_x \\ \varepsilon_y \\ \gamma_{xy} \end{bmatrix} + \begin{bmatrix} \sigma_{x0} \\ \sigma_{y0} \\ \tau_{xy0} \end{bmatrix} \tag{B.2}$$

The constitutive matrix $\mathbf{E}$ is symmetric and can represent both isotropic and anisotropic material properties. For an isotropic plane stress case the constitutive matrix is defined as

$$\mathbf{E} = \frac{E}{1-\nu^2} \begin{bmatrix} 1 & \nu & 0 \\ \nu & 1 & 0 \\ 0 & 0 & \frac{1-\nu}{2} \end{bmatrix} \tag{B.3}$$

where ν is the Poisson's ratio. Inverting Eq. (B.3) one obtains the relation

$$\boldsymbol{\varepsilon} = \mathbf{E}^{-1}\boldsymbol{\sigma} + \boldsymbol{\varepsilon}_0 \tag{B.4}$$

If the material is isotropic and initial strains are produced by a temperature change T, then $\varepsilon_{x0} = \varepsilon_{y0} = \alpha T$, where α is the CTE (here assumed to be independent of temperature).

A displacement field describes how a body deforms as well as how it displaces. Strain-displacement relations extract the strain field contained in a displacement field and play a prominent role in formulating commonly used elements. The linear strain-displacement relations are

$$\begin{aligned} \varepsilon_x &= \frac{\partial u}{\partial v} \\ \varepsilon_y &= \frac{\partial v}{\partial y} \\ \gamma_{xy} &= \frac{\partial u}{\partial y} + \frac{\partial v}{\partial x} \end{aligned} \tag{B.5}$$

where $u = u(x,y)$ and $v = v(x,y)$ respectively are the x-direction and y-direction displacements.

In matrix operator format, for a 2D case, the strain-displacement relations are

$$\begin{bmatrix} \varepsilon_x \\ \varepsilon_y \\ \gamma_{xy} \end{bmatrix} = \begin{bmatrix} \frac{\partial}{\partial x} & 0 & \frac{\partial}{\partial y} \\ 0 & \frac{\partial}{\partial y} & \frac{\partial}{\partial x} \end{bmatrix}^T \begin{bmatrix} u \\ v \end{bmatrix} \tag{B.6}$$

which can compactly be written as

$$\varepsilon = \partial \mathbf{u} \tag{B.7}$$

The compatibility condition ($\varepsilon_{x,yy} + \varepsilon_{y,xx} = \gamma_{xy,xy}$) requires that displacements are continuous and single-valued functions of position, i.e. when a body is deformed without breaking, no cracks appear in stretching, no kinks appear in bending and material particles do no interpenetrate.

The equilibrium equation scan be symbolised as

$$\partial^T \boldsymbol{\sigma} + \mathbf{F} = \mathbf{0} \tag{B.8}$$

The foregoing formula of structural mechanics are very comparable to quantities and fields in the thermal domain. Note that heat conduction is a scalar problem, since the field quantity temperature T has no direction, while the displacement field is a vector field having components in coordinate directions. The field gradient in the structural domain, the strains, are comparable to temperature gradients in the thermal domain. The elastic constants $\mathbf{E}$ is comparable to the thermal conductivities $\boldsymbol{\kappa}$ similar as stresses $\boldsymbol{\sigma}$ and heat fluxes $\mathbf{q}$. Surface loads, in structural mechanics denoted by tractions $\mathbf{t}$ are comparable to normal heat fluxes q_n. The internal loads, in structural mechanics the body forces $\mathbf{F}$ have a thermal counterpart which is the internal heat generation $\mathbf{Q}$.

B.2 Interpolation and shape functions

Interpolations devise a continuous function satisfying prescribed conditions at a finite number of points. In finite element analysis these points are the nodes of an element, where the prescribed conditions are the nodal values (and possibly its derivatives).

In terms of generalised DOF a_i, an interpolating polynomial with dependent variable ϕ and independent variable x can be written as

$$\phi = \sum_{i=0}^{n} d_i x^i = \mathbf{Xd} \tag{B.9}$$

where $\mathbf{X} = \begin{pmatrix} 1 & x & x^2 & \dots & x^n \end{pmatrix}$ and $\mathbf{d} = (d_0 \quad d_1 \quad d_2 \quad \dots \quad d_n)^T$. The a_i can be expressed in terms of nodal values of ϕ, appearing at known values of x, this relation is symbolised as

$$\boldsymbol{\phi}^{\mathrm{e}} = \mathbf{Ad} \tag{B.10}$$

where each row of $\mathbf{A}$ is $\mathbf{X}$ evaluated at the appropriate nodal location. As a result

$$\phi = \mathbf{N}\boldsymbol{\phi}^{\mathrm{e}} \tag{B.11}$$

where $\mathbf{N} = \mathbf{XA}^{-1} = \begin{bmatrix} N_1 & N_2 & \dots \end{bmatrix}$. Every individual N_i is called a shape function and state the interpolated $\phi = \phi(x)$ when the corresponding ϕ_i is unity and all other ϕ_i are zero. The element nodal values $\boldsymbol{\phi}^{\mathrm{e}}$ appear in $\mathbf{U}$ (or $\mathbf{T}$ for a thermal case), the global vector of DOF, hence $\boldsymbol{\phi}^{\mathrm{e}}$ is determined by solving $\mathbf{KU} = \mathbf{F}$.

While ϕ can be guaranteed to vary smoothly within each element, the transition between elements is not necessarily smooth; the symbol C^m describes the continuity of a piecewise field. A certain field is C^m continuous if its derivatives up to and including degree m are inter-element-continuous. Usually, C^0 elements are used to model plane and solid bodies and C^1 elements are used to model beams, plates and shells providing inter-elemental continuity of the slope.

Consider C^0 interpolation between points (x_1, ϕ_1) and (x_2, ϕ_2) for which $\mathbf{X} = \begin{bmatrix} 1 & x \end{bmatrix}$. Evaluating $\mathbf{X}$ at both points, one can obtain

$$\begin{bmatrix} \phi_1 \\ \phi_2 \end{bmatrix} = \mathbf{A} \begin{bmatrix} d_0 \\ d_1 \end{bmatrix} \tag{B.12}$$

where

$$\mathbf{A} = \begin{bmatrix} 1 & x_1 \\ 1 & x_2 \end{bmatrix} \tag{B.13}$$

Thus we can calculate the shape functions

$$\mathbf{N} = \begin{bmatrix} \frac{x_2 - x}{x_2 - x_1} & \frac{x - x_1}{x_2 - x_1} \end{bmatrix} \tag{B.14}$$

Note that all shape functions N_i along with the function ϕ are polynomials of the same degree, that for any shape function N_i, $N_i = 1$ when $x = x_i$ and $N_i = 0$ when $x = x_j$ for any integer $j \neq i$, i.e. N_i is unity at its own node but is zero at other nodes. Furthermore, C^0 shape functions sum to unity; $\sum N_i = 1$. In two or three dimensions, two or three independent variables are needed and usually all components are interpolated using the same shape functions.

B.3 Principle of virtual work

The principle of virtual work can be used to obtain formulas for the element stiffness matrix and for the accompanying load vectors associated with initial strains, body forces and surface tractions[1].

A virtual displacement is an imaginary, admissible[2] and very small change in the configuration of a system relative to the equilibrium configuration. The principle of virtual work for a single element can be stated as

$$\begin{aligned} \int \delta W^{\text{int}} \mathrm{d}V &= \int \delta W^{\text{ext}} \mathrm{d}V \\ \int \delta \varepsilon^T \boldsymbol{\sigma} \mathrm{d}V &= \int \delta \mathbf{U}^T \mathbf{F} \mathrm{d}V + \int \delta \mathbf{U}^T \mathbf{t} \mathrm{d}S \end{aligned} \tag{B.15}$$

where $\delta \mathbf{U} = \begin{bmatrix} \delta u & \delta v & \delta w \end{bmatrix}^T$ for a generalised 3D case. Equation (B.15) tells us that for any admissible virtual displacement $\delta \mathbf{U}$ from an equilibrium configuration the increment of stored strain energy is equal to the increment of work done by body forces $\mathbf{F}$ and surface tractions $\mathbf{t}$.

Now let $\mathbf{U}$ be interpolated over an element in the same way as ϕ in Eq. (B.11)

$$\mathbf{U} = \mathbf{N}\mathbf{d} \tag{B.16}$$

where in this case $\mathbf{d}$ lists the nodal displacement DOF of an element. The strains are determined from the displacements as follows

$$\varepsilon = \boldsymbol{\partial} \mathbf{N}\mathbf{d} = \mathbf{B}\mathbf{d} \tag{B.17}$$

where $\mathbf{B}$ is called the strain-displacement matrix. Assuming Eq. (B.34) includes the initial strain (e.g. from temperature variations), by substitution of Eq. (B.34) into Eq. (B.15) one obtains

$$\delta \mathbf{d}^T \left(\int \mathbf{B}^T \mathbf{E} \mathbf{B} \mathrm{d}V \mathbf{d} - \int \mathbf{B}^T \mathbf{E} \varepsilon_0 \mathrm{d}V + \int \mathbf{B}^T \boldsymbol{\sigma}_0 \mathrm{d}V - \int \mathbf{N}^T \mathbf{F} \mathrm{d}V - \int \mathbf{N}^T \mathbf{t} \mathrm{d}S \right) = 0 \tag{B.18}$$

Equation (B.18) must be true for any admissible virtual displacements from the equilibrium configuration and therefore Eq. (B.18) yields

$$\mathbf{K}^{\text{e}} \mathbf{U}^{\text{e}} = \mathbf{F}^{\text{e}} \tag{B.19}$$

[1] This can be done equivalently for the thermal case; the conductivity matrix and the heat fluxes, normal fluxes and internal heat generation.

[2] An admissible displacement does not violate compatibility or displacement boundary conditions.

where

$$\mathbf{K}^{\mathrm{e}} = \int \mathbf{B}^T \mathbf{E} \mathbf{B} \mathrm{d}V \tag{B.20}$$

and the vector of loads applied to the element nodes, due to all sources but element deformation, is

$$\mathbf{F}^{\mathrm{e}} = \int \mathbf{N}^T \mathbf{F} \mathrm{d}V + \int \mathbf{N}^T \mathbf{t} \mathrm{d}S + \int \mathbf{B}^T \mathbf{E} \boldsymbol{\varepsilon}_0 \mathrm{d}V - \int \mathbf{B}^T \boldsymbol{\sigma}_0 \mathrm{d}V \tag{B.21}$$

The work W done by nodal loads $\mathbf{P}$ in moving through nodal displacements $\mathbf{d}$ is equal to work done by distributed elemental loads $\mathbf{F}$ and $\mathbf{t}$ in moving through the displacement field defined by $\mathbf{d}$ and element shape functions, thus we can state

$$W = \mathbf{d}^T \mathbf{P} = \int \mathbf{U}^T \mathbf{F} \mathrm{d}V + \int \mathbf{U}^T \mathbf{t} \mathrm{d}S \tag{B.22}$$

B.4 Isoparametric elements

The isoparametric formulation permits quadrilaterals to have non-rectangular shapes. Shape functions are used to interpolate both the displacement field (or equivalently the temperature field) and element geometry. That is, displacement of a point within an element can be expressed in terms of nodal DOF and shape functions $\mathbf{N}$, which are functions of the reference coordinates. Similarly, the global position of a point within the element can be expressed in terms of global nodal positions and shape functions $\tilde{\mathbf{N}}$, which are also function of reference coordinates. The shape function matrices $\mathbf{N}$ and $\tilde{\mathbf{N}}$ are functions of the natural or intrinsic coordinates ξ, η and ζ and an element is considered isoparametric if $\mathbf{N}$ and $\tilde{\mathbf{N}}$ are identical.

Bilinear quadrilateral element

Because the Q4 element is isoparametric the same shape functions are sued to interpolate both coordinates and displacement of a point within the element from coordinates and displacements (or temperatures) of nodes, thus

$$\begin{aligned} \begin{bmatrix} x \\ y \end{bmatrix} &= \begin{bmatrix} \sum N_i x_i \\ \sum N_i y_i \end{bmatrix} &&= \mathbf{Nc} \\ \begin{bmatrix} u \\ v \end{bmatrix} &= \begin{bmatrix} \sum N_i u_i \\ \sum N_i v_i \end{bmatrix} &&= \mathbf{Nd} \end{aligned} \tag{B.23}$$

where for the Q4 i runs from one to four, and

$$\mathbf{c} = \begin{bmatrix} x_1 & y_1 & x_2 & y_2 & x_3 & y_3 & x_4 & y_4 \end{bmatrix}^T \tag{B.24}$$

$$\mathbf{d} = \begin{bmatrix} u_1 & v_1 & u_2 & v_2 & u_3 & v_3 & u_4 & v_4 \end{bmatrix}^T \tag{B.25}$$

$$\mathbf{N} = \begin{bmatrix} N_1 & 0 & N_2 & 0 & N_3 & 0 & N_4 & 0 \\ 0 & N_1 & 0 & N_2 & 0 & N_3 & 0 & N_4 \end{bmatrix} \tag{B.26}$$

The individual shape functions, by setting $a = 1$, $b = 1$, $x = \xi$ and $y = \eta$, are

$$\begin{aligned} N_1 &= \frac{(1-\xi)(1-\eta)}{4} \\ N_2 &= \frac{(1+\xi)(1-\eta)}{4} \\ N_3 &= \frac{(1+\xi)(1+\eta)}{4} \\ N_4 &= \frac{(1-\xi)(1+\eta)}{4} \end{aligned} \tag{B.27}$$

The strain-displacement matrix $\mathbf{B}$ cannot be written as easily since it involves gradients. Consider the function $\phi = \phi(\xi, \eta)$; its derivatives with respect to ξ and η are

$$\begin{aligned} \frac{\partial \phi}{\partial \xi} &= \frac{\partial \phi}{\partial x}\frac{\partial x}{\partial \xi} + \frac{\partial \phi}{\partial y}\frac{\partial y}{\partial \xi} \\ \frac{\partial \phi}{\partial \eta} &= \frac{\partial \phi}{\partial x}\frac{\partial x}{\partial \eta} + \frac{\partial \phi}{\partial y}\frac{\partial y}{\partial \eta} \end{aligned} \tag{B.28}$$

or equivalently

$$\begin{bmatrix} \phi_{,\xi} \\ \phi_{,\eta} \end{bmatrix} = \mathbf{J} \begin{bmatrix} \phi_{,x} \\ \phi_{,y} \end{bmatrix} \tag{B.29}$$

where $\mathbf{J}$ is the Jacobian matrix

$$\mathbf{J} = \begin{bmatrix} x_{,\xi} & y_{,\xi} \\ x_{,\eta} & y_{,\eta} \end{bmatrix} = \begin{bmatrix} \sum N_{i,\xi} x_i & \sum N_{i,\xi} y_i \\ \sum N_{i,\eta} x_i & \sum N_{i,\eta} y_i \end{bmatrix} \tag{B.30}$$

For a four-node plane element

$$\mathbf{J} = \frac{1}{4} \begin{bmatrix} -(1-\eta) & (1-\eta) & (1+\eta) & -(1+\eta) \\ -(1-\xi) & (1-\xi) & (1+\xi) & -(1+\xi) \end{bmatrix} \begin{bmatrix} x_1 & y_1 \\ x_2 & y_2 \\ x_3 & y_3 \\ x_4 & y_4 \end{bmatrix} = \begin{bmatrix} J_{11} & J_{12} \\ J_{21} & J_{22} \end{bmatrix} \tag{B.31}$$

This result can be used to derive the desired derivatives of the function with relation to the coordinates x and y, such that

$$\begin{bmatrix} \phi_{,x} \\ \phi_{,y} \end{bmatrix} = \mathbf{\Gamma} \begin{bmatrix} \phi_{,\xi} \\ \phi_{,\eta} \end{bmatrix} \tag{B.32}$$

where

$$\mathbf{\Gamma} = \mathbf{J}^{-1} = \frac{1}{\det \mathbf{J}} \begin{bmatrix} J_{22} & -J_{12} \\ -J_{21} & J_{11} \end{bmatrix} \tag{B.33}$$

The Jacobian J can be regarded as a scale factor that multiplies $\mathrm{d}\xi\mathrm{d}\eta$ to produce the physical area increment $\mathrm{d}x\mathrm{d}y$[3].

The element strain-displacement relation now can be written as

$$\varepsilon = \mathbf{B}\mathbf{d} \tag{B.34}$$

whereas as the same time (assuming linearity) for a planar 2D element

$$\varepsilon = \begin{bmatrix} \varepsilon_x \\ \varepsilon_y \\ \gamma_{xy} \end{bmatrix} = \begin{bmatrix} 1 & 0 & 0 & 0 \\ 0 & 0 & 0 & 1 \\ 0 & 1 & 1 & 0 \end{bmatrix} \begin{bmatrix} u_{,x} \\ u_{,y} \\ v_{,x} \\ v_{,y} \end{bmatrix} \tag{B.35}$$

where

$$\begin{bmatrix} u_{,x} \\ u_{,y} \\ v_{,x} \\ v_{,y} \end{bmatrix} = \begin{bmatrix} \Gamma_{11} & \Gamma_{12} & 0 & 0 \\ \Gamma_{21} & \Gamma_{22} & 0 & 0 \\ 0 & 0 & \Gamma_{11} & \Gamma_{12} \\ 0 & 0 & \Gamma_{21} & \Gamma_{22} \end{bmatrix} \begin{bmatrix} u_{,\xi} \\ u_{,\eta} \\ v_{,\xi} \\ v_{,\eta} \end{bmatrix} \tag{B.36}$$

where

$$\begin{bmatrix} u_{,\xi} \\ u_{,\eta} \\ v_{,\xi} \\ v_{,\eta} \end{bmatrix} = \begin{bmatrix} N_{1,\xi} & 0 & N_{2,\xi} & 0 & N_{3,\xi} & 0 & N_{4,\xi} & 0 \\ N_{1,\eta} & 0 & N_{2,\eta} & 0 & N_{3,\eta} & 0 & N_{4,\eta} & 0 \\ 0 & 1,\xi & 0 & N_{2,\xi} & 0 & N_{3,\xi} & 0 & N_{4,\xi} \\ 0 & N_{1,\eta} & 0 & N_{2,\eta} & 0 & N_{3,\eta} & 0 & N_{4,\eta} \end{bmatrix} \mathbf{d} \tag{B.37}$$

[3]For rectangles or parallelograms $J = \frac{A}{4}$, where A is the area of the physical element

where $N_{1,\xi} = -\frac{1-\eta}{4}$, and so on. Comparing above equations with Eq. (B.34) we can define the strain-displacement matrix as

$$\mathbf{B} = \begin{bmatrix} 1 & 0 & 0 & 0 \\ 0 & 0 & 0 & 1 \\ 0 & 1 & 1 & 0 \end{bmatrix} \begin{bmatrix} \Gamma_{11} & \Gamma_{12} & 0 & 0 \\ \Gamma_{21} & \Gamma_{22} & 0 & 0 \\ 0 & 0 & \Gamma_{11} & \Gamma_{12} \\ 0 & 0 & \Gamma_{21} & \Gamma_{22} \end{bmatrix} \begin{bmatrix} N_{1,\xi} & 0 & N_{2,\xi} & 0 & N_{3,\xi} & 0 & N_{4,\xi} & 0 \\ N_{1,\eta} & 0 & N_{2,\eta} & 0 & N_{3,\eta} & 0 & N_{4,\eta} & 0 \\ 0 & 1,\xi & 0 & N_{2,\xi} & 0 & N_{3,\xi} & 0 & N_{4,\xi} \\ 0 & N_{1,\eta} & 0 & N_{2,\eta} & 0 & N_{3,\eta} & 0 & N_{4,\eta} \end{bmatrix} \tag{B.38}$$

Now the stiffness matrix of an element of thickness t can be calculated as

$$\mathbf{K}^{\mathrm{e}} = \iint \mathbf{B}^T \mathbf{E} \mathbf{B} t \mathrm{d}x\mathrm{d}y = \int_{-1}^{1} \int_{-1}^{1} \mathbf{B}^T \mathbf{E} \mathbf{B} t J \mathrm{d}\xi \mathrm{d}\eta \tag{B.39}$$

Note: nodes may be numbered in arbitrary manner, though, when using the N_i as defined in Eq. (B.27) the cyclic order must be maintained and must run counterclockwise in order for J not to become negative.

In the case of a scalar field quantity, such as temperature $\mathbf{T}$ in heat conduction, at every node i there exists a single DOF ϕ_i. For a scalar field element Eq. (B.32) can be written as

$$\begin{bmatrix} \phi_{,x} \\ \phi_{,y} \end{bmatrix} = \begin{bmatrix} \Gamma_{11} & \Gamma_{12} \\ \Gamma_{21} & \Gamma_{22} \end{bmatrix} \begin{bmatrix} N_{1,\xi} & N_{2,\xi} & N_{3,\xi} & N_{4,\xi} \\ N_{1,\eta} & N_{2,\eta} & N_{3,\eta} & N_{4,\eta} \end{bmatrix} \begin{bmatrix} \phi_1 \\ \phi_2 \\ \phi_3 \\ \phi_4 \end{bmatrix} \tag{B.40}$$

and thus for a scalar field element

$$\mathbf{B} = \begin{bmatrix} \Gamma_{11} & \Gamma_{12} \\ \Gamma_{21} & \Gamma_{22} \end{bmatrix} \begin{bmatrix} N_{1,\xi} & N_{2,\xi} & N_{3,\xi} & N_{4,\xi} \\ N_{1,\eta} & N_{2,\eta} & N_{3,\eta} & N_{4,\eta} \end{bmatrix} \tag{B.41}$$

Equivalently to Eq. (B.39) the element characteris matrix, e.g. for heat conduction problems the conductivity matrix, for the four-node plane element is

$$\mathbf{K}^{\mathrm{e}} = \int \mathbf{B}^T \boldsymbol{\kappa} \mathbf{B} t \mathrm{d}A = \int_{-1}^{1} \int_{-1}^{1} \mathbf{B}^T \boldsymbol{\kappa} \mathbf{B} t J \mathrm{d}\xi \mathrm{d}\eta \tag{B.42}$$

Quadrature

Numerical integration of element properties operates by evaluating (or sampling) the function at specific points, multiplying the resulting number by an appropriate weighting factor and summing the results. Gauss quadrature is the most often used rule in generating element matrices. It locates sampling points and assigns weights so as to minimize integration errors when the integrand is a general polynomial.

In 2D, consider the function $\phi = \phi(\xi, \eta)$, integrating first with respect to ξ and then with respect to η one obtains

$$\begin{aligned} I &= \int_{-1}^{1}\int_{-1}^{1} \phi(\xi,\eta)\mathrm{d}\xi\,\mathrm{d}\eta \approx \int_{-1}^{1}\left[\sum_i W_i\phi(\xi_i,\eta)\right]\mathrm{d}\eta \\ &\approx \sum_j W_j\left[\sum_i W_i\phi(\xi_i,\eta_j)\right] = \sum_i\sum_j W_iW_j\phi(\xi_i,\eta_j) \end{aligned} \tag{B.43}$$

where I is the integrand. For a four-point integration rule, $W_iW_j = 1$ at each Gauss point and hence,

$$I \approx \phi_1 + \phi_2 + \phi_3 + \phi_4 \tag{B.44}$$

where ϕ_i is the numerical value of ϕ at the ith Gauss point. In general, if $\phi = J$, the Jacobian of the transformation, the integration provides the length, area or volume of the physical element.

C. LAGRANGE MULTIPLIERS

This section provides additional information about the derivation of Lagrange multipliers, as found in [26]. The necessary condition for the reduced gradient to vanish at a stationary point can be written as

$$\left(\frac{\partial f}{\partial \mathbf{d}}\right)_{\dagger} - \left(\frac{\partial f}{\partial \mathbf{s}}\right)_{\dagger} \left(\frac{\partial \mathbf{h}}{\partial \mathbf{s}}\right)_{\dagger}^{-1} \left(\frac{\partial \mathbf{h}}{\partial \mathbf{d}}\right)_{\dagger} = \mathbf{0}^T \tag{C.1}$$

where $\mathbf{s}$ denote the solution or state variables and $\mathbf{d}$ indicate the remaining decision variables. Now we may define

$$\boldsymbol{\lambda}^T \triangleq -\left(\frac{\partial f}{\partial \mathbf{s}}\right)_{\dagger} \left(\frac{\partial \mathbf{h}}{\partial \mathbf{s}}\right)_{\dagger}^{-1} \tag{C.2}$$

and with some rearrangement one obtains

$$\begin{aligned} \left(\frac{\partial f}{\partial \mathbf{d}}\right)_{\dagger} + \boldsymbol{\lambda}^T \left(\frac{\partial \mathbf{h}}{\partial \mathbf{d}}\right)_{\dagger} &= \mathbf{0}^T \\ \left(\frac{\partial f}{\partial \mathbf{s}}\right)_{\dagger} + \boldsymbol{\lambda}^T \left(\frac{\partial \mathbf{h}}{\partial \mathbf{s}}\right)_{\dagger} &= \mathbf{0}^T \end{aligned} \tag{C.3}$$

The stationary condition Eq. (C.3) can be rewritten in terms of the vector $\boldsymbol{\lambda}$ and the vector of variables $\mathbf{s} = (\mathbf{d}, \mathbf{s})^T$ as

$$\nabla f(\mathbf{s}_{\dagger}) + \boldsymbol{\lambda}^T \nabla \mathbf{h}(\mathbf{s}_{\dagger}) = \mathbf{0}^T \tag{C.4}$$

which shows that the necessary condition for a minimum is that the gradient of the objective must be a linear combination of the gradients of the constraints, at this minimizing point. The stationarity condition Eq. (C.4) is often expressed in terms of a special function, the Lagrangian function defined by

$$\mathscr{L}(\mathbf{s}, \boldsymbol{\lambda}) \triangleq f(\mathbf{s}) - \boldsymbol{\lambda}^T \mathbf{h}(\mathbf{s}) \tag{C.5}$$

where $\boldsymbol{\lambda}$ is a vector of new variables called Lagrange multipliers. The sign in front of $\boldsymbol{\lambda}$ is related to whether the positive or negative (null) form is used for the model.

A more general sufficiency condition for a constrained minimum states that a feasible point $\mathbf{s}_* = (\mathbf{d}_*, \mathbf{s}_*)^T$ satisfying the conditions $\left(\frac{\partial f}{\partial \mathbf{d}}\right)_* = \mathbf{0}^T$ and $\partial \mathbf{d}^T \left(\frac{\partial^2 f}{\partial \mathbf{d}^2}\right)_* \partial \mathbf{d} > 0$ is a local constrained minimum.

The sufficiency conditions can be restated such that if a feasible point $\mathbf{s}_*$ exists together with a vector $\boldsymbol{\lambda}$ such that $\nabla f(\mathbf{s}_*) + \boldsymbol{\lambda}^T \nabla \mathbf{h}(\mathbf{s}_*) = \mathbf{0}$ and the Hessian of the Lagrangian with respect to $\mathbf{s}$ is positive definite on the subspace tangent to $\mathbf{h}(\mathbf{s})$ at $\mathbf{s}_*$, then $\mathbf{s}_*$ is a local constrained minimum.

Equivalently similar conditions can be derived for inequality constraints.